

# Exploring the Stability of Planar-Architecture Perovskite Solar Cells

Tarek Ibrahim Alanazi

The University of Sheffield

Faculty of Science

Department of Physics and Astronomy



The  
University  
Of  
Sheffield.

Thesis submitted for the degree of Doctor of Philosophy in Physics

August 2021

# Acknowledgements

---

---

First, I would like to thank my God, *Allah* Almighty, who has guided me and gave me patience and strength throughout my PhD.

I would like to express my deep gratitude towards my supervisor, Prof. David Lidzey. I have been fortunate to pursue doctoral research with him in a supportive environment. He has always been willing and able to provide guidance, feedback, and advice, which has made this PhD come to fruition. Working with the EPMM group has been a great experience with the friendly setting, motivation, help, and scholarly contributions towards my PhD; I thank all my group members for it.

I would like to extend special thanks to our great and humble postdoc, Dr Onkar Game for his guidance, support, ideas, contribution, and compassion. His assistance in the lab has been absolutely helpful. I am also grateful to Joel Smith for his critical advice, which has been of great help. Also, a big thank you to Rachel Kilbride, Dr Claire Greenland, Dr Rahul Jayaprakash, Dr Kyriacos Georgiou for their contributions towards my doctoral work. I would like to acknowledge Nick Terrill from Diamond Light Source Ltd. for his support during *in situ* stability experiments.

I would like to thank my family, especially my parents, wife, children for their support and patience during this long journey.

I am greatly indebted to Northern Border University (NBU) for funding my PhD scholarship.

# Abstract

---

---

The aim of this thesis is to study the stability of lead halide perovskites when used in planar (*n-i-p*) photovoltaic (PV) devices. Since their first use in solar cells, a tremendous improvement has been witnessed in the efficiency of perovskite devices which now compete with established single crystalline silicon technologies. Notably, the low costs associated with the fabrication of perovskite devices from solution makes them a very promising challenger PV technology.

For perovskite solar cell manufacture to become commercially viable, device stability needs to be increased towards that of silicon that typically has an operational lifetime in excess of 25 years. This issue is addressed in Chapter 4, where the role of perovskite composition is explored using a device structure based on ITO/SnO<sub>2</sub>/perovskite/HTL/Au. Devices based on the perovskite MAPbI<sub>3</sub> are explored alongside those based on the triple-cation perovskite Cs<sub>0.05</sub>FA<sub>0.79</sub>MA<sub>0.15</sub>PbI<sub>2.45</sub>Br<sub>0.55</sub>. While both types of device have shown power conversion efficiencies (PCE), [16% and 19.5% respectively], it is found that triple-cation perovskites have substantially better structural and optoelectronic properties; a feature that is reflected by enhanced film and device stability. Using optimised triple-cation perovskites, the effect of the hole transport material (HTM) used in PV devices is then explored. Here, devices were fabricated using the HTMs Spiro-OMeTAD and PTAA, and it is found that PTAA devices demonstrate higher thermal and dark-storage stability compared to Spiro-OMeTAD. This result suggests that further investigation of HTMs and other charge-selective interlayers are crucial to create devices that combine both high efficiency and long-term operational stability.

In Chapter 5, the effect of incorporating potassium iodide (KI) into a triple-cation perovskite device is explored. Here, it is shown that this additive (that is often used a defect passivating agent), can in fact reduce film and device stability. This result is explained by a small amount of KOH contained within a SnO<sub>2</sub> colloidal solution used to prepare the electron transfer layer (ETL). It is proposed that the KOH negates the benefits resulting from the KI passivation, leading to the formation of an undesirable secondary KBr phase.

# Publications

---

---

As Chapter (5)

1. **Tarek I. Alanazi**, Onkar S. Game, Joel A. Smith, Rachel C. Kilbride, Claire Greenland, Rahul Jayaprakash, Kyriacos Georgiou, Nicholas J. Terrill, David G. Lidzey, *Potassium iodide reduces the stability of triple-cation perovskite solar cells*, RSC Advances, **2020**, 10, 66, 40341-50. DOI: 10.1039/D0RA07107B
2. I. M. Dharmadasa, Yaqub Rahaq, Ayotunde A. Ojo, **Tarek I. Alanazi**, *Perovskite solar cells: a deep analysis using current–voltage and capacitance–voltage techniques*, Journal of Materials Science: Materials in Electronics, **2019**, 30, 2, 1227-35. DOI: 10.1007/s10854-018-0390-5
3. Benjamin G. Freestone, Joel A. Smith, Giacomo Piana, Rachel C. Kilbride, Andrew J. Parnell, Luca Sortino, David M. Coles, Orianna B. Ball, Natalia Martsinovich, Courtney J. Thompson, **Tarek I. Alanazi**, Onkar S. Game, Alexander I. Tartakovskii, Pavlos Lagoudakis, David G. Lidzey, Low-dimensional emissive states in non-stoichiometric methylammonium lead halide perovskites, Journal of Materials Chemistry A, **2019**, 7, 18, 11104-16. DOI: 10.1039/C8TA12184B
4. Joel A. Smith, Onkar S. Game, James E. Bishop, Emma L. Spooner, Rachel C. Kilbride, Claire Greenland, Rahul Jayaprakash, **Tarek I. Alanazi**, Elena J. Cassella, Alvaro Tejada, Ganna Chistiakova, Michael Wong-Stringer, Thomas J. Routledge, Andrew J. Parnell, Deborah B. Hammond, David G. Lidzey, *Rapid scalable processing of tin oxide transport layers for perovskite solar cells*, ACS Applied Energy Materials, **2020**, 3, 6, 5552-62. DOI: 10.1021/acsaem.0c00525

5. Onkar S. Game, Joel A. Smith, **Tarek I. Alanazi**, Michael Wong-Stringer, Vikas Kumar, Cornelia Rodenburg, Nick J. Terrill, David G. Lidzey, *Solvent vapour annealing of methylammonium lead halide perovskite: what's the catch?*, *Journal of Materials Chemistry A*, **2020**, 8, 21, 10943-56. DOI: 10.1039/D0TA03023F
  
6. Gabriel E. Pérez, Harikrishna Erothu, Paul D. Topham, Francesco Bastianini, **Tarek I. Alanazi**, Gabriel Bernardo, Andrew J. Parnell, Stephen M. King, Alan D. Dunbar, *Improved Performance and Stability of Organic Solar Cells by the Incorporation of a Block Copolymer Interfacial Layer*, *Advanced Materials Interfaces*, **2020**, 7, 18, 2000918. DOI: 10.1002/admi.202000918
  
7. Mary E. O'Kane, Joel A. Smith, **Tarek I. Alanazi**, Elena J. Cassella, Onkar S. Game, Sandra van Meurs, David G. Lidzey, *Perovskites on Ice: An Additive-Free Approach to Increase the Shelf-Life of Triple-Cation Perovskite Precursor Solutions*, *ChemSusChem*, **2021**. DOI:10.1002/cssc.202100332

# Conference Presentations

---

---

Oral presentation

**Tarek I. Alanazi**, Onkar S. Game, Joel A. Smith, Rachel C. Kilbride, David G. Lidzey, *Influence of Potassium Iodide Inclusion on Operational Lifetime of Triple-Cation Mixed-Halide Perovskite Solar Cells*, UK Semiconductors 2019, **July 2019**.

# Table of Contents

---

---

<b>Chapter 1: Introduction</b>	<b>1</b>
1.1: Thesis Motivation .....	6
1.2: Thesis Aims .....	6
1.3: Thesis Overview .....	6
1.4: References .....	9
<b>Chapter 2: Background Theory</b>	<b>10</b>
2.0: An Introduction to Photovoltaics .....	10
2.1: Characterising Solar Cells .....	12
2.2: Structure of Perovskites .....	17
2.3: Properties of Perovskite Materials .....	19
2.4: Device Structure of Perovskite Solar Cells .....	20
2.5: Working Mechanism of Perovskite Solar Cells .....	21
2.6: Charge Transport Materials .....	22
2.7: A Brief Review of the Development Process of Perovskite Solar Cells	23
2.8: Stability of Perovskite Solar Cells.....	28
2.9: Strategies to Improve the Stability of Perovskite Solar Cells .....	37
2.10: Summary .....	42
2.11: References .....	43
<b>Chapter 3: Experimental Methods</b>	<b>62</b>
3.0: Introduction .....	62
3.1: Deposition Techniques .....	62
3.2: Materials .....	65
3.3: Device Fabrication .....	67
3.4: Device Characterisation .....	71
3.5: Microscopy and Spectroscopy .....	73
3.6: References .....	82

<b>Chapter 4: Investigating the stability of perovskite photovoltaic devices: Role of perovskite compositions and hole transport layers</b>	<b>84</b>
4.0: Introduction .....	84
4.1: Results and Discussion .....	88
4.2: Conclusion .....	108
4.3: References .....	110
<b>Chapter 5: Potassium Iodide Reduces the Stability of Triple-Cation Perovskite Solar Cells</b>	<b>115</b>
5.0: Motivation of Work .....	116
5.1: Publication Main Body.....	117
5.2: Supporting Information .....	153
5.3: References.....	162
<b>Chapter 6: Conclusions and Proposed Future Work</b>	<b>167</b>

# Chapter 1

---

## Introduction

It is well established that our dependence on non-renewable resources, especially fossil fuels to provide our energy has led to adverse, catastrophic effects on the planet, visible locally through soil and water pollution, and globally through the increase in greenhouse gas (GHG) emissions.<sup>[1]</sup> The threat of global climate change is already underway, with demands being made for immediate actionable ideas to reduce carbon dioxide (CO<sub>2</sub>) and other GHG emissions and to seek alternative sources in meeting our ever-increasing energy demands. To this end, societies are increasingly turning to sustainable resources to generate energy, including wind power, hydroelectric power, geothermal power, and perhaps, the mightiest of all, solar power. Unlike nuclear power, most of these resources are widely available, practically free, and environmentally-friendly. In addition to being a potential solution to climate change, renewable energy resources are highly desirable, with governments setting economic policies to favour their use. For example, Saudi Arabia is planning to maximise solar-powered energy through the massive installation of photovoltaics (PV). While the currently installed PV is expected to provide 20 GW in Saudi Arabia by 2023, it has also been anticipated that further expansion will increase this to about 40 GW by 2030, as proposed in the Saudi Vision 2030.<sup>[2]</sup> In the global context, nearly a third of new electricity generation is projected to be from the use of PVs by 2030<sup>[3]</sup>, largely owing their cost effectiveness; here there has been extensive reductions in the cost of manufacturing PVs with their

average price dropping from \$100/W to less than \$0.5/W over the past few decades.<sup>[4]</sup>

It has taken humankind more than a century to utilise PVs for energy generation since their discovery by Becquerel in 1839.<sup>[5]</sup> Progress in PV research and development has witnessed unparalleled growth following the invention of the first generation of solar cells based on silicon in 1954, with this type of device becoming the current industry leader.<sup>[6]</sup> Other materials such as cadmium telluride (CdTe) (in the form of thin film semiconductors) have also been used to produce solar cells that are efficient, stable under operational conditions and cheap to produce. One important parameter that measures the light incident converted to electricity is the power conversion efficiency (PCE). This is calculated under a standard light intensity and spectrum and can be used to compare the efficiencies of different PV devices. Based on PCE measurements tracked by National Renewable Energy Laboratory (NREL) over the decades, the immense technological progress towards achieving higher efficiency PVs can be clearly evidenced (see Figure 1).<sup>[7]</sup>

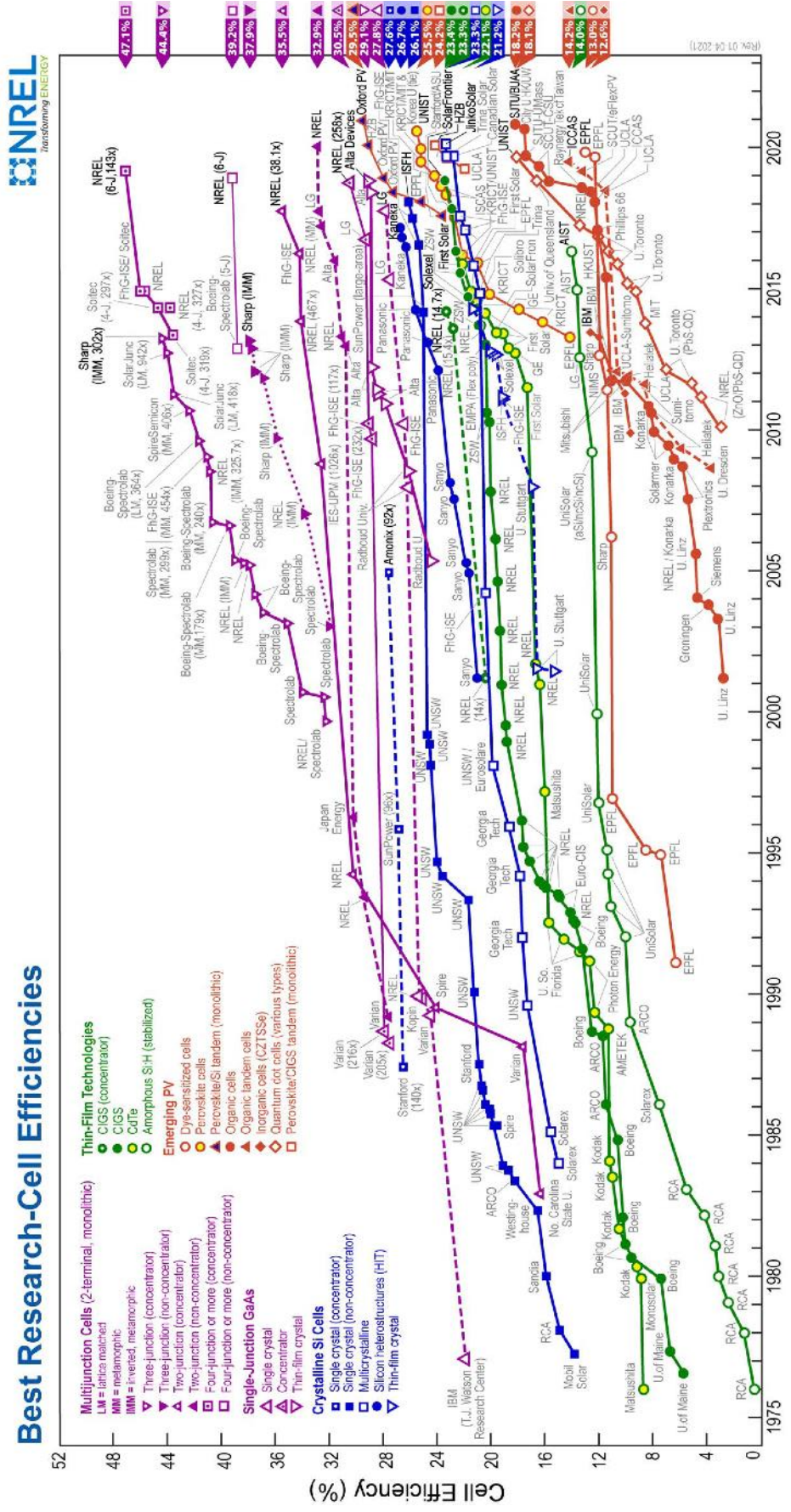


Figure 1: Certified highest efficiencies for a variety of PV technologies provided by NREL.[7]

Overall, the three main generations of PV technology have emerged. The first generation was based on silicon such as crystalline (c-Si) and amorphous silicon (a-Si). In the late 20<sup>th</sup> century, silicon-based solar cells reached an efficiency of 27.6%. Here, early generations of devices required active layer thickness of hundreds of microns to absorb sufficient light to enhance their PCE. Furthermore, silicon wafers are produced using large inputs of energy in order to reach a purity necessary for high performance.<sup>[8]</sup> These processes made such devices relatively expensive to produce, although such drawbacks, have stimulated research into a second generation PV technology. Such 2<sup>nd</sup> generation devices are based on thin films of semiconductors having higher absorption coefficients that are produced using low temperature processes, with one of the key examples being CdTe-based solar cells.<sup>[9]</sup> Here, thin film solar cells are relatively easy to fabricate which has led to an overall reduction in their cost of production. However, despite years of research, thin film technologies have failed to displace PV-based on silicon, with such devices only reaching < 10% of market share to date.<sup>[10]</sup>

Over the past 30 years, much research has explored the use of organic semiconductors (polymers and small molecules) for PV applications. These materials can potentially be easily manufactured and in some cases have reasonably efficient PV performance. These are considered so-called 3<sup>rd</sup> generation PV technologies, which include dye sensitized solar cells (DSSCs) and organic solar cells (OSCs). These materials however, also face a number of challenges including their low PCEs compared to silicon-based solar cells, and their substantial degradation under operational conditions associated with intrinsic and extrinsic instabilities.<sup>[11]</sup> Despite lower PCEs, these materials are potentially economic in terms of fabrication

when compared to the first generation PV, thus making them cost-competitive for industry purposes.<sup>[12]</sup>

Towards the start of the 21<sup>st</sup> century, a remarkable new PV technology emerged in the form of perovskite solar cells (PSCs); in 2009, Kojima *et al.* first introduced a perovskite material instead of a light-absorbing dye molecule in a DSSC.<sup>[13]</sup>

Perovskites are a class of materials with a crystal structure of ABX<sub>3</sub> where an 'A' is an organic cation, a 'B' is a metal cation, and an 'X' is an anion.<sup>[14,15]</sup> Since then, considerable progress has been made in the field of PSCs which have enjoyed an unprecedented rise in PCE, reaching 25.5% and exceeding all the other third generation PV technologies.<sup>[7]</sup> These devices potentially combine low fabrication cost, enhanced optoelectronic properties and ease of cell manufacture, making them a serious bet for commercially viable manufacture. However, for perovskites to be viable, it is important to address the issue of their long-term stability. This is one of the main concerns regarding the application of perovskites as they can degrade quickly when exposed to ambient conditions.<sup>[3,16]</sup> If perovskites manage to overcome this obstacle, there exists a real potential for them transferring out of the lab and into the market.

## **1.1: Thesis Motivation**

Perovskite solar cells (PSCs) have undergone a massive improvement in their efficiency, however, two key drawbacks of perovskites remain in the form of toxicity (lead) and stability. The first limitation can be avoided by using high quality encapsulation or by replacing lead with other materials such as tin. However, device stability continues to remain a hurdle for PSC commercialisation, and is the main topic of this thesis.

## **1.2: Thesis Aims**

The main aim of this doctoral research is to develop highly efficient as well as stable PV devices. The work described includes a study into two perovskite compositions and different charge transporting materials, together with the use of defect passivation, with the overall aim being the development of strategies to enhance device efficiency and extend operational lifetime.

## **1.3: Thesis Overview**

**Chapter 2** presents a background summary of PVs and their operation. A brief history of PV technology is provided. The chemical structure, properties, and device structure of PSCs are summarised. The development of PSCs is briefly reviewed. The chapter also includes information on perovskite stability and strategies to avoid degradation process as an introduction to the experiments discussed in Chapters 4 and 5 respectively.

**Chapter 3** summarises deposition techniques to create a PSC device as well as types of materials used in devices including perovskite active materials and charge

transport layers. The fabrication and characterisation techniques that are used in Chapters 4 and 5 are also outlined.

**Chapter 4** discusses the stability of two popular perovskite compositions namely methylammonium lead iodide ( $\text{MAPbI}_3$ ) and cesium formamidinium methylammonium lead iodide bromide with a formula of ( $\text{Cs}_{0.05}\text{FA}_{0.79}\text{MA}_{0.15}\text{PbI}_{2.45}\text{Br}_{0.55}$ ) known as a triple-cation mixed-halide. The chapter discusses the nuances of compositional engineering. It is shown that triple-cation perovskite film is highly stable under high stress conditions. High operational and shelf stability are also observed in devices using spiro-OMeTAD as a hole transport layer (HTL). The same perovskite composition is utilised with PTAA as a HTL and is shown to demonstrate high thermal stability. Building upon existing perovskite literature, we conclude that a triple-cation perovskite containing Cs, FA, and MA is a promising material composition against rapid device degradation.

**Chapter 5** explores PSCs utilising  $\text{SnO}_2$  and  $\text{TiO}_2$  as an electron transport layers (ETLs) and the role of passivating potassium iodide (KI) on efficiency and stability. It is observed that the efficiency of  $\text{SnO}_2$  ETL devices decreases with an increase in the amount of KI used, which also reduces the long-term operational stability of the cells. It is found that as the amount of KI increases by more than 5%, a secondary phase appears in the form of potassium bromide (KBr) that becomes a favourable product causing instability. Another reason for this instability arises as the potassium hydroxide (KOH) stabiliser that is present in the colloidal dispersion, already passivates the  $\text{SnO}_2$ /perovskite interface. However,  $\text{TiO}_2$  ETL devices show substantial improvement in the efficiency yet no enhancement in stability.

**Chapter 6** summarises the results of this thesis alongside proposals for future work to enhance device stability and drive PSCs towards commercialisation.

## 1.4: References

- [1] P. Erickson, H. van Asselt, D. Koplow, M. Lazarus, P. Newell, N. Oreskes, G. Supran, *Nature* **2020**, 578, E1.
- [2] Z. S. AlOtaibi, H. I. Khonkar, A. O. AlAmoudi, S. H. Alqahtani, *Energy Transitions* **2020**, 4, 1.
- [3] M. A. Green, A. Ho-Baillie, H. J. Snaith, *Nat. Photonics* **2014**, 8, 506.
- [4] W. F. Pickard, *Energy Policy* **2017**, 107, 488.
- [5] N. Gasparini, A. Salleo, I. McCulloch, D. Baran, *Nat. Rev. Mater.* **2019**, 4, 229.
- [6] M. A. Green, *Prog. Photovoltaics Res. Appl.* **2005**, 13, 447.
- [7] NREL, "Best Research-Cell Efficiency Chart," **2021**.
- [8] J. Nelson, *The Physics of Solar Cells*, Published by Imperial College Press and Distributed by World Scientific Publishing Co., **2003**.
- [9] A. Polman, M. Knight, E. C. Garnett, B. Ehrler, W. C. Sinke, *Science*. **2016**, 352, aad4424.
- [10] T. D. Lee, A. U. Ebong, *Renew. Sustain. Energy Rev.* **2017**, 70, 1286.
- [11] Z. L. Wang, W. Wu, *Angew. Chemie Int. Ed.* **2012**, 51, 11700.
- [12] G. Li, X. Gao, *Adv. Mater.* **2020**, 32, 1806478.
- [13] A. Kojima, K. Teshima, Y. Shirai, T. Miyasaka, *J. Am. Chem. Soc.* **2009**, 131, 6050.
- [14] Y. K. Wang, Z. Q. Jiang, L. S. Liao, *Chinese Chem. Lett.* **2016**, 27, 1293.
- [15] G. Zheng, C. Zhu, J. Ma, X. Zhang, G. Tang, R. Li, Y. Chen, L. Li, J. Hu, J. Hong, Q. Chen, X. Gao, H. Zhou, *Nat. Commun.* **2018**, 9, 2793.
- [16] H. J. Snaith, *J. Phys. Chem. Lett.* **2013**, 4, 3623.

# Chapter 2

---

## Background Theory

### 2.0: An Introduction to Photovoltaics

There has been significant increase in the demand for energy over time following global economic growth.<sup>[1]</sup> Much of the world's supply of energy is currently supplied from fossil fuels.<sup>[2]</sup> However to store and generate clean and renewable energy, more modern technologies are being developed ranging from lithium-ion batteries,<sup>[3-7]</sup> fuel cells,<sup>[8-11]</sup> water splitting,<sup>[12-15]</sup> supercapacitors<sup>[16-19]</sup> and solar energy.<sup>[20-29]</sup> Recently, the use of solar photovoltaics to generate electricity has grown significantly as they represent a clean and abundant sustainable energy technology.

Solar cells are devices composed of semiconductor materials possessing the ability to absorb sunlight and generate an electron-hole pair. This is then separated into free charge carriers via an in-built asymmetry in the device which produces a photocurrent that can be used to generate power when connected to an external circuit. The technique of electrical energy generation from light is not as modern as we think; Becquerel first discovered that a photovoltaic (PV) was produced when an electrode was placed in an electrolyte solution under sunlight in 1839.<sup>[30,31]</sup> After that, Adams and Day recognised a similar effect within a material called selenium, with Smith establishing photoconductive behaviour in selenium in 1873.<sup>[32]</sup> However it took an additional thirty years to generate a power conversion efficiency (PCE) of approximately 1% in a selenium solar cell. <sup>[33]</sup> Rapid development in PV

cells was then made, with a PCE of 6% demonstrated in 1954 in a silicon single crystal solar cell.<sup>[34]</sup>

Significant research and development has been performed in the past couple of decades to improve the basic materials used in solar cells. This has resulted in the development of three main generations of solar cells. The first generation was based on single crystalline silicon, polycrystalline silicon and amorphous silicon. Here, crystalline silicon solar cells can reach PCEs of up to 27.6%.<sup>[35]</sup> However such PV devices require silicon to be purified to extremely high levels which increases manufacturing costs. There is also a significant environmental impact in their production due to the release of by-products. In order to overcome this problem, significant research has been done into the identification of alternate materials that can be used to produce high performance devices with minimal environmental impact.

Second generation solar cells are based on inorganic materials such as cadmium sulfide (CdS), cadmium selenide (CdSe), cadmium telluride (CdTe), gallium arsenide (GaAs), copper indium selenide (CIS) and copper indium gallium selenide (CIGS) films. The PCE of these cells is roughly equivalent to those of Si-based PV devices and is between 22.1 to 23.4%.<sup>[35]</sup> However the toxicity of these relatively-rare materials has halted their further development.<sup>[36]</sup> Another challenge for second-generation solar cells is material degradation; for example the front contact electrode of CIS and CIGS film solar cells undergo corrosion when exposed to moisture.<sup>[37]</sup>

Third generation organic solar cells (OSCs) are generally much simpler to fabricate, a property that may potentially reduce their manufacturing costs. Another class of

3<sup>rd</sup> generation PV device are dye-sensitized solar cells (DSSCs) made using organic dyes together with a titanium dioxide (TiO<sub>2</sub>) electron absorber layer, and an I/I<sub>3</sub> based liquid electrolyte. The PCE of DSSCs has demonstrated a maximum PCE of 13%,<sup>[35]</sup> however the leakage of liquid electrolytes from such cells is a problem that has yet to be solved. Notably OSCs (usually composed of a blend of organic donor and acceptor molecules) can be produced utilising simple solution-based processed techniques. Here, the low cost of these processes coupled with their ease of fabrication has made third generation PV devices a popular research topic. Indeed, following intensive research, the performance of OSCs has risen to 18.2%.<sup>[35]</sup>

Recently, a new class of third generation PV device based on organic-inorganic halide perovskite <sup>[38-40]</sup> has risen to prominence. As we describe below, the unique properties of perovskites lead to the realisation of solar cells with high PCE that can be fabricated cheaply and simply. Such devices have the potential to replace the current Si-based solar cells and become the future market standard.<sup>[41]</sup>

## 2.1: Characterising Solar Cells

The electrical behaviour of a solar cell can be characterised by measuring the acquisition of a current-voltage ( $I$ - $V$ ) curve. Here, the voltage is applied between the contacts of a PV devices and a photocurrent is measured when the device is illuminated. The current produced depends on the active area of the PV, and thus the current density is calculated by dividing the photocurrent by the device active area. This measurement is critical to determine device performance metrics. A typical current density-voltage ( $J$ - $V$ ) curve for a solar cell is shown in Figure 1, where the direction of the photocurrent is taken as positive. The  $J$ - $V$  curve can also be used to determine the value of key performance metrics such as open-circuit voltage

( $V_{oc}$ ), short-circuit current density ( $J_{sc}$ ), fill factor (FF), PCE, shunt resistance ( $R_{SH}$ ) and series resistance ( $R_s$ ).<sup>[42]</sup>

When measured in the dark, a solar cell should work as a diode. In an ideal p-n junction solar cell, the Shockley equation describes the dependency of the current density to the voltage as expressed by equation 1.

$$J(V) = J_0 \left( e^{\frac{eV}{k_B T}} - 1 \right) \quad (Eq.1)$$

Here,  $e$  is the elementary charge,  $V$  is the applied voltage,  $k_B$  is the Boltzmann constant,  $T$  is the temperature and  $J_0$  is the reverse saturation current density. Under illumination, a photocurrent is produced. The photocurrent is treated as a positive quantity and denoted using  $J_{sc}$  (expressed as a current density), that flows in the opposite direction to the charge carriers that are injected by a positive applied voltage. Consequently, in an ideal p-n junction, the current density under illumination is expressed using in equation 2.

$$J(V) = J_0 \left( e^{\frac{eV}{k_B T}} - 1 \right) - J_{sc} \quad (Eq.2)$$

Several different parameters can be evaluated from a  $J$ - $V$  curve under illumination. For example, no current can be injected by an external voltage source at zero voltage. At this point, all current is generated by the conversion of solar energy and is labelled as  $J_{sc}$ . At a fixed positive voltage, the photocurrent is opposed by the injection current and thus the net current flow is zero. The voltage at this certain point is called  $V_{oc}$ .  $V_{oc}$  is generally generated as a result of the splitting of electron and hole quasi-Fermi energy levels under illumination of light.

$$V_{OC} = \left(\frac{1}{e}\right)(E_{Fn}E_{Fp}) \quad (Eq.3)$$

Here,  $E_{Fn}$  and  $E_{Fp}$  being the electron and hole quasi-Fermi levels respectively.<sup>[43]</sup> In practice, the  $V_{OC}$  of a device is dependent on the work function metal contacts and the band-gap structure of the active semiconductor, but it is reduced from its ideal values by charge-carrier recombination effects.

One of the most critical parameters that defines the performance of a PV device is its PCE. This is the product of voltage and current density, and is dependent upon the applied voltage. Figure 1 demonstrates the power output (cyan curve) for voltages ranging between 0 V and  $V_{OC}$ . At some specific voltage, a maximum power output occurs, with this particular point of operation referred to as the maximum power point (MPP). The power delivered at the MPP is the area defined by the rectangle enclosed by dashed lines. The maximum PCE of a single-junction PV has a theoretical limit (called the Shockley-Queisser (S-Q) limit<sup>[44]</sup>) that is approximately equal to 34% and is only reached using a semiconductor having a band gap of around 1.34 eV.

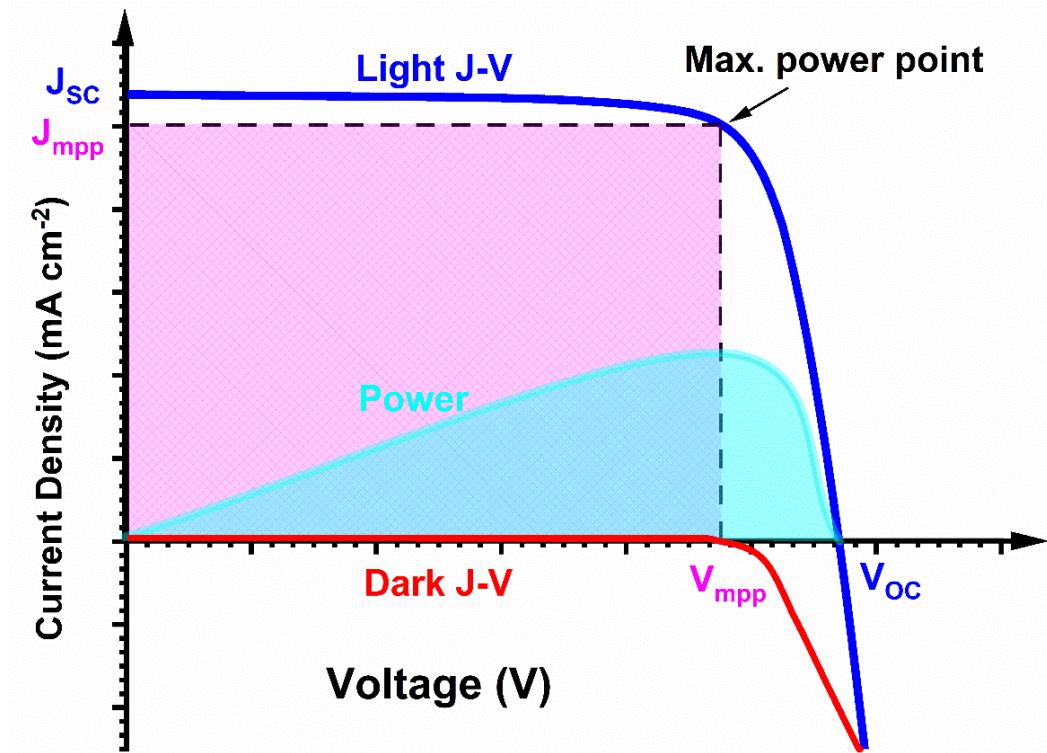


**Figure 1:** Typical J-V curve and corresponding power curve with indicated MPP parameters.

The current-density and voltage ( $J_{mpp}$  and  $V_{mpp}$ ) at the MPP respectively, are used to define the Fill-Factor (FF) as expressed by equation 4.

$$FF = \frac{J_{mpp}V_{mpp}}{J_{sc}V_{oc}} = \frac{P_{mpp}}{J_{sc}V_{oc}} \quad (Eq.4)$$

Here, the FF defines how rectangular the J-V curve is. It has been shown that ideal performance of PV device is reached when the FF approaches 80%. The FF is often contingent on the optimisation (or otherwise) of device fabrication.

To measure the PCE, the output power ( $P_{out}$ ) should be divided by the incident sunlight power ( $P_{in}$ ) as shown in equation 5.

$$PCE = \frac{P_{out}}{P_{in}} = \frac{P_{mpp}}{P_{in}} \quad (Eq.5)$$

By using equation 4 and substituting in equation 5, device efficiency can express using equation 6.

$$PCE = \frac{J_{sc}V_{oc}FF}{P_{in}} \quad (Eq.6)$$

It is clear therefore that FF is an important parameter that influences PCE. Device FF is also dominated by two other important parameters;  $R_{SH}$  and  $R_s$ . The  $R_{SH}$  of a solar cell is the resistance to leakage current that passes through the photoactive layer or any charge transporting layer used in a solar cell. Here, pinholes or roughness that form in the various layers during device fabrication can result in current leakage paths. This leakage current will then cause a loss in  $R_{SH}$  as shown in Figure 2 (a). However, the  $R_s$  of a solar cell encompasses all processes that resist the extraction of charge from the device. Here, the  $R_s$  will increase due to processes that limit the transport of charges from the solar cell. The main factors that contribute to high  $R_s$  include the bulk resistance of the semiconductor material and resistance of device interfaces and external contacts. When device fabrication quality is poor, a contact resistance can develop between the metallic device contacts and the semiconductor which also increases the  $R_s$ . Figure 2 (b) shows the effect of increased  $R_s$  on a solar cell's  $J-V$  characteristics.

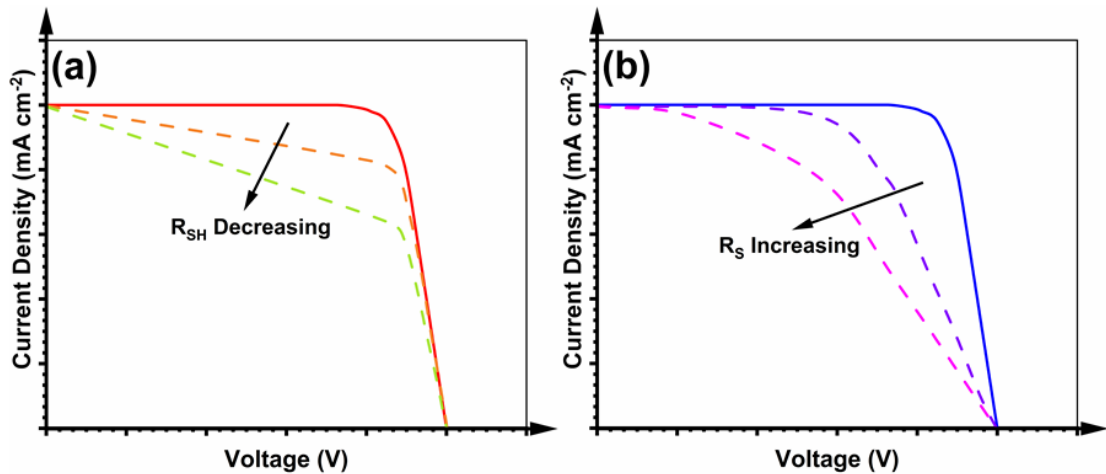


**Figure 2:** *J-V curves with dotted curves demonstrate (a) decreasing  $R_{SH}$  and (b) increasing  $R_S$ .*

## 2.2: Structure of Perovskites

The principal semiconductors explored in this thesis for PV applications are metal-halide perovskites. The first perovskites were discovered in mineral form and consisted of calcium titanium oxide ( $\text{CaTiO}_3$ ). This class of mineral was first discovered by Gustav Rose. Names after Lev Perovski, a Russian born mineralogist.<sup>[45]</sup> A perovskite is a compound belonging to the class of  $\text{ABX}_3$  compounds, where A and B are cations and X is an anion or halide. It has been shown that the A-site cation is located inside octahedral cages, with the structure of a perovskite consisting of a cubic array of corner-sharing  $[\text{BX}_6]$  octahedra as depicted in Figure 3. The structure of a perovskite can also be defined as a cubic close-packed  $[\text{AX}_3]$  array, where the B-site cations are located inside the octahedral holes. The metal-halide perovskites typical of those used in this thesis were first discovered by Dieter Weber 1978 <sup>[46]</sup> and comprise A-site organic and B-site inorganic components together with various X-site halides (e.g. bromide (Br), chloride (Cl) and iodide (I)).

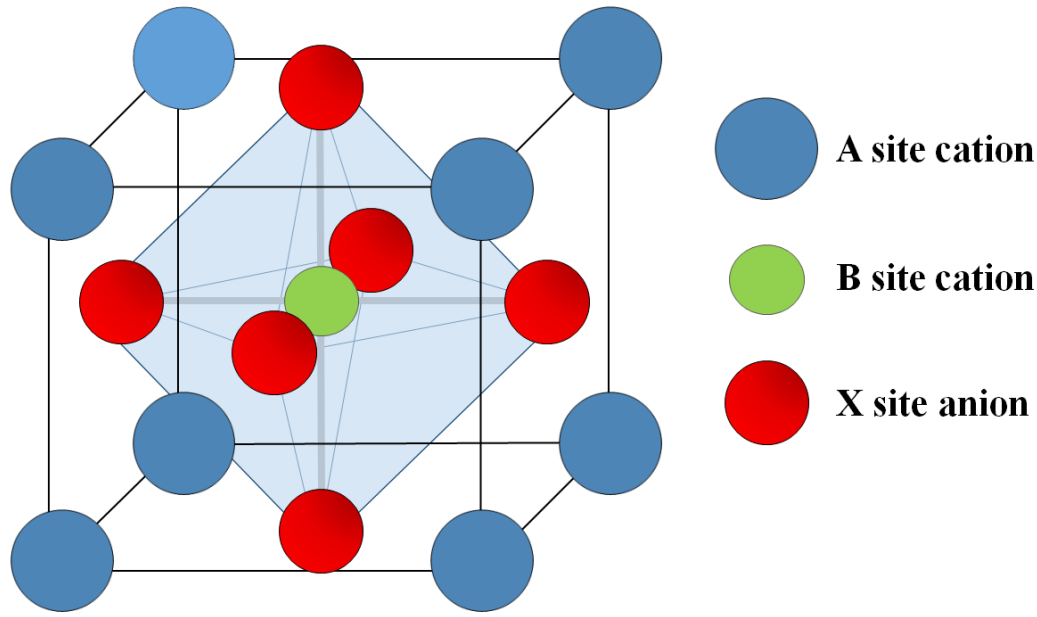


**Figure 3:** Crystal structure of a perovskite.

A variety of monovalent A-site cations have been variously explored including methylammonium (MA), formamidinium (FA)) or in certain cases an inorganic cation (e.g., cesium (Cs), rubidium (Rb), potassium (K), sodium (Na) etc). In such perovskite materials, the B-site is usually occupied by a divalent cation such as lead (Pb), tin (Sn) or germanium (Ge).

To understand whether a certain halide perovskite can be created, researchers often use the tolerance factor–octahedral factor map method.<sup>[47]</sup> Here, the empirical Goldschmidt tolerance factor ( $t$ ) is the principle factor responsible for the maintenance of the stability of a three dimensional (3D) perovskite structure, with  $t$  defined by equation 7.<sup>[48]</sup>

$$t = \frac{R_A + R_X}{\sqrt{2}(R_B + R_X)} \quad (\text{Eq.7})$$

Here,  $R_A$  defines the radius of a monovalent cation,  $R_B$  the radius of the divalent metal cation and  $R_X$  the radius of the monovalent halide anion. Here, an ideal 3D cubic crystal perovskite is expected to form when  $t = 1$ , with a cubic structure only

expected where  $0.89 < t < 1$ .<sup>[49]</sup> A reduced tolerance factor is indicative of lower symmetry, which often results in the transition of a cubic perovskite to an orthorhombic or tetragonal structure; a process which can potentially have a detrimental effect on optoelectronic properties.<sup>[49]</sup> In general, a perovskite material should have  $0.8 < t < 1$  to be termed as being stable.<sup>[50,51]</sup> Apart from the ionic radius of the constituent anions and cations, the phase of a perovskite can be affected by both temperature and pressure. For example, three main crystalline phases of the methylammonium lead iodide (MAPbI<sub>3</sub>) perovskite can exist, namely orthorhombic, tetragonal, and cubic, with these being dependent on temperature-dependent.<sup>[52]</sup>

### **2.3: Properties of Perovskite Materials**

Due to their structural versatility and vast compositional space, perovskites have an extensive range of functional properties, including electrical and optical. The perovskite MAPbI<sub>3</sub> which is often used in solar cell devices has an optical bandgap ( $E_g$ ) of 1.6 eV; a value that can be adjusted from 1.2 to 3.0 eV by engineering its chemical composition.<sup>[53]</sup> MAPbI<sub>3</sub> has a direct band gap with strong optical absorption (high absorption coefficient ( $\alpha$ )), coupled with a rapid onset of low Urbach energy ( $E_u$ ) and efficient photoluminescence emission. This material has other useful electronic characteristics, such as the direct production of free charge carriers at room temperature (electrons and holes) on photoexcitation as a result of a low exciton binding energy. Such perovskites also have high defect tolerance (resulting from shallow defect levels) and strong ambipolar charge carrier transport properties such as high mobility ( $\mu$ ), long lifetime ( $\tau$ ) and long diffusion lengths ( $L_d$ ).<sup>[47,54-58]</sup> As can be expected, the optoelectronic properties of such perovskites (which includes light absorption, charge generation and charge-extraction

capability) depend upon thin-film microstructure, formation, processing and material composition. This broad parameter space has prompted many researchers to analyse the dependence on device PCE and the perovskite crystal structure.<sup>[58-61]</sup>

## 2.4: Device Structure of Perovskite Solar Cells

Figure 4 shows a range of typical structures of a perovskite solar cell (PSC); these include so-called mesoporous (n-i-p) structure, regular planar (n-i-p) structure and inverted planar (p-i-n) structure (see Figure 4(a), (b) and (c) respectively). Here, regular planar n-i-p devices are generally formed using a transparent conductive oxide (TCO)/electron transport layer (ETL)/perovskite absorber layer/hole transport layer (HTL)/top electrode, while the order of these layers is reversed in a planar p-i-n device. Typical mesoporous n-i-p devices comprise of a thin film of compact TiO<sub>2</sub> (c-TiO<sub>2</sub>) capped by a mesoporous layer of (mp)-TiO<sub>2</sub> or aluminium oxide (mp-Al<sub>2</sub>O<sub>3</sub>) layer that functions as an ETL. A photoactive perovskite layer forms the heart of a PSC device. This usually consists of a material such as methylammonium lead halide (MAPbX<sub>3</sub>), formamidinium lead halide (FAPbX<sub>3</sub>) or cesium lead halide (CsPbX<sub>3</sub>). However as described in later sections, it is increasingly common to use perovskite materials that include two or three different cations.<sup>[62-67]</sup>, with the X-site anion being generally composed of I, Cl or Br or a combination of all three elements.<sup>[68]</sup>

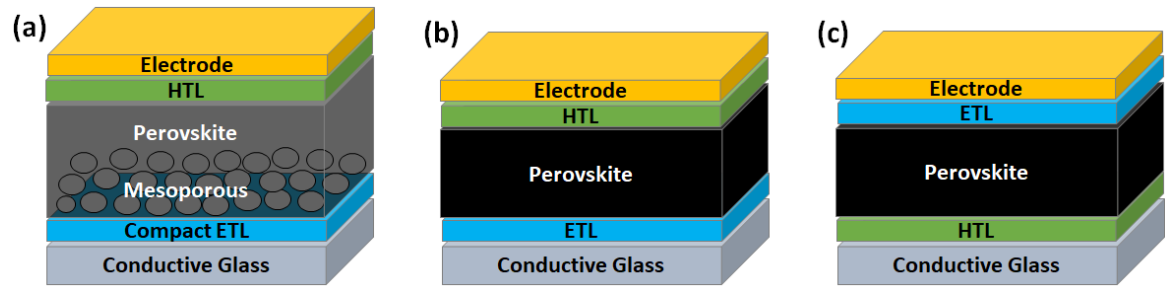


**Figure 4:** Schematic showing general device structures of PSCs (a) mesoporous n-i-p, (b) regular planar n-i-p, and (c) inverted planar p-i-n.

## 2.5: Working Mechanism of Perovskite Solar Cells

There is a general consensus amongst researchers regarding the operational principles of a PSC. Firstly, following exposure to light, excitons (electron-hole pairs) are photo-generated within the perovskite. The exciton binding energy for perovskite material is in the range of 2-50 meV<sup>[69]</sup> resulting in the dissociation of excitons into free energy carriers of electrons and holes at a room temperature.<sup>[70]</sup> These charge carriers then diffuse throughout the perovskite and become separated via electron- and hole-selective contacts. Here, a rapid transition of charge carriers occurs between the perovskite later to electron and hole transport layers, with typical transfer time being in the range of  $0.37 \pm 0.02$  ns and  $0.64 \pm 0.03$  ns between the perovskite MAPbI<sub>3</sub> and the ETL PCBM and the HTL spiro-OMeTAD respectively.<sup>[71]</sup> Once electrons/holes reach the anode/cathode, electrical power can be delivered to an external load upon connection to the circuit.<sup>[72]</sup> PSC performance is however affected by material composition and diffusion length of each type of charge carrier. Studies show that in the perovskite MAPbI<sub>3</sub>, electrons have a lower diffusion length than holes. This limits the active layer to a thickness of approximately few hundreds of nm.<sup>[73]</sup> However, a noticeable improvement in the electron diffusion lengths has been observed when using composite halide-based perovskites such as methylammonium lead iodide chloride (MAPbI<sub>3-x</sub>Cl<sub>x</sub>).<sup>[74]</sup>

## 2.6: Charge Transport Materials

### 2.6.1: Transparent Conductive Oxides

To act as both a window layer and a charge extraction contact, PSC devices are generally constructed on a transparent conductive oxide (TCO) film. These materials combine high conductivity, high transparency of > 82%, low roughness of 1 to 15 nm, and low sheet resistance of 10 to 20  $\Omega$ /square. Here, examples of PSC applicable TCOs include aluminium-doped zinc oxide (AZO), fluorine-doped tin oxide (FTO), and indium-doped tin oxide (ITO).

### 2.6.2: Electron Transport Materials

There are several types of materials that are being explored as ETLs. These range from  $\text{TiO}_2$ , tin (IV) oxide ( $\text{SnO}_2$ ), zinc oxide ( $\text{ZnO}$ ), and phenyl-C<sub>61</sub>-butyric- acid methyl ester (PCBM). The most common ETL currently used in PSCs is  $\text{TiO}_2$ .<sup>[75-78]</sup> However  $\text{TiO}_2$  has several disadvantages including an instability when exposed to ultraviolet (UV) light and low electron mobility.<sup>[79]</sup> The instability of  $\text{TiO}_2$  is compounded when it is used in the form of a mesoporous scaffold.<sup>[80]</sup> High-temperature-processes (HTPs) are usually used to eliminate organic content during the process of fabrication of  $\text{TiO}_2$  ETL. This is problematic as it reduces PSC compatibility with sensitive plastic substrates. It also potentially increases the cost of device manufacture and extends the energy payback time. In contrast, the ETL  $\text{Al}_2\text{O}_3$  and  $\text{ZnO}$  can be deposited without the use of a HTP,<sup>[81,82]</sup> but  $\text{ZnO}$  tends to be unstable as a result of the surface nature of  $\text{ZnO}$  layer. Such species then result in the decomposition of the perovskite absorbers.<sup>[83]</sup> Another compound that has similar properties to  $\text{TiO}_2$  is  $\text{SnO}_2$ . Here,  $\text{SnO}_2$  can be used to create high efficiency PSCs due to improved electrical and optical properties and favourable band

alignment to perovskite.<sup>[84-86]</sup> Here, its strong optical transparency is an essential feature for efficient operation in PV cells.<sup>[87]</sup>

### **2.6.3: Hole Transport Materials**

Several materials have been examined as HTLs, including 2,2',7,7'-tetrakis[N,N-di(4-methoxyphenyl)amine]-9,9'-spirobifluorene (spiro-OMeTAD or spiro),<sup>[88-90]</sup> poly-triarylamine (PTAA),<sup>[91-93]</sup> poly (3-hexylthiophene-2,5-diyl) (P3HT),<sup>[94-96]</sup> poly(3,4-ethylenedioxythiophene)-poly(styrenesulfonate) (PEDOT:PSS),<sup>[97-99]</sup> nickel oxide (NiO),<sup>[100-102]</sup> and other p-type materials. Here, Spiro-OMeTAD is the most widely used HTL and has been used in solar cells with a certified PCE of 23.48% in small cells.<sup>[103]</sup>

### **2.6.4: Device Contacts**

Materials such as carbon (C),<sup>[104,105]</sup> aluminium (Al),<sup>[98,100,106-108]</sup> silver (Ag),<sup>[20,109,110]</sup> and gold (Au)<sup>[111-113]</sup> have been used to perform the role of top electrode. The function of these materials is to extract charge from the device and deliver it to an external circuit. Such materials are generally deposited by thermal evaporation, however other techniques can be used such as sputtering<sup>[114]</sup> and doctor-blade coating.<sup>[104]</sup>

## **2.7: A Brief Review of the Development Process of Perovskite Solar Cells**

Organic-inorganic halide PSCs have become a hot research topic in the field of energy conversion. The perovskite MAPbI<sub>3</sub> gained first attention in 2009 when it was used as a semiconductor sensitizer in liquid electrolyte-based devices with a PCE of 3.8%. However, this efficiency rapidly degraded over a few minutes.<sup>[115]</sup> By

2011, a Korean group lead by Professor Park managed to improve device efficiency to 6.54%, while maintaining stability for 10 minutes in an electrolyte based perovskite quantum-dot-sensitized solar cell.<sup>[116]</sup> In 2012, Kim *et al.* revolutionized the development of PSCs by replacing the liquid HTL with a solid HTL. Here, an amorphous organic hole transport material (HTM) spiro was used for the first time creating a PSC, which reached a PCE of 9.7% with 500 hours certified stability.<sup>[117]</sup> This finding prompted Snaith *et al.* to retain the spiro HTL and substitute the TiO<sub>2</sub> mesoporous layer with Al<sub>2</sub>O<sub>3</sub> which increased device PCE to 10.9%.<sup>[118]</sup> This suggested that solid-state perovskite cells had unique advantages in comparison to devices using liquid electrolytes.<sup>[119]</sup> These advantages include convenience of device fabrication and ease of interconnection into modules. This potentially reduces the cost of device fabrication and utilisation.<sup>[120]</sup>

To improve device efficiency, Wang *et al.* incorporated graphene into a PSC to achieve a PCE of 15.6% in 2013.<sup>[121]</sup> Similar studies in 2015 observed a further improvement in efficiency to 20.1% through the development of perovskite materials based on formamidinium lead iodide (FAPbI<sub>3</sub>) with a PTAA HTL.<sup>[122]</sup> Zhou *et al.* achieved 19.3% efficiency when devices were fabricated in air, and used Yttrium doped into TiO<sub>2</sub> as an ETL leading to suppressed carrier recombination in the perovskite layer.<sup>[123]</sup> Despite significant effort, n-i-p architecture devices containing MAPbI<sub>3</sub> have not been reported with a PCE that exceeded 20%.<sup>[124-126]</sup>

Varying methods has been used to fabricate perovskites since 2013 and these techniques are shown in Figure 5. These methodologies include so-called 'one step' spin coating,<sup>[127-131]</sup> vapour deposition,<sup>[132-134]</sup> sequential deposition,<sup>[135-137]</sup> atomic layer deposition (ALD),<sup>[97,109,138]</sup> electrodeposition-assisted deposition,<sup>[139-141]</sup> and

vapor-assisted solution deposition.<sup>[142-144]</sup> Liu *et al.* devised a new methodology in 2013 to replace the widely used spin coating technique with a vapor deposition technique, which permitted a PCE of 15.4% to be demonstrated.<sup>[145]</sup>

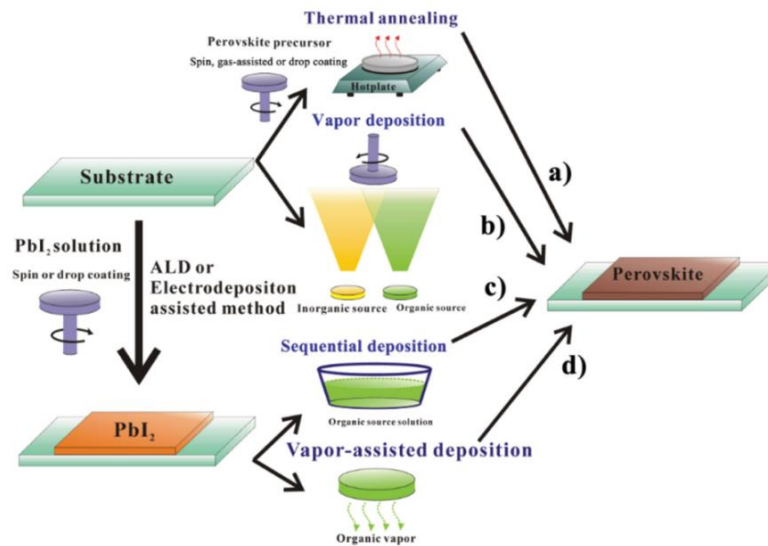


**Figure 5:** Taken from N. Tiep *et al.* <sup>[146]</sup> showing various methods to fabricate perovskite absorber layer: (a) “one step” method; such as spin and spray coating, (b) Vapor deposition, (c) sequential deposition (e.g. ALD-assisted and electrodeposition) and (d) vapor-assisted solution deposition.

Third generation PSCs have reached the threshold for commercialisation as they now demonstrate high efficiency, cost-effectiveness and convenience of fabrication. One of the most useful techniques to improve PSC efficiency has been through the use of chemical additives. For example, methylammonium chloride (MACl) has been used as an additive to different perovskite materials, enabling the achievement of high PCE devices. Jung *et al.* added MACl into mesoporous PSCs to increase the PCE to 22.7%.<sup>[96]</sup> MACl was also used by Jiang *et al.* and Kim *et al.* in a planar heterojunction device to demonstrate a PCE of 23.32%<sup>[147]</sup> and 23.48%<sup>[103]</sup> respectively. Major strides have been made to improve certified device efficiencies, with PCEs of 25.5% recorded on the NREL, Best Research-Cell Efficiency.<sup>[35]</sup> This

value should be compared with record the first- and second-generation devices in which PCE values of 27.6% and 23.4% have been reported for single crystal Si based solar cells and CIGS based solar cells respectively. Here, the high performance of perovskites can be attributed to several factors, including their high absorption coefficient, balanced electron-hole mobility and low-energy direct bandgap (~1.5 eV). Moreover, low exciton binding energies, high carrier mobility, high dielectric constants and long range charge diffusion lengths (100-1000 nm) also contribute favourably.<sup>[148-150]</sup>

Perovskite PV devices are however known to have stability issues.<sup>[151]</sup> Niu *et al.* have reported a detailed summary of the stability of PSCs, including their chemical stability, the effect of the environment (temperature, UV light, oxygen, moisture etc) and potential solutions for such issues.<sup>[152]</sup> Other known problems include the toxicity of perovskite compounds that contain the metal Pb. Such issues must be addressed before PSCs can become fully commercialised.<sup>[153]</sup>

### **2.7.1: Perovskite Compositional Engineering**

The chemical composition of perovskite materials is often modified through the partial substitution of A, B and X ions by organic or inorganic elements. This technique can be used to enhance device efficiency and long-term stability.<sup>[154]</sup> It has been found that perovskite stability problems can be associated with intrinsic structural properties, which affect the Goldschmidt tolerance factor. As described above, an ideal perovskite material has a tolerance factor that approaches unity, with deviations from this value indicating possible structural instability.<sup>[155]</sup> Around six years ago from 2021, MA based perovskites were commonly used in PSCs. However, Pellet *et al.* explored the combination FA and MA to create the perovskite

$(\text{MA})_x(\text{FA})_{1-x}\text{PbI}_3$  ( $X = 0 - 1$ ). This composition was shown to drive a significant improvement in the optical, structural and electrical properties of the resultant, leading to a PCE value of 14.9%.<sup>[156]</sup> Hao *et al.* then developed PSCs based on the mixed composition  $\text{MASn}_{1-x}\text{Pb}_x\text{I}_3$ , with perovskite band gap being tuneable from 1.17 to 1.55 eV via the modification of the Sn:Pb ratio. This composition was shown to improve the absorption of infra-red around 1.1 eV and thereby increase device  $J_{\text{sc}}$  from 14.16  $\text{mAcm}^{-2}$  to 20.64  $\text{mAcm}^{-2}$ .<sup>[157]</sup>

Yang *et al.* developed Perovskites based on the compositional mixture  $\text{MA}_{0.7}\text{FA}_{0.3}\text{Pb}(\text{I}_{0.9}\text{Br}_{0.1})_3$  perovskite, and achieved a PCE of 17.34%. This improvement in performance was achieved due to better morphology of the perovskite film whilst minimising the defect density and enhancing carrier lifetime.<sup>[158]</sup> In other work, Seok *et al.* used a similar perovskite composition to produce devices having an average PCE of 18.4%.<sup>[159]</sup> Zhang *et al.* then showed that incorporating a small quantity of Rb into the perovskite composition (creating  $\text{FA}_{0.80}\text{MA}_{0.15}\text{Rb}_{0.05}\text{PbI}_{2.55}\text{Br}_{0.45}$ ) allowed devices to be created having a PCE up to 20%.<sup>[160]</sup> A triple-cation perovskite was subsequently created by Saliba *et al.* based on a Cs-FA-MA composition. Here, the introduction of a small quantity of Cs to a double cation composition created devices that were more stable and reproducible, achieving PCE values of 21.1%.<sup>[63]</sup>

## 2.7.2: Perovskite Solvent Engineering

Solvents are used to create perovskite precursor solutions, or to treat a perovskite film using post-deposition techniques. The boiling points and polarities of the solvents used vary from one to another and hence can be used to modify a perovskite crystallisation process.<sup>[161]</sup> Here, a key technique known as solvent

engineering used to control a perovskite film morphology is the exposure of a drying film to an antisolvent. This process is accomplished by the deposition of a small quantity of solvent during spin-coating to a perovskite precursor film. This technique modifies the crystal nucleation process and can be used to enhance the morphology of a perovskite film. An antisolvent is chosen by considering its solubility in the perovskite precursor solvent, with chlorobenzene being widely used.<sup>[162-166]</sup> For example, Cheng *et al.* used chlorobenzene as an antisolvent to accelerate crystallisation and improve the uniformity of MAPbI<sub>3</sub> films, with devices created having a PCE of 13.9%.<sup>[167]</sup> Prochowicz *et al.* have used isopropanol as an antisolvent to produce perovskite films having a smoother surface and larger grain sizes than those produced using chlorobenzene.<sup>[168]</sup> The team lead by Seok have also used a hybrid casting solvent containing both  $\gamma$ -butyrolactone (GBL) and dimethylsulphoxide (DMSO) accompanied by toluene drop-casting exposure shortly after spin coating. This produced an intermediate phase PbI<sub>2</sub>•MAI•DMSO which slowed the perovskite crystallisation process. This led to the generation of a uniform and dense perovskite layer, generating devices which had a PCE of 16.2%.<sup>[161]</sup>

## 2.8: Stability of Perovskite Solar Cells

For PSCs to be a viable technology, they need to be able to maintain long-term operational stability. There has been considerable research performed to explore stability issues. Some such studies have focussed their attention on “gentle” aging tests. For example, some tests study stability of devices stored in the dark or when exposed to light at room temperature. Other tests explore devices run at 60 °C using light-emitting diode (LED) light sources either with or without UV filters (see below).<sup>[100,130,169-171]</sup> Commonly used aging tests often include exposure to UV light

soaking at a temperature between 40 °C and 85 °C, or when exposed to temperatures of 85 °C in an environment having a more than 50% relative humidity (RH).<sup>[92,96,110,172,173]</sup> To pass such tests, devices PSCs need to operate for 1000 hours continuously without losing more than 10% of their initial efficiency. The recorded stability and performance of PSCs developed over the last six years are summarised in Figure 6. It is evident that there over this time, there has been a tremendous improvement in device stability and performance. (Data in Figure 6 collected from the literature).<sup>[63,96,100,106,137,172,174–203]</sup>

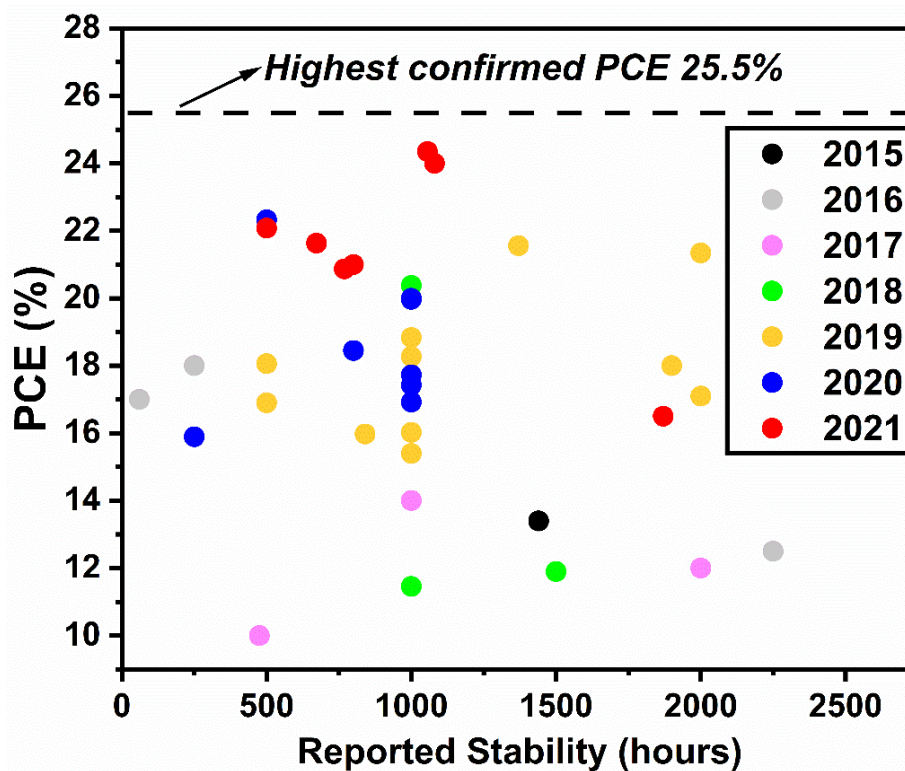


**Figure 6:** Development of PCE and stability of some PSCs that have been reported in the literature from 2015 until 2021.

The stability of the devices has improved as a result of the development of new light absorbing materials, improvements to device fabrication processes and greater understanding of the process of degradation. Chen *et al.* have reported the highest stability PSCs of more than 90% of initial PCE over a 1000 hours of light soaking

test.<sup>[204]</sup> This efficiency was achieved using doped inorganic layers to facilitate rapid charge extraction and to reduce degradation of the active perovskite material.<sup>[204]</sup> A summary of the reported stability of regular structure devices is shown in Table 1.

Perovskites are known to be highly sensitive to oxygen and moisture in their surrounding environment. In the presence of moisture, MAPbI<sub>3</sub> (CH<sub>3</sub>NH<sub>3</sub>PbI<sub>3</sub>) undergoes decomposition as summarised below.<sup>[205]</sup>



It is known that there are three main factors that affect the degradation process; exposure to UV radiation, oxygen (equation 8c) and moisture. Here, the product hydrogen iodide (HI) can either undergo a redox reaction (equation 8c) or decompose to H<sub>2</sub> and I<sub>2</sub> (equation 8d).<sup>[152]</sup> Noh *et al.* reported that the colour of a CH<sub>3</sub>NH<sub>3</sub>PbI<sub>3</sub> perovskite film changed from dark brown to yellow once the local humidity reached 55% signifying the start of decomposition.<sup>[130]</sup>

Device structure	$V_{oc}$ (V)	$J_{sc}$ ( $mAcm^{-2}$ )	FF (%)	PCE (%)	Degradation rate (%)	Measurement conditions	Ref
FTO/c-TiO <sub>2</sub> /Li doped mp-TiO <sub>2</sub> /Cs <sub>0.05</sub> (MA <sub>0.17</sub> FA <sub>0.83</sub> ) <sub>0.95</sub> Pb(I <sub>0.83</sub> Br <sub>0.17</sub> ) <sub>3</sub> /Spiro/Au	1.13	22.7	75	21.1	8	1 sun, N <sub>2</sub> atmosphere, 250 h	[63]
ITO/TiO <sub>2</sub> /Cs <sub>0.05</sub> MA <sub>0.03</sub> FA <sub>0.92</sub> Pb(I <sub>0.94</sub> Br <sub>0.06</sub> ) <sub>3</sub> /Spiro/Au	1.12	23.8	80.8	21.5	20	1 sun, 500 h	[137]
FTO/c-TiO <sub>2</sub> /mp-TiO <sub>2</sub> /FA <sub>x</sub> Cs <sub>1-x</sub> PbI <sub>3</sub> /Spiro/Au	1.15	24	75	20.9	≈ 2	White LED light, ambient air, 55-60 °C, 1000 h	[174]
FTO/c-TiO <sub>2</sub> /mp-TiO <sub>2</sub> /SnO <sub>2</sub> /triple-cation perovskite/MeSBA-DMPA/Au	1.06	22.75	75.3	18.21	12	1 sun, 25 °C, 1020 h	[179]
FTO/d-TiO <sub>2</sub> /mp-TiO <sub>2</sub> /(FAPbI <sub>3</sub> ) <sub>0.95</sub> (MAPbI <sub>3</sub> ) <sub>0.05</sub> /PTAA/Au	N/A	N/A	N/A	20	≈ 4	1 sun, UV, ambient condition, 1000 h	[180]
FTO/Ru:SnO <sub>2</sub> /Cs <sub>0.05</sub> (MA <sub>0.10</sub> FA <sub>0.90</sub> ) <sub>0.95</sub> Pb(I <sub>0.90</sub> Br <sub>0.10</sub> ) <sub>3</sub> /Zn-TFSI <sub>2</sub> :Spiro/Au	1.15	24.6	78	22	3	1 sun, 2000 h	[181]
FTO/TiO <sub>2</sub> /FA <sub>0.85</sub> MA <sub>0.15</sub> Pb(I <sub>0.85</sub> Br <sub>0.15</sub> ) <sub>3</sub> /MnS/Au	1.11	23.4	76.5	19.9	20	1 sun, 85 °C, 80% RH, ambient air, 500 h	[182]
FTO/c-TiO <sub>2</sub> /mp-TiO <sub>2</sub> /(CsFAMA)Pb(I <sub>1-x</sub> Br <sub>x</sub> ) <sub>3</sub> /CuSCN/C	1.01	23.4	76.5	18.1	5	Full sun, 60 °C, 2000 h	[185]
FTO/CsF:SnO <sub>2</sub> /Cs <sub>0.05</sub> (MA <sub>0.15</sub> FA <sub>0.85</sub> ) <sub>0.95</sub> Pb(I <sub>0.85</sub> Br <sub>0.15</sub> ) <sub>3</sub> /D4 TBP/Spiro/Au	1.16	23.2	76	20.5	>10	White LED, N <sub>2</sub> atmosphere, 25 °C, 800 h	[186]
FTO/bl-TiO <sub>2</sub> /mp-TiO <sub>2</sub> /TPA <sub>x</sub> MA <sub>(1-x)</sub> PbI <sub>3</sub> (4%)/Spiro/Au	1.12	22.1	71.9	17.8	>20	Full sun, 25 °C, 250 h	[187]
FTO/c-TiO <sub>2</sub> /mp-TiO <sub>2</sub> /Cs <sub>0.05</sub> FA <sub>0.85</sub> MA <sub>0.10</sub> Pb(I <sub>0.97</sub> Br <sub>0.03</sub> ) <sub>3</sub> /tBBAl/Spiro/Au	1.14	25.1	82.1	23.5	5	1 sun, N <sub>2</sub> atmosphere, 500 h	[188]
ITO/SnO <sub>2</sub> /Rb <sub>0.09</sub> Cs <sub>0.05</sub> [(FA <sub>0.85</sub> MA <sub>0.15</sub> ) <sub>0.95</sub> Pb(I <sub>0.85</sub> Br <sub>0.15</sub> ) <sub>3</sub> ]/Spiro/Au	1.16	23.56	76.25	20.84	≈ 20	1 sun, ambient condition, 1000 h	[189]
FTO/c-TiO <sub>2</sub> /mp-TiO <sub>2</sub> /K <sub>0.10</sub> Cs <sub>0.06</sub> FA <sub>0.79</sub> MA <sub>0.15</sub> Pb(I <sub>0.85</sub> Br <sub>0.15</sub> ) <sub>3</sub> /Spiro/Au	1.17	23.2	79	21.5	> 30	1 sun, N <sub>2</sub> atmosphere, 40 °C, 350 h	[206]

**Table 1:** Solar cells stability at MPP (regular structure devices) from literature (ISOS L-1).

Niu *et al.* reported that upon exposure to both oxygen and moisture, perovskite degradation becomes an irreversible process.<sup>[205]</sup> As the crystal structure of the

perovskite material affects its optoelectronic properties such as carrier mobility, band gap and absorption, changes in crystalline structure can lead to a significant reduction in optoelectronic properties.<sup>[73]</sup> It has also been found that low bandgap Sn-based perovskite devices demonstrated reduced performance and stability. This is mainly due to the oxidation of tin (II) ( $\text{Sn}^{2+}$ ) to form  $\text{Sn}^{4+}$  when exposed to air. This results in an increase in the density of trap-states, leading to reduction in operational stability and performance.<sup>[207-209]</sup> This inherent weakness can be corrected with the use of additives to minimise the  $\text{Sn}^{2+}$  oxidation seen in Sn-halide perovskites. For example, Tai *et al.* used a hydroxybenzene sulfonic acid additive as an antioxidant in the perovskite precursor along with excess tin (II) chloride ( $\text{SnCl}_2$ ). This made it possible to fabricate formamidinium tin iodide ( $\text{FASnI}_3$ ) solar cells that are more resistant to degradation in air. Such devices retained 80% of their initial performance over 500 hours when exposed to air without encapsulation.<sup>[210]</sup> Ion migration in the presence of a bias voltage or thermal drift is also known to reduce PSCs stability.<sup>[211]</sup> This process is shown schematically in Figure 7.

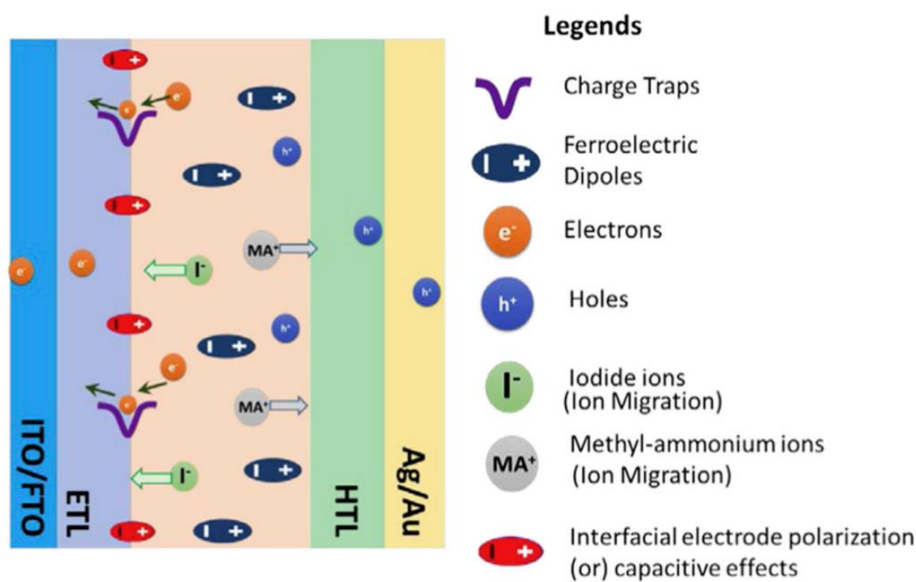


**Figure 7:** Taken from N. Elumalai *et al.*<sup>[212]</sup> Schematic diagram shows the ion/defects movements within the device structure.

Long-term stability of perovskite in the presence of moisture has been improved following the use of various additives (in the form of polymers and molecules). Such additives often contain a hydrophobic ammonium or carbonyl group that interact with the perovskites at its surface or grain boundary and prevent damage due to moisture (Figure 8). Zhao *et al.* were able to enhance perovskite stability through the addition of a hygroscopic PEG scaffold. This caused the film to develop a self-regenerating behaviour, with unencapsulated devices maintaining high efficiency for approximately 300 hours in a humid environment (70% RH).<sup>[213]</sup> An alternative method to enhance stability was demonstrated by Gao *et al.* who generated Pb-S bonds at the surface of a perovskite film through the addition of the additive thiourea. Following exposure to normal air for two months, PSCs retained 98% and 93% of their efficiency, with devices having active areas of 0.1 and 1.0 cm<sup>2</sup> respectively.<sup>[214]</sup>

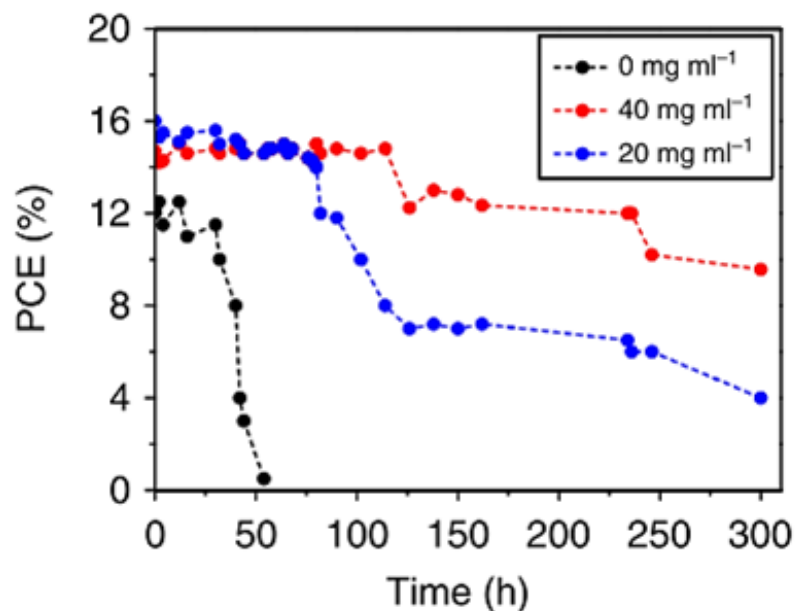


**Figure 8:** Taken from Y. Zhao *et al.*<sup>[213]</sup> showing PCE as a function of time of PSCs with and without scaffold exposed in high humidity atmosphere (70% RH) dark environment without encapsulation.

Zuo *et al.* attempted to modify the composition of a MAPbI<sub>3</sub> perovskite film through the incorporation of poly(4-vinylpyridine) (PVP). This resulted in the formation of devices retaining 85% of initial efficiency over 100 days under dark storage (e.g. corresponding to an operational 'shelf life').<sup>[215]</sup> Jiang *et al.* explored using a number of polymers such as p-type and n-type semiconductors and a traditional insulator dispersed into a perovskite layer to develop a network between grain boundaries and thereby enhance film stability. This approach enhanced device PCE to 19.19% and resulted in improved stability compared to undoped devices.<sup>[216]</sup> Zong *et al.* used a triblock copolymer (TBCP) having hydrophilic–hydrophobic–hydrophilic symmetric blocks which enabled grain boundaries to be functionalised. The optimised perovskite devices had a PCE of 19.4% and retained 92% of the initial PCE over a period of 480 hours.<sup>[217]</sup> This approach was improved by Li *et al.* through the addition of the hydrophobic additive trimethylolpropane triacrylate (TMTA) to a MAPbI<sub>3</sub> perovskite films. Following thermal treatment, it was claimed that TMTA stabilised grain boundaries, with thermal, UV and moisture stability of the cross-linked TMTA-based devices being enhanced when tested under one sun for 400 hours. Such devices showed remarkable resilience to heat and moisture, exceeding 90% of the initial performance after 1000 hours.<sup>[218]</sup> Notably however, the degradation in charge transport layers caused by chemical reactions occurring with device electrodes is also known to substantially reduce PSC stability.<sup>[219,220]</sup>

### **2.8.1: Thermal Instability**

In general, when solar cells are operated in direct sunlight, the temperature of the device can exceed ambient temperature by 45 °C. According to the international standard (IEC 61646 climatic chamber tests), it is essential for PV devices to have

long-term stability at 85 °C to be competitive with other PV technologies and presumably to be considered stable enough for commercialisation. Temperature is a significant factor that can influence the phase transition of a perovskite; a process that can potentially lead to the thermal decomposition of a PSC. Each material in a device generally has a different phase transition temperature.<sup>[221]</sup> Dualeh *et al.* used thermogravimetric analysis (TGA) to evaluate the thermal stability of MAPbX<sub>3</sub> (X = I, Cl). Here, it was observed that the organic component of MAPbX<sub>3</sub> (X = I, Cl) undergoes thermal decomposition to HI and methylamine (CH<sub>3</sub>NH<sub>2</sub>).<sup>[222]</sup> Another study used aging test to assess relative thermal stability and showed that methylammonium lead bromide (MAPbBr<sub>3</sub>) is more stable than MAPbI<sub>3</sub>; an effect that results from a variation in the bond strength and the specific crystalline structure of each compound.<sup>[223]</sup> Mozaffari *et al.* has found that the replacement of the organic cation MA with FA causes a decrease in the band gap which results in much higher thermal stability.<sup>[224]</sup>

Kim *et al.* studied the degradation of spiro-OMeTAD and the MAPbI<sub>3</sub>/spiro-OMeTAD interface resulting from ion migration driven by thermal annealing. It was found that no significant change occurred in a MAPbI<sub>3</sub> film held at 85 °C for a short period of time. However the presence of spiro-OMeTAD and the interface present between MAPbI<sub>3</sub>/spiro-OMeTAD were affected due to the migration of I<sup>-</sup> and MA<sup>+</sup>. At higher temperatures, it was found that the I-ions moved into the spiro-OMeTAD and acted as reducing agents. It was also evident that the I-ions moved in the form of MAI, as demonstrated by the presence of MA on the surface of the spiro-OMeTAD. Indeed, it has been speculated that PSC degradation at 85 °C is caused by spiro-OMeTAD rather than the decomposition of MAPbI<sub>3</sub>.<sup>[225]</sup>

## 2.8.2: Environmental Instability

The exposure to oxygen can cause an oxidation of the organic components within a device. However, there is no sign of degradation when PSCs are kept in dry air in the dark.<sup>[117,118]</sup> There is however considerable degradation that occurs to a perovskite when it is exposed to moisture. Perovskites are capable of absorbing moisture from the ambient environment which results in the formation of hydrate products such as  $\text{MA}_4\text{PbI}_6 \cdot 2\text{H}_2\text{O}$  owing to the extremely hydrophilic property of amine salts.<sup>[226]</sup>  $\text{MAPbI}_{3-x}\text{Cl}_x$  and  $\text{MAPbI}_3$  both show similar behavioural patterns of moisture-related degradation with a pure  $\text{PbI}_2$  phase formed.<sup>[227]</sup> Niu *et al.* examined the various decomposition processes that occur in  $\text{MAPbI}_3$ . Here,  $\text{TiO}_2/\text{MAPbI}_3$  films were held at a temperature of 35 °C at 60% RH for 18 hours, with optical absorption and perovskite crystal structure monitored before and after the experiment. Here, changes observed in  $\text{MAPbI}_3$  indicated that it underwent decomposition as described earlier in equations 8(a-c).<sup>[205]</sup> Leguy *et al.* studied the different effects of water vapor and liquid water on perovskite films. It was found that exposure of  $\text{CH}_3\text{NH}_3\text{PbI}_3$  to water vapor at room temperature for a prolonged period of time resulted in the formation of  $\text{CH}_3\text{NH}_3\text{PbI}_3 \cdot \text{H}_2\text{O}$  which then formed  $(\text{CH}_3\text{NH}_3)_4\text{PbI}_6 \cdot 2\text{H}_2\text{O}$ . Upon drying, the perovskite films, it was found that this process could be completely reversed.<sup>[228]</sup> It was also shown that when exposed to water vapor, devices suffered a drop in  $J_{\text{sc}}$  by 90% and a loss of 200 mV in  $V_{\text{oc}}$ . However, these values returned to their normal range upon storage in dry nitrogen for approximately 6 hours. Following dehydration, the device  $J$ - $V$  curve was found to demonstrate a high degree of hysteresis. This change was attributed to an alteration in the film morphology and an increase in its density. In comparison to water vapor, exposure to liquid water drove an irreversible degradation of  $\text{MAPbI}_3$

to  $\text{PbI}_2$ .<sup>[228]</sup> Dong *et al.* modelled the process of degradation in perovskite structure, and explored the strength of different chemical bonds between the organic and inorganic compounds. It was found that the stability of  $\text{MAPbI}_3$  can be chiefly attributed to the hydrogen bond interactions present between the inorganic  $\text{PbI}_2$  and organic MAI. Furthermore, it was proposed that  $\text{MAPbI}_3$  underwent complete decomposition in the presence of two water molecules through the breakage of the hydrogen bond between  $\text{PbI}_2$  and MAI.<sup>[229]</sup> Yang *et al.* explored that the effect of humidity level and how it influences the process of degradation in perovskites. It was shown that HTLs play an important role in influencing the stability of  $\text{MAPbI}_3$  when exposed to a humid environment, suggesting that the quality of the HTL is important in building stable devices.<sup>[230]</sup>

The majority of laboratory experiments to explore the effect of UV radiation on PSC stability, have been done using controlled light sources such as LEDs which mimic the UV component of sunlight which is known to drive degradation.<sup>[231]</sup> Leijtens *et al.* studied the effect of UV radiation on PSCs and it was found that encapsulation of the PSCs using  $\text{TiO}_2$  in nitrogen environment resulted in rapid degradation in  $J_{sc}$  and PCE. In contrast, unencapsulated perovskite devices had greater stability.<sup>[80]</sup>

## **2.9: Strategies to Improve the Stability of Perovskite Solar Cells**

There have been countless trials conducted to enhance the resistance to PSC degradation caused by the effect of moisture. For example, Guarnera *et al.* demonstrated that the stability of perovskite devices can be extended through the use of an insulating mesoporous “buffer layer”. This layer consisted of  $\text{Al}_2\text{O}_3$  nanoparticles spread between a metal electrode and the perovskite layer. Here,  $\text{Al}_2\text{O}_3$  acts to minimise degradation by preventing the formation of shorts between

the top electrode and the perovskite film and allowed devices to be created that were stable for 350 hours.<sup>[232]</sup>

### **2.9.1.1: Humidity**

Stability issues can result from the lithium (Li)-salt dopants added to the spiro-OMeTAD. These dopants lower the stability of PSCs due to their sensitivity to water and this necessitates the use of a high level of device encapsulation.<sup>[80]</sup> Bass *et al.* demonstrated that humidity can accelerate the crystallisation of perovskite films.<sup>[233]</sup> Zheng *et al.* showed that inserting ammonium iodide (NH<sub>4</sub>I) as an interfacial layer between the TiO<sub>2</sub> and perovskite improved the quality of films and the efficiency of electron extraction. These devices showed high stability over 700 hours at 80% RH.<sup>[234]</sup> Sidhik *et al.* also found that by using a high-purity lead sulfide quantum dots (PbS QDs) as interfacial layer between perovskite and spiro-OMeTAD, devices had improving stability at 70% RH (retaining 76% of initial PCE over 1440 hours).<sup>[235]</sup>

### **2.9.1.2: UV**

Degradation as a result of UV exposure can be overcome by adding an UV filter before the TiO<sub>2</sub> ETL; a strategy that prevents the absorption UV light by TiO<sub>2</sub>. Chander *et al.* exploited this effect and used a transparent luminescent down-shifting (DS) Europium (Eu<sup>3+</sup>) doped yttrium vanadate (YVO<sub>4</sub>) nano-phosphor layer to fabricate TiO<sub>2</sub> based PSCs. This layer was able to absorb UV light and emit visible light which then could be absorbed by perovskite layer leading to enhanced stability, whilst retaining over 50% of the initial efficiency.<sup>[171]</sup> Roose *et al.* showed that by replacing the TiO<sub>2</sub> ETL with SnO<sub>2</sub> devices could be run under UV light for 10 hours.<sup>[236]</sup>

### 2.9.1.3: Thermal

Li *et al.* demonstrated an improvement in stability in a triple-layer architecture device composed of MAPbI<sub>3</sub> infiltrated layers of mp-TiO<sub>2</sub> and mp-zirconium (IV) oxide (ZrO<sub>2</sub>), with C as a back contact. Such devices were tested for three months at temperature of 80 to 85 °C in the deserts of Saudi Arabia as well as indoors and both showed high stability.<sup>[237]</sup> Numerous researchers have attempted to enhance the thermal stability of PSCs through the replacement of the MA cation with other cations such as FA or<sup>[159]</sup> Cs cations,<sup>[131]</sup> or a mixture of both. Other groups have used double and triple-cation based perovskites to enhance thermal stability of PSCs. For example, Cs-FA mixture-based PSCs were shown to have enhanced stability in comparison to pristine FAPbI<sub>3</sub> in the presence of light, heat and moisture.<sup>[238]</sup> Saliba *et al.* introduced the fabrication of a triple-cation perovskite composition which demonstrated greater thermal stability, reduced phase impurities and minimal sensitivity to processing conditions.<sup>[63]</sup> It has also been shown that PSCs using a PTAA HTL which incorporated Rb into a triple-cation perovskite had improved thermal stability. Such devices demonstrated a PCE in excess of 20% and maintained 92% of their starting efficiency after stress testing at 85 °C and 85% RH for 1000 hours according to international standards (IEC 61215).<sup>[173]</sup>

### **2.9.2: Encapsulation**

Encapsulation is an important process used to enhance stability of perovskite devices. Here, encapsulation can be placed on the front and/or back of a PSC device. This process is designed to exclude water and oxygen in the environmental from the devices. Several studies have been conducted to estimate the effectiveness of encapsulation on solar cell devices. Bella *et al.* showed that encapsulation created devices that were stable over 6 months.<sup>[239]</sup> Cavity glass and UV-curable resins have been used to encapsulate  $\text{MAPbI}_{3-x}\text{Cl}_x$  perovskite devices. Here, such devices have been shown to maintaining 90% of their original PCE for more than 70 days under ambient environment conditions.<sup>[240]</sup> The use of UV activated glue has been used in PSCs to create highly stable and efficient devices that maintained 90% of their initial performance over 1000 hours.<sup>[204]</sup>

### **2.9.3: Current-Voltage Hysteresis**

Solar cells are characterised by recording a  $J-V$  curve. It has been found that hysteresis in the  $J-V$  characteristics appears correlated with perovskite device performance and long-term stability. In high efficiency PSCs, ion migration within a perovskite crystal has a significant influence on hysteresis.<sup>[156,241]</sup> Experiments to analyse this particular effect have shown that the ion migration along the grain boundaries is a key reason for hysteresis.<sup>[242]</sup> Such hysteresis is manifest by changes in the  $J-V$  curve that is dependent upon the direction of scan and the scan rate as shown in Figure 9. Here, a 'reverse' or 'backward' scan is one where the voltage is altered from positive (open-circuit) to negative (short-circuit). Alternatively, when the scan is done in the opposite direction, it is known as a 'forward' scan. It has been

found that reverse scans apparently yield a larger estimate of PV efficiency in comparison to forward scans.<sup>[212]</sup>

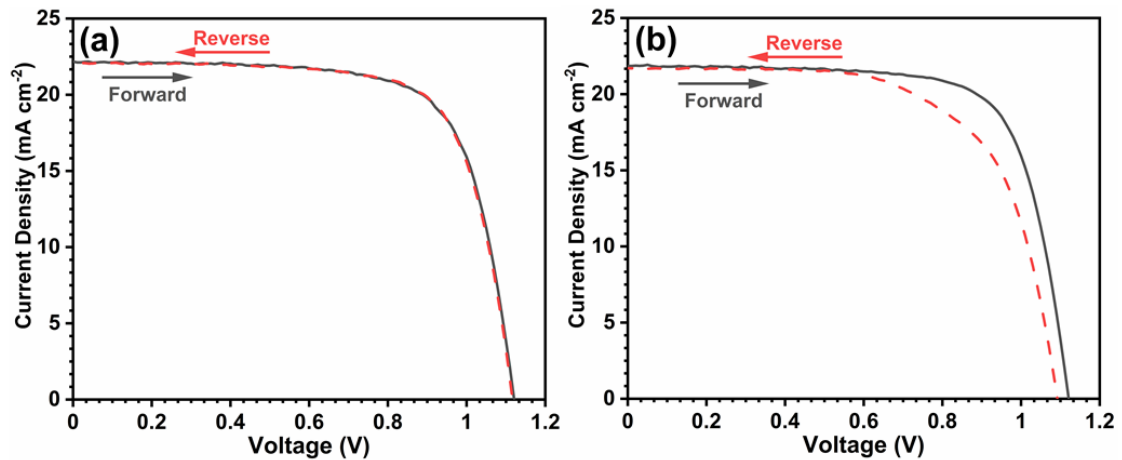


**Figure 9:** Shows  $J$ - $V$  curve (a) with negligible hysteresis and (b) with hysteresis of PSCs.

Hysteresis mainly results from the low activation energy for the migration of ions within a perovskite layer.<sup>[243–245]</sup> This can result in significant ionic diffusion when a perovskite is placed under thermal stress, subject to external electronic bias or placed under illumination.<sup>[246]</sup>  $I^-$  ions possess the ability to move through polycrystalline perovskite grains and even reach the device electrode. This process can cause the formation of defects which become nonradiative recombination sites (e.g. at grain boundaries or other interfaces).<sup>[247]</sup> Domanski *et al.* demonstrated that halide migration occurs upon application of an electric field, with halide vacancies collecting at the interface with the hole selective contact over timescales ranging from  $10^{-1}$  to  $10^2$  s. Such effects are apparent from a hysteresis in the PSC  $J$ - $V$  curves.<sup>[248]</sup>

Several studies have also shown that the migration of ionic species within a perovskite results in transient and slow dynamic processes, with ion migration playing a vital part in defining long-term stability. It has generally been concluded

that prevention of the formation of ionic defects is key in maintaining long-term stability.<sup>[248-250]</sup> Experimental work has shown that  $J$ - $V$  hysteresis is weak when there is low charge-carrier surface recombination and long carrier-diffusion length.<sup>[251]</sup> Such processes can potentially be improved by enhancing perovskite crystallinity, fabrication processes and optimising device contacts. HTMs have been found to have an effect on  $J$ - $V$  hysteresis, with a copper zinc tin sulphide ( $\text{Cu}_2\text{ZnSnS}_4$ ) HTM having less hysteresis than spiro-OMeTAD.<sup>[252]</sup> Hysteresis effects directly affect measured performance parameters,<sup>[253]</sup> however, Kim *et al.* showed that inverted planar p-i-n structured devices show minimal hysteresis compared to normal planar n-i-p devices.<sup>[254]</sup> Indeed Saliba *et al.* show that triple-cation perovskite exhibit significantly reduced hysteresis.<sup>[63]</sup>

## 2.10: Summary

In this chapter, I have reviewed the structure and operation of perovskite photovoltaics, and in particular have reviewed progress in the development of devices having improved stability. I draw upon this, and in Chapter 4, I explore the relative stability of two popular perovskite materials formulation and in particular compare devices that utilise two different hole transport materials. This theme continuous in Chapter 5 where I investigate the role of passivating potassium iodide (KI) on improving the efficiency and stability of triple-cation perovskites. Here, I show that defect passivation using KI is highly sensitive to the perovskite/electron transport layer interface and can leading to reduce the stability of the resultant PSCs.

## 2.11: References

- [1] T. R. Cook, D. K. Dogutan, S. Y. Reece, Y. Surendranath, T. S. Teets, D. G. Nocera, *Chem. Rev.* **2010**, *110*, 6474.
- [2] H. Du, C. X. Zhao, J. Lin, J. Guo, B. Wang, Z. Hu, Q. Shao, D. Pan, E. K. Wujcik, Z. Guo, *Chem. Rec.* **2018**, *18*, 1365.
- [3] C. Lin, L. Hu, C. Cheng, K. Sun, X. Guo, Q. Shao, J. Li, N. Wang, Z. Guo, *Electrochim. Acta* **2018**, *260*, 65.
- [4] M. Idrees, S. Batool, J. Kong, Q. Zhuang, H. Liu, Q. Shao, N. Lu, Y. Feng, E. K. Wujcik, Q. Gao, T. Ding, R. Wei, Z. Guo, *Electrochim. Acta* **2019**, *296*, 925.
- [5] Y. Zhang, L. Qian, W. Zhao, X. Li, X. Huang, X. Mai, Z. Wang, Q. Shao, X. Yan, Z. Guo, *J. Electrochem. Soc.* **2018**, *165*, H510.
- [6] X. Lou, C. Lin, Q. Luo, J. Zhao, B. Wang, J. Li, Q. Shao, X. Guo, N. Wang, Z. Guo, *ChemElectroChem* **2017**, *4*, 3171.
- [7] W. Zhao, X. Li, R. Yin, L. Qian, X. Huang, H. Liu, J. Zhang, J. Wang, T. Ding, Z. Guo, *Nanoscale* **2019**, *11*, 50.
- [8] C. Wang, B. Mo, Z. He, Q. Shao, D. Pan, E. Wujick, J. Guo, X. Xie, X. Xie, Z. Guo, *J. Memb. Sci.* **2018**, *556*, 118.
- [9] B. Seger, P. V. Kamat, *J. Phys. Chem. C* **2009**, *113*, 7990.
- [10] A. Dubey, N. Adhikari, S. Mabrouk, F. Wu, K. Chen, S. Yang, Q. Qiao, *J. Mater. Chem. A* **2018**, *6*, 2406.
- [11] K.-S. Lee, J. S. Spendelow, Y.-K. Choe, C. Fujimoto, Y. S. Kim, *Nat. Energy* **2016**, *1*, 16120.
- [12] J. Jia, L. C. Seitz, J. D. Benck, Y. Huo, Y. Chen, J. W. D. Ng, T. Bilir, J. S. Harris, T. F. Jaramillo, *Nat. Commun.* **2016**, *7*, 13237.
- [13] Y. Kuang, Q. Jia, G. Ma, T. Hisatomi, T. Minegishi, H. Nishiyama, M. Nakabayashi, N. Shibata, T. Yamada, A. Kudo, K. Domen, *Nat. Energy* **2017**, *2*, 16191.

- [14] J. Gu, J. A. Aguiar, S. Ferrere, K. X. Steirer, Y. Yan, C. Xiao, J. L. Young, M. Al-Jassim, N. R. Neale, J. A. Turner, *Nat. Energy* **2017**, *2*, 16192.
- [15] G. Zheng, J. Wang, H. Liu, V. Murugadoss, G. Zu, H. Che, C. Lai, H. Li, T. Ding, Q. Gao, Z. Guo, *Nanoscale* **2019**, *11*, 18968.
- [16] C. Feng, *Int. J. Electrochem. Sci.* **2019**, *14*, 8284.
- [17] H. Li, T. Lv, H. Sun, G. Qian, N. Li, Y. Yao, T. Chen, *Nat. Commun.* **2019**, *10*, 536.
- [18] C. Zhang, L. McKeon, M. P. Kremer, S.-H. Park, O. Ronan, A. Seral-Ascaso, S. Barwich, C. Ó. Coileáin, N. McEvoy, H. C. Nerl, B. Anasori, J. N. Coleman, Y. Gogotsi, V. Nicolosi, *Nat. Commun.* **2019**, *10*, 1795.
- [19] Z. Tian, X. Tong, G. Sheng, Y. Shao, L. Yu, V. Tung, J. Sun, R. B. Kaner, Z. Liu, *Nat. Commun.* **2019**, *10*, 4913.
- [20] L. Yang, X. Wang, X. Mai, T. Wang, C. Wang, X. Li, V. Murugadoss, Q. Shao, S. Angaiah, Z. Guo, *J. Colloid Interface Sci.* **2019**, *534*, 459.
- [21] M. M. Tavakoli, D. Prochowicz, P. Yadav, R. Tavakoli, M. Saliba, *Eng. Sci.* **2018**, *2*, 48.
- [22] M. He, X. Pang, X. Liu, B. Jiang, Y. He, H. Snaith, Z. Lin, *Angew. Chemie Int. Ed.* **2016**, *55*, 4280.
- [23] Q. Hou, J. Ren, H. Chen, P. Yang, Q. Shao, M. Zhao, X. Zhao, H. He, N. Wang, Q. Luo, Z. Guo, *ChemElectroChem* **2018**, *5*, 726.
- [24] M. He, D. Zheng, M. Wang, C. Lin, Z. Lin, *J. Mater. Chem. A* **2014**, *2*, 5994.
- [25] P. Panneerselvam, V. Murugadoss, V. Elayappan, N. Lu, Z. Guo, S. Angaiah, *ES Energy Environ.* **2018**, 99.
- [26] S. Angaiah, V. Murugadoss, S. Arunachalam, P. Panneerselvam, S. Krishnan, *Eng. Sci.* **2018**, 1.
- [27] J. Xu, Y. Chen, L. Dai, *Nat. Commun.* **2015**, *6*, 8103.
- [28] J. Zhao, Y. Li, G. Yang, K. Jiang, H. Lin, H. Ade, W. Ma, H. Yan, *Nat. Energy* **2016**,

1, 15027.

- [29] K. Yoshikawa, H. Kawasaki, W. Yoshida, T. Irie, K. Konishi, K. Nakano, T. Uto, D. Adachi, M. Kanematsu, H. Uzu, K. Yamamoto, *Nat. Energy* **2017**, *2*, 17032.
- [30] N. G. Park, M. Grätzel, T. Miyasaka, *Organic-Inorganic Halide Perovskite Photovoltaics*, Springer International Publishing, Cham, **2016**.
- [31] J. Yan, M. J. Uddin, T. J. Dickens, O. I. Okoli, *Sol. Energy* **2013**, *96*, 239.
- [32] W. G. Adams, R. E. Day, *Proc. R. Soc. London* **1877**, *25*, 113.
- [33] A. Fahrenbruch, R. Bube, *Fundamentals of Solar Cells: Photovoltaic Solar Energy Conversion.*, Elsevier, **2012**.
- [34] D. M. Chapin, C. S. Fuller, G. L. Pearson, *J. Appl. Phys.* **1954**, *25*, 676.
- [35] NREL, "Best Research-Cell Efficiency Chart," **2021**.
- [36] W. Liu, T. Wu, M. Liu, W. Niu, Y. Chueh, *Adv. Mater. Interfaces* **2019**, *6*, 1801758.
- [37] J. A. del Cueto, S. Rummel, B. Kroposki, A. Anderberg, in *Photovolt. Cell Modul. Technol. II* (Eds.: B. von Roedern, A.E. Delahoy), **2008**, p. 704504.
- [38] J. Burschka, N. Pellet, S.-J. Moon, R. Humphry-Baker, P. Gao, M. K. Nazeeruddin, M. Grätzel, *Nature* **2013**, *499*, 316.
- [39] N.-G. Park, *J. Phys. Chem. Lett.* **2013**, *4*, 2423.
- [40] H.-S. Kim, S. H. Im, N.-G. Park, *J. Phys. Chem. C* **2014**, *118*, 5615.
- [41] W.-Q. Wu, D. Chen, R. A. Caruso, Y.-B. Cheng, *J. Mater. Chem. A* **2017**, *5*, 10092.
- [42] H. Borchert, *Solar Cells Based on Colloidal Nanocrystals*, Springer International Publishing, Cham, **2014**.
- [43] B. Qi, J. Wang, *J. Mater. Chem.* **2012**, *22*, 24315.
- [44] W. Shockley, H. J. Queisser, *J. Appl. Phys.* **1961**, *32*, 510.
- [45] J. P. Attfield, P. Lightfoot, R. E. Morris, *Dalt. Trans.* **2015**, *44*, 10541.

- [46] D. Weber, *Zeitschrift für Naturforsch. B* **1978**, *33*, 1443.
- [47] Z. Xiao, Y. Yan, *Adv. Energy Mater.* **2017**, *7*, 1701136.
- [48] B.-H. Chen, *J. Solid State Chem.* **1996**, *125*, 63.
- [49] M. A. Green, A. Ho-Baillie, H. J. Snaith, *Nat. Photonics* **2014**, *8*, 506.
- [50] C. J. Bartel, C. Sutton, B. R. Goldsmith, R. Ouyang, C. B. Musgrave, L. M. Ghiringhelli, M. Scheffler, *Sci. Adv.* **2019**, *5*, eaav0693.
- [51] A. Amat, E. Mosconi, E. Ronca, C. Quarti, P. Umari, M. K. Nazeeruddin, M. Grätzel, F. De Angelis, *Nano Lett.* **2014**, *14*, 3608.
- [52] H. Zhang, X. Qiao, Y. Shen, T. Moehl, S. M. Zakeeruddin, M. Grätzel, M. Wang, *J. Mater. Chem. A* **2015**, *3*, 11762.
- [53] S. De Wolf, J. Holovsky, S.-J. Moon, P. Löper, B. Niesen, M. Ledinsky, F.-J. Haug, J.-H. Yum, C. Ballif, *J. Phys. Chem. Lett.* **2014**, *5*, 1035.
- [54] C. C. Stoumpos, M. G. Kanatzidis, *Adv. Mater.* **2016**, *28*, 5778.
- [55] J. S. Manser, J. A. Christians, P. V. Kamat, *Chem. Rev.* **2016**, *116*, 12956.
- [56] B. R. Sutherland, E. H. Sargent, *Nat. Photonics* **2016**, *10*, 295.
- [57] J. M. Ball, A. Petrozza, *Nat. Energy* **2016**, *1*, 16149.
- [58] Y. Zhao, K. Zhu, *Chem. Soc. Rev.* **2016**, *45*, 655.
- [59] Y. Zhao, K. Zhu, *J. Phys. Chem. Lett.* **2014**, *5*, 4175.
- [60] J. S. Manser, M. I. Saidaminov, J. A. Christians, O. M. Bakr, P. V. Kamat, *Acc. Chem. Res.* **2016**, *49*, 330.
- [61] W. Zhang, G. E. Eperon, H. J. Snaith, *Nat. Energy* **2016**, *1*, 16048.
- [62] L. Wang, K. Wang, B. Zou, *J. Phys. Chem. Lett.* **2016**, *7*, 2556.
- [63] M. Saliba, T. Matsui, J.-Y. Seo, K. Domanski, J.-P. Correa-Baena, M. K. Nazeeruddin, S. M. Zakeeruddin, W. Tress, A. Abate, A. Hagfeldt, M. Grätzel, *Energy Environ. Sci.* **2016**, *9*, 1989.

- [64] J. Wang, J. Peng, Y. Sun, X. Liu, Y. Chen, Z. Liang, *Adv. Electron. Mater.* **2016**, *2*, 1600329.
- [65] Z. Tang, T. Bessho, F. Awai, T. Kinoshita, M. M. Maitani, R. Jono, T. N. Murakami, H. Wang, T. Kubo, S. Uchida, H. Segawa, *Sci. Rep.* **2017**, *7*, 12183.
- [66] Z. Liu, B. Sun, X. Liu, J. Han, H. Ye, T. Shi, Z. Tang, G. Liao, *Nano-Micro Lett.* **2018**, *10*, 34.
- [67] S.-H. Turren-Cruz, A. Hagfeldt, M. Saliba, *Science (80-. )*. **2018**, *362*, 449.
- [68] B. Suarez, V. Gonzalez-Pedro, T. S. Ripolles, R. S. Sanchez, L. Otero, I. Mora-Sero, *J. Phys. Chem. Lett.* **2014**, *5*, 1628.
- [69] A. Miyata, A. Mitioglu, P. Plochocka, O. Portugall, J. T. W. Wang, S. D. Stranks, H. J. Snaith, R. J. Nicholas, *Nat. Phys.* **2015**, *11*, 582.
- [70] T. C. Sum, N. Mathews, *Energy Environ. Sci.* **2014**, *7*, 2518.
- [71] G. Xing, N. Mathews, S. Sun, S. S. Lim, Y. M. Lam, M. Gratzel, S. Mhaisalkar, T. C. Sum, *Science (80-. )*. **2013**, *342*, 344.
- [72] C. R. Kalaiselvi, N. Muthukumarasamy, D. Velauthapillai, M. Kang, T. S. Senthil, *Mater. Lett.* **2018**, *219*, 198.
- [73] M. I. Asghar, J. Zhang, H. Wang, P. D. Lund, *Renew. Sustain. Energy Rev.* **2017**, *77*, 131.
- [74] M. Bouchard, J. Hilhorst, S. Pouget, F. Alam, M. Mendez, D. Djurado, D. Aldakov, T. Schüllli, P. Reiss, *J. Phys. Chem. C* **2017**, *121*, 7596.
- [75] J. Yu, Q. Li, J. Fan, B. Cheng, *Chem. Commun.* **2011**, *47*, 9161.
- [76] K. Lv, J. Yu, J. Fan, M. Jaroniec, *CrystEngComm* **2011**, *13*, 7044.
- [77] J. Fan, L. Zhao, J. Yu, G. Liu, *Nanoscale* **2012**, *4*, 6597.
- [78] X. Zhu, B. Cheng, J. Yu, W. Ho, *Appl. Surf. Sci.* **2016**, *364*, 808.
- [79] J. P. Correa Baena, L. Steier, W. Tress, M. Saliba, S. Neutzner, T. Matsui, F. Giordano, T. J. Jacobsson, A. R. Srimath Kandada, S. M. Zakeeruddin, A.

Petrozza, A. Abate, M. K. Nazeeruddin, M. Grätzel, A. Hagfeldt, *Energy Environ. Sci.* **2015**, *8*, 2928.

- [80] T. Leijtens, G. E. Eperon, S. Pathak, A. Abate, M. M. Lee, H. J. Snaith, *Nat. Commun.* **2013**, *4*, 2885.
- [81] M. J. Carnie, C. Charbonneau, M. L. Davies, J. Troughton, T. M. Watson, K. Wojciechowski, H. Snaith, D. A. Worsley, *Chem. Commun.* **2013**, *49*, 7893.
- [82] D. Liu, T. L. Kelly, *Nat. Photonics* **2014**, *8*, 133.
- [83] J. Yang, B. D. Siempelkamp, E. Mosconi, F. De Angelis, T. L. Kelly, *Chem. Mater.* **2015**, *27*, 4229.
- [84] Q. Dong, Y. Shi, K. Wang, Y. Li, S. Wang, H. Zhang, Y. Xing, Y. Du, X. Bai, T. Ma, *J. Phys. Chem. C* **2015**, *119*, 10212.
- [85] X. Ren, D. Yang, Z. Yang, J. Feng, X. Zhu, J. Niu, Y. Liu, W. Zhao, S. F. Liu, *ACS Appl. Mater. Interfaces* **2017**, *9*, 2421.
- [86] L. Huang, X. Sun, C. Li, J. Xu, R. Xu, Y. Du, J. Ni, H. Cai, J. Li, Z. Hu, J. Zhang, *ACS Appl. Mater. Interfaces* **2017**, *9*, 21909.
- [87] E. J. Yeom, S. S. Shin, W. S. Yang, S. J. Lee, W. Yin, D. Kim, J. H. Noh, T. K. Ahn, S. Il Seok, *J. Mater. Chem. A* **2017**, *5*, 79.
- [88] Q. Jiang, L. Zhang, H. Wang, X. Yang, J. Meng, H. Liu, Z. Yin, J. Wu, X. Zhang, J. You, *Nat. Energy* **2017**, *2*, 16177.
- [89] M. Kim, G.-H. Kim, K. S. Oh, Y. Jo, H. Yoon, K.-H. Kim, H. Lee, J. Y. Kim, D. S. Kim, *ACS Nano* **2017**, *11*, 6057.
- [90] J. Peng, T. Duong, X. Zhou, H. Shen, Y. Wu, H. K. Mulmudi, Y. Wan, D. Zhong, J. Li, T. Tsuzuki, K. J. Weber, K. R. Catchpole, T. P. White, *Adv. Energy Mater.* **2017**, *7*, 1601768.
- [91] W. S. Yang, J. H. Noh, N. J. Jeon, Y. C. Kim, S. Ryu, J. Seo, S. I. Seok, *Science (80-. )*. **2015**, *348*, 1234.
- [92] S. S. Shin, E. J. Yeom, W. S. Yang, S. Hur, M. G. Kim, J. Im, J. Seo, J. H. Noh, S. Il

- Seok, *Science* (80-. ). **2017**, 356, 167.
- [93] T. Duong, Y. Wu, H. Shen, J. Peng, X. Fu, D. Jacobs, E.-C. Wang, T. C. Kho, K. C. Fong, M. Stocks, E. Franklin, A. Blakers, N. Zin, K. McIntosh, W. Li, Y.-B. Cheng, T. P. White, K. Weber, K. Catchpole, *Adv. Energy Mater.* **2017**, 7, 1700228.
- [94] Z. Qiu, S. Yuan, H. Gong, H. Zhang, X. Qiu, T. Luo, B. Cao, *J. Am. Ceram. Soc.* **2017**, 100, 176.
- [95] N. Y. Nia, F. Matteocci, L. Cina, A. Di Carlo, *ChemSusChem* **2017**, 10, 3854.
- [96] E. H. Jung, N. J. Jeon, E. Y. Park, C. S. Moon, T. J. Shin, T.-Y. Yang, J. H. Noh, J. Seo, *Nature* **2019**, 567, 511.
- [97] D. Koushik, W. J. H. Verhees, D. Zhang, Y. Kuang, S. Veenstra, M. Creatore, R. E. I. Schropp, *Adv. Mater. Interfaces* **2017**, 4, 1700043.
- [98] X. Bao, Y. Wang, Q. Zhu, N. Wang, D. Zhu, J. Wang, A. Yang, R. Yang, *J. Power Sources* **2015**, 297, 53.
- [99] H. Choi, J. Jeong, H.-B. Kim, S. Kim, B. Walker, G.-H. Kim, J. Y. Kim, *Nano Energy* **2014**, 7, 80.
- [100] J. You, L. Meng, T.-B. Song, T.-F. Guo, Y. (Michael) Yang, W.-H. Chang, Z. Hong, H. Chen, H. Zhou, Q. Chen, Y. Liu, N. De Marco, Y. Yang, *Nat. Nanotechnol.* **2016**, 11, 75.
- [101] W. Chen, L. Xu, X. Feng, J. Jie, Z. He, *Adv. Mater.* **2017**, 29, 1603923.
- [102] F. Xie, C.-C. Chen, Y. Wu, X. Li, M. Cai, X. Liu, X. Yang, L. Han, *Energy Environ. Sci.* **2017**, 10, 1942.
- [103] M. Kim, G.-H. Kim, T. K. Lee, I. W. Choi, H. W. Choi, Y. Jo, Y. J. Yoon, J. W. Kim, J. Lee, D. Huh, H. Lee, S. K. Kwak, J. Y. Kim, D. S. Kim, *Joule* **2019**, 3, 2179.
- [104] J. Duan, Y. Wang, X. Yang, Q. Tang, *Angew. Chemie Int. Ed.* **2020**, 59, 4391.
- [105] R. Dileep, G. Kesavan, V. Reddy, M. K. Rajbhar, S. Shanmugasundaram, E. Ramasamy, G. Veerappan, *Sol. Energy* **2019**, 187, 261.

- [106] H. Tsai, W. Nie, J.-C. Blancon, C. C. Stoumpos, R. Asadpour, B. Harutyunyan, A. J. Neukirch, R. Verduzco, J. J. Crochet, S. Tretiak, L. Pedesseau, J. Even, M. A. Alam, G. Gupta, J. Lou, P. M. Ajayan, M. J. Bedzyk, M. G. Kanatzidis, A. D. Mohite, *Nature* **2016**, *536*, 312.
- [107] Y. Shao, Y. Yuan, J. Huang, *Nat. Energy* **2016**, *1*, 15001.
- [108] J. Lee, H. Kang, G. Kim, H. Back, J. Kim, S. Hong, B. Park, E. Lee, K. Lee, *Adv. Mater.* **2017**, *29*, 1606363.
- [109] T. Jin, W. Li, Y. Li, Y. Luo, Y. Shen, L. Cheng, J. Tang, *Adv. Opt. Mater.* **2018**, *6*, 1801153.
- [110] L. Kuai, Y. Wang, Z. Zhang, Y. Yang, Y. Qin, T. Wu, Y. Li, Y. Li, T. Song, X. Gao, L. Wang, B. Sun, *Sol. RRL* **2019**, *3*, 1900053.
- [111] L. Wang, G. Wang, Z. Yan, J. Qiu, C. Jia, W. Zhang, C. Zhen, C. Xu, K. Tai, X. Jiang, S. Yang, *Sol. RRL* **2020**, *4*, 2000098.
- [112] J. A. Smith, O. S. Game, J. E. Bishop, E. L. K. Spooner, R. C. Kilbride, C. Greenland, R. Jayaprakash, T. I. Alanazi, E. J. Cassella, A. Tejada, G. Chistiakova, M. Wong-Stringer, T. J. Routledge, A. J. Parnell, D. B. Hammond, D. G. Lidzey, *ACS Appl. Energy Mater.* **2020**, acsaem.0c00525.
- [113] O. S. Game, J. A. Smith, T. I. Alanazi, M. Wong-Stringer, V. Kumar, C. Rodenburg, N. J. Terrill, D. G. Lidzey, *J. Mater. Chem. A* **2020**, *8*, 10943.
- [114] Y. Mo, J. Shi, P. Zhou, S. Li, T. Bu, Y.-B. Cheng, F. Huang, *Sol. RRL* **2019**, *3*, 1900209.
- [115] A. Kojima, K. Teshima, Y. Shirai, T. Miyasaka, *J. Am. Chem. Soc.* **2009**, *131*, 6050.
- [116] J.-H. Im, C.-R. Lee, J.-W. Lee, S.-W. Park, N.-G. Park, *Nanoscale* **2011**, *3*, 4088.
- [117] H.-S. Kim, C.-R. Lee, J.-H. Im, K.-B. Lee, T. Moehl, A. Marchioro, S.-J. Moon, R. Humphry-Baker, J.-H. Yum, J. E. Moser, M. Grätzel, N.-G. Park, *Sci. Rep.* **2012**, *2*, 591.
- [118] M. M. Lee, J. Teuscher, T. Miyasaka, T. N. Murakami, H. J. Snaith, *Science (80- )*.

2012, 338, 643.

- [119] A. B. Djurišić, F. Z. Liu, H. W. Tam, M. K. Wong, A. Ng, C. Surya, W. Chen, Z. B. He, *Prog. Quantum Electron.* **2017**, 53, 1.
- [120] H. M. Upadhyaya, S. Senthilarasu, M.-H. Hsu, D. K. Kumar, *Sol. Energy Mater. Sol. Cells* **2013**, 119, 291.
- [121] J. T.-W. Wang, J. M. Ball, E. M. Barea, A. Abate, J. A. Alexander-Webber, J. Huang, M. Saliba, I. Mora-Sero, J. Bisquert, H. J. Snaith, R. J. Nicholas, *Nano Lett.* **2014**, 14, 724.
- [122] W. S. Yang, J. H. Noh, N. J. Jeon, Y. C. Kim, S. Ryu, J. Seo, S. Il Seok, *Science (80-. )*. **2015**, 348, 1234.
- [123] H. Zhou, Q. Chen, G. Li, S. Luo, T. -b. Song, H.-S. Duan, Z. Hong, J. You, Y. Liu, Y. Yang, *Science (80-. )*. **2014**, 345, 542.
- [124] F. Palazon, D. Pérez-del-Rey, S. Marras, M. Prato, M. Sessolo, H. J. Bolink, L. Manna, *ACS Energy Lett.* **2018**, 3, 835.
- [125] L. Givalou, M. Antoniadou, A. Kaltzoglou, P. Falaras, *Mater. Today Proc.* **2019**, 19, 79.
- [126] A. J. Harding, A. G. Kuba, B. E. McCandless, U. K. Das, K. D. Dobson, B. A. Ogunnaike, W. N. Shafarman, *RSC Adv.* **2020**, 10, 16125.
- [127] R. Belchi, A. Habert, E. Foy, A. Gheno, S. Vedraïne, R. Antony, B. Ratier, J. Bouclé, N. Herlin-Boime, *ACS Omega* **2019**, 4, 11906.
- [128] Y.-N. Zhang, B. Li, L. Fu, L.-W. Yin, *J. Power Sources* **2019**, 419, 27.
- [129] J. W. Lim, H. Wang, C. H. Choi, L. N. Quan, K. Chung, W.-T. Park, Y.-Y. Noh, D. H. Kim, *J. Power Sources* **2019**, 438, 226956.
- [130] J. H. Noh, S. H. Im, J. H. Heo, T. N. Mandal, S. Il Seok, *Nano Lett.* **2013**, 13, 1764.
- [131] D. Huang, P. Xie, Z. Pan, H. Rao, X. Zhong, *J. Mater. Chem. A* **2019**, 7, 22420.
- [132] M. M. Tavakoli, L. Gu, Y. Gao, C. Reckmeier, J. He, A. L. Rogach, Y. Yao, Z. Fan,

*Sci. Rep.* **2015**, *5*, 14083.

- [133] D. Lin, T. Zhang, J. Wang, M. Long, F. Xie, J. Chen, B. Wu, T. Shi, K. Yan, W. Xie, P. Liu, J. Xu, *Nano Energy* **2019**, *59*, 619.
- [134] J. Jang, G. Choe, S. Yim, *ACS Appl. Mater. Interfaces* **2019**, *11*, 20073.
- [135] Y. Wang, H. Xu, F. Wang, D. Liu, H. Chen, H. Zheng, L. Ji, P. Zhang, T. Zhang, Z. D. Chen, J. Wu, L. Chen, S. Li, *Chem. Eng. J.* **2019**, *391*, 123589.
- [136] S. Wang, J. Jin, Y. Qi, P. Liu, Y. Xia, Y. Jiang, R. He, B. Chen, Y. Liu, X. Zhao, *Adv. Funct. Mater.* **2020**, *30*, 1908343.
- [137] Q. Li, Y. Zhao, W. Zhou, Z. Han, R. Fu, F. Lin, D. Yu, Q. Zhao, *Adv. Energy Mater.* **2019**, *9*, 1902239.
- [138] K. Deng, L. Li, *Adv. Mater. Interfaces* **2016**, *3*, 1600505.
- [139] Y. Ko, Y. R. Kim, H. Jang, C. Lee, M. G. Kang, Y. Jun, *Nanoscale Res. Lett.* **2017**, *12*, 498.
- [140] U. A. Charles, M. A. Ibrahim, M. A. M. Teridi, *J. Power Sources* **2018**, *378*, 717.
- [141] Q. Xi, G. Gao, H. Zhou, Y. Zhao, C. Wu, L. Wang, Y. Lei, J. Xu, *Appl. Surf. Sci.* **2019**, *463*, 1107.
- [142] J. Chen, J. Xu, L. Xiao, B. Zhang, S. Dai, J. Yao, *ACS Appl. Mater. Interfaces* **2017**, *9*, 2449.
- [143] F. Ansari, M. Salavati-Niasari, P. Nazari, N. Mir, V. Ahmadi, B. Abdollahi Nejad, *ACS Appl. Energy Mater.* **2018**, *1*, 6018.
- [144] J. Li, X. Liu, J. Xu, J. Chen, C. Zhao, M. Salma Maneno, B. Zhang, J. Yao, *Sol. RRL* **2019**, *3*, 1900218.
- [145] M. Liu, M. B. Johnston, H. J. Snaith, *Nature* **2013**, *501*, 395.
- [146] N. H. Tiep, Z. Ku, H. J. Fan, *Adv. Energy Mater.* **2016**, *6*, 1501420.
- [147] Q. Jiang, Y. Zhao, X. Zhang, X. Yang, Y. Chen, Z. Chu, Q. Ye, X. Li, Z. Yin, J. You, *Nat. Photonics* **2019**, *13*, 460.

- [148] P. Roy, N. Kumar Sinha, S. Tiwari, A. Khare, *Sol. Energy* **2020**, *198*, 665.
- [149] A. Mahapatra, D. Prochowicz, M. M. Tavakoli, S. Trivedi, P. Kumar, P. Yadav, *J. Mater. Chem. A* **2020**, *8*, 27.
- [150] Z. Yang, Z. Yu, H. Wei, X. Xiao, Z. Ni, B. Chen, Y. Deng, S. N. Habisreutinger, X. Chen, K. Wang, J. Zhao, P. N. Rudd, J. J. Berry, M. C. Beard, J. Huang, *Nat. Commun.* **2019**, *10*, 4498.
- [151] S. S. Mali, J. V. Patil, H. Arandiyani, R. Luque, C. K. Hong, *ECS J. Solid State Sci. Technol.* **2019**, *8*, Q111.
- [152] G. Niu, X. Guo, L. Wang, *J. Mater. Chem. A* **2015**, *3*, 8970.
- [153] J. Prakash, A. Singh, G. Sathiyani, R. Ranjan, A. Singh, A. Garg, R. K. Gupta, *Mater. Today Energy* **2018**, *9*, 440.
- [154] Q. Chen, H. Zhou, Y. Fang, A. Z. Stieg, T.-B. Song, H.-H. Wang, X. Xu, Y. Liu, S. Lu, J. You, P. Sun, J. McKay, M. S. Goorsky, Y. Yang, *Nat. Commun.* **2015**, *6*, 7269.
- [155] M. Kim, T. K. Lee, I. W. Choi, H. W. Choi, Y. Jo, J. Lee, G.-H. Kim, S. K. Kwak, D. S. Kim, *Sustain. Energy Fuels* **2020**, DOI 10.1039/D0SE00382D.
- [156] N. Pellet, P. Gao, G. Gregori, T. Y. Yang, M. K. Nazeeruddin, J. Maier, M. Grätzel, *Angew. Chemie - Int. Ed.* **2014**, *53*, 3151.
- [157] F. Hao, C. C. Stoumpos, R. P. H. Chang, M. G. Kanatzidis, *J. Am. Chem. Soc.* **2014**, *136*, 8094.
- [158] Z. Yang, C.-C. Chueh, P.-W. Liang, M. Crump, F. Lin, Z. Zhu, A. K. Y. Jen, *Nano Energy* **2016**, *22*, 328.
- [159] N. J. Jeon, J. H. Noh, W. S. Yang, Y. C. Kim, S. Ryu, J. Seo, S. Il Seok, *Nature* **2015**, *517*, 476.
- [160] M. Zhang, J. S. Yun, Q. Ma, J. Zheng, C. F. J. Lau, X. Deng, J. Kim, D. Kim, J. Seidel, M. A. Green, S. Huang, A. W. Y. Ho-Baillie, *ACS Energy Lett.* **2017**, *2*, 438.
- [161] N. J. Jeon, J. H. Noh, Y. C. Kim, W. S. Yang, S. Ryu, S. Il Seok, *Nat. Mater.* **2014**, *13*, 897.

- [162] L. Ji, T. Zhang, Y. Wang, P. Zhang, D. Liu, Z. Chen, S. Li, *Nanoscale Res. Lett.* **2017**, *12*, 367.
- [163] T. Wu, J. Wu, Y. Tu, X. He, Z. Lan, M. Huang, J. Lin, *J. Power Sources* **2017**, *365*, 1.
- [164] S. Jin, Y. Wei, F. Huang, X. Yang, D. Luo, Y. Fang, Y. Zhao, Q. Guo, Y. Huang, J. Wu, *J. Power Sources* **2018**, *404*, 64.
- [165] L. Yang, Y. Gao, Y. Wu, X. Xue, F. Wang, Y. Sui, Y. Sun, M. Wei, X. Liu, H. Liu, *ACS Appl. Mater. Interfaces* **2019**, *11*, 792.
- [166] B. Gao, J. Meng, J. Lu, R. Zhao, *Mater. Lett.* **2020**, *274*, 127995.
- [167] M. Xiao, F. Huang, W. Huang, Y. Dkhissi, Y. Zhu, J. Etheridge, A. Gray-Weale, U. Bach, Y.-B. Cheng, L. Spiccia, *Angew. Chemie Int. Ed.* **2014**, *53*, 9898.
- [168] D. Prochowicz, M. M. Tavakoli, A. Solanki, T. W. Goh, K. Pandey, T. C. Sum, M. Saliba, P. Yadav, *J. Mater. Chem. A* **2018**, *6*, 14307.
- [169] J. H. Kim, P. W. Liang, S. T. Williams, N. Cho, C. C. Chueh, M. S. Glaz, D. S. Ginger, A. K. Y. Jen, *Adv. Mater.* **2015**, *27*, 695.
- [170] D. Liu, Y. Wang, H. Zheng, J. Wu, L. Ji, P. Zhang, W. Ahmad, H. Chen, Z. Chen, S. Li, *Electrochim. Acta* **2019**, *296*, 508.
- [171] N. Chander, A. F. Khan, P. S. Chandrasekhar, E. Thouti, S. K. Swami, V. Dutta, V. K. Komarala, *Appl. Phys. Lett.* **2014**, *105*, 033904.
- [172] M. Wong-Stringer, O. S. Game, J. A. Smith, T. J. Routledge, B. A. Alqurashy, B. G. Freestone, A. J. Parnell, N. Vaenas, V. Kumar, M. O. A. Alawad, A. Iraqi, C. Rodenburg, D. G. Lidzey, *Adv. Energy Mater.* **2018**, *1801234*, 1.
- [173] T. Matsui, T. Yamamoto, T. Nishihara, R. Morisawa, T. Yokoyama, T. Sekiguchi, T. Negami, *Adv. Mater.* **2019**, *31*, 1806823.
- [174] D. Bi, X. Li, J. V. Milić, D. J. Kubicki, N. Pellet, J. Luo, T. LaGrange, P. Mettraux, L. Emsley, S. M. Zakeeruddin, M. Grätzel, *Nat. Commun.* **2018**, *9*, 4482.
- [175] J. A. Christians, P. Schulz, J. S. Tinkham, T. H. Schloemer, S. P. Harvey, B. J.

- Tremolet de Villers, A. Sellinger, J. J. Berry, J. M. Luther, *Nat. Energy* **2018**, *3*, 68.
- [176] X. Li, S. Fu, S. Liu, Y. Wu, W. Zhang, W. Song, J. Fang, *Nano Energy* **2019**, *64*, 103962.
- [177] X. Yang, J. Xi, Y. Sun, Y. Zhang, G. Zhou, W.-Y. Wong, *Nano Energy* **2019**, *64*, 103946.
- [178] A. Ghosh, D. K. Chaudhary, A. Mandal, S. Prodhan, K. K. Chauhan, S. Vihari, G. Gupta, P. K. Datta, S. Bhattacharyya, *J. Phys. Chem. Lett.* **2020**, *11*, 591.
- [179] N. Drigo, C. Roldan-Carmona, M. Franckevičius, K.-H. Lin, R. Gegevičius, H. Kim, P. A. Schouwink, A. A. Sutanto, S. Olthof, M. Sohail, K. Meerholz, V. Gulbinas, C. Corminboeuf, S. Paek, M. K. Nazeeruddin, *J. Am. Chem. Soc.* **2020**, *142*, 1792.
- [180] T. Yang, N. J. Jeon, H. Shin, S. S. Shin, Y. Y. Kim, J. Seo, *Adv. Sci.* **2019**, *6*, 1900528.
- [181] S. Akin, *ACS Appl. Mater. Interfaces* **2019**, *11*, 39998.
- [182] X. Li, J. Yang, Q. Jiang, H. Lai, S. Li, Y. Tan, Y. Chen, S. Li, *J. Mater. Chem. A* **2019**, *7*, 7065.
- [183] R. Prasanna, T. Leijtens, S. P. Dunfield, J. A. Raiford, E. J. Wolf, S. A. Swifter, J. Werner, G. E. Eperon, C. de Paula, A. F. Palmstrom, C. C. Boyd, M. F. A. M. van Hest, S. F. Bent, G. Teeter, J. J. Berry, M. D. McGehee, *Nat. Energy* **2019**, *4*, 939.
- [184] S. Bai, P. Da, C. Li, Z. Wang, Z. Yuan, F. Fu, M. Kawecki, X. Liu, N. Sakai, J. T.-W. Wang, S. Huettner, S. Buecheler, M. Fahlman, F. Gao, H. J. Snaith, *Nature* **2019**, *571*, 245.
- [185] N. Arora, M. I. Dar, S. Akin, R. Uchida, T. Baumeler, Y. Liu, S. M. Zakeeruddin, M. Grätzel, *Small* **2019**, *15*, 1904746.
- [186] S. Akin, *Sol. Energy* **2020**, *199*, 136.
- [187] A. Krishna, M. A. Akhavan Kazemi, M. Sliwa, G. N. M. Reddy, L. Delevoye, O. Lafon, A. Felten, M. T. Do, S. Gottis, F. Sauvage, *Adv. Funct. Mater.* **2020**, *30*, 1909737.

- [188] H. Zhu, Y. Liu, F. T. Eickemeyer, L. Pan, D. Ren, M. A. Ruiz-Preciado, B. Carlsen, B. Yang, X. Dong, Z. Wang, H. Liu, S. Wang, S. M. Zakeeruddin, A. Hagfeldt, M. I. Dar, X. Li, M. Grätzel, *Adv. Mater.* **2020**, *32*, 1907757.
- [189] S. Ma, Y. Bai, H. Wang, H. Zai, J. Wu, L. Li, S. Xiang, N. Liu, L. Liu, C. Zhu, G. Liu, X. Niu, H. Chen, H. Zhou, Y. Li, Q. Chen, *Adv. Energy Mater.* **2020**, *10*, 1902472.
- [190] Y. Lv, H. Zhang, R. Liu, Y. Sun, W. Huang, *ACS Appl. Mater. Interfaces* **2020**, *12*, 27277.
- [191] W.-Q. Wu, P. N. Rudd, Z. Ni, C. H. Van Brackle, H. Wei, Q. Wang, B. R. Ecker, Y. Gao, J. Huang, *J. Am. Chem. Soc.* **2020**, *142*, 3989.
- [192] H. Back, G. Kim, H. Kim, C.-Y. Nam, J. Kim, Y. R. Kim, T. Kim, B. Park, J. R. Durrant, K. Lee, *Energy Environ. Sci.* **2020**, *13*, 840.
- [193] H. R. Mohseni, M. Dehghanipour, N. Dehghan, F. Tamaddon, M. Ahmadi, M. Sabet, A. Behjat, *Sol. Energy* **2021**, *213*, 59.
- [194] G. Li, J. Wu, J. Song, C. Meng, Z. Song, X. Wang, X. Liu, Y. Yang, D. Wang, Z. Lan, *J. Power Sources* **2021**, *481*, 228857.
- [195] E. Akman, S. Akin, *Adv. Mater.* **2021**, *33*, 2006087.
- [196] H. Bi, X. Zuo, B. Liu, D. He, L. Bai, W. Wang, X. Li, Z. Xiao, K. Sun, Q. Song, Z. Zang, J. Chen, *J. Mater. Chem. A* **2021**, *9*, 3940.
- [197] X. Chen, W. Xu, Z. Shi, G. Pan, J. Zhu, J. Hu, X. Li, C. Shan, H. Song, *Nano Energy* **2021**, *80*, 105564.
- [198] H. Zhu, Y. Ren, L. Pan, O. Ouellette, F. T. Eickemeyer, Y. Wu, X. Li, S. Wang, H. Liu, X. Dong, S. M. Zakeeruddin, Y. Liu, A. Hagfeldt, M. Grätzel, *J. Am. Chem. Soc.* **2021**, *143*, 3231.
- [199] Y.-W. Jang, S. Lee, K. M. Yeom, K. Jeong, K. Choi, M. Choi, J. H. Noh, *Nat. Energy* **2021**, *6*, 63.
- [200] E. H. Anaraki, A. Kermanpur, L. Steier, K. Domanski, T. Matsui, W. Tress, M. Saliba, A. Abate, M. Grätzel, A. Hagfeldt, J.-P. Correa-Baena, *Energy Environ. Sci.*

2016, 9, 3128.

- [201] Z. Wang, D. P. McMeekin, N. Sakai, S. van Reenen, K. Wojciechowski, J. B. Patel, M. B. Johnston, H. J. Snaith, *Adv. Mater.* **2017**, *29*, 1604186.
- [202] Y. Zhang, Z. Fei, P. Gao, Y. Lee, F. F. Tirani, R. Scopelliti, Y. Feng, P. J. Dyson, M. K. Nazeeruddin, *Adv. Mater.* **2017**, *29*, 1702157.
- [203] K. A. Bush, A. F. Palmstrom, Z. J. Yu, M. Boccard, R. Cheacharoen, J. P. Mailoa, D. P. McMeekin, R. L. Z. Hoyer, C. D. Bailie, T. Leijtens, I. M. Peters, M. C. Minichetti, N. Rolston, R. Prasanna, S. Sofia, D. Harwood, W. Ma, F. Moghadam, H. J. Snaith, T. Buonassisi, Z. C. Holman, S. F. Bent, M. D. McGehee, *Nat. Energy* **2017**, *2*, 17009.
- [204] W. Chen, Y. Wu, Y. Yue, J. Liu, W. Zhang, X. Yang, H. Chen, E. Bi, I. Ashraful, M. Gratzel, L. Han, *Science (80-. )*. **2015**, *350*, 944.
- [205] G. Niu, W. Li, F. Meng, L. Wang, H. Dong, Y. Qiu, *J. Mater. Chem. A* **2014**, *2*, 705.
- [206] M. Abdi-Jalebi, Z. Andaji-Garmaroudi, S. Cacovich, C. Stavrakas, B. Philippe, J. M. Richter, M. Alsari, E. P. Booker, E. M. Hutter, A. J. Pearson, S. Lilliu, T. J. Savenije, H. Rensmo, G. Divitini, C. Ducati, R. H. Friend, S. D. Stranks, *Nature* **2018**, *555*, 497.
- [207] W. Liao, D. Zhao, Y. Yu, C. R. Grice, C. Wang, A. J. Cimaroli, P. Schulz, W. Meng, K. Zhu, R.-G. Xiong, Y. Yan, *Adv. Mater.* **2016**, *28*, 9333.
- [208] S. J. Lee, S. S. Shin, Y. C. Kim, D. Kim, T. K. Ahn, J. H. Noh, J. Seo, S. Il Seok, *J. Am. Chem. Soc.* **2016**, *138*, 3974.
- [209] L. Ma, F. Hao, C. C. Stoumpos, B. T. Phelan, M. R. Wasielewski, M. G. Kanatzidis, *J. Am. Chem. Soc.* **2016**, *138*, 14750.
- [210] Q. Tai, X. Guo, G. Tang, P. You, T.-W. Ng, D. Shen, J. Cao, C.-K. Liu, N. Wang, Y. Zhu, C.-S. Lee, F. Yan, *Angew. Chemie Int. Ed.* **2019**, *58*, 806.
- [211] J. S. Yun, J. Seidel, J. Kim, A. M. Soufiani, S. Huang, J. Lau, N. J. Jeon, S. Il Seok, M. A. Green, A. Ho-Baillie, *Adv. Energy Mater.* **2016**, *6*, 1600330.

- [212] N. K. Elumalai, A. Uddin, *Sol. Energy Mater. Sol. Cells* **2016**, *157*, 476.
- [213] Y. Zhao, J. Wei, H. Li, Y. Yan, W. Zhou, D. Yu, Q. Zhao, *Nat. Commun.* **2016**, *7*, 10228.
- [214] L. Gao, S. Huang, L. Chen, X. Li, B. Ding, S. Huang, G. Yang, *Sol. RRL* **2018**, *2*, 1800088.
- [215] L. Zuo, H. Guo, D. W. DeQuilettes, S. Jariwala, N. De Marco, S. Dong, R. DeBlock, D. S. Ginger, B. Dunn, M. Wang, Y. Yang, *Sci. Adv.* **2017**, *3*, e1700106.
- [216] J. Jiang, Q. Wang, Z. Jin, X. Zhang, J. Lei, H. Bin, Z.-G. Zhang, Y. Li, S. F. Liu, *Adv. Energy Mater.* **2018**, *8*, 1701757.
- [217] Y. Zong, Y. Zhou, Y. Zhang, Z. Li, L. Zhang, M.-G. Ju, M. Chen, S. Pang, X. C. Zeng, N. P. Padture, *Chem* **2018**, *4*, 1404.
- [218] X. Li, W. Zhang, Y.-C. Wang, W. Zhang, H.-Q. Wang, J. Fang, *Nat. Commun.* **2018**, *9*, 3806.
- [219] D. Yang, W. Ming, H. Shi, L. Zhang, M.-H. Du, *Chem. Mater.* **2016**, *28*, 4349.
- [220] D. Wei, F. Ma, R. Wang, S. Dou, P. Cui, H. Huang, J. Ji, E. Jia, X. Jia, S. Sajid, A. M. Elseman, L. Chu, Y. Li, B. Jiang, J. Qiao, Y. Yuan, M. Li, *Adv. Mater.* **2018**, *30*, 1707583.
- [221] G. Divitini, S. Cacovich, F. Matteocci, L. Cinà, A. Di Carlo, C. Ducati, *Nat. Energy* **2016**, *1*, 15012.
- [222] A. Dualeh, P. Gao, S. Il Seok, M. K. Nazeeruddin, M. Grätzel, *Chem. Mater.* **2014**, *26*, 6160.
- [223] R. K. Misra, S. Aharon, B. Li, D. Mogilyansky, I. Visoly-Fisher, L. Etgar, E. A. Katz, *J. Phys. Chem. Lett.* **2015**, *6*, 326.
- [224] M. Mozaffari, A. Behjat, B. F. Mirjalili, *Sol. Energy* **2018**, *174*, 780.
- [225] S. Kim, S. Bae, S.-W. Lee, K. Cho, K. D. Lee, H. Kim, S. Park, G. Kwon, S.-W. Ahn, H.-M. Lee, Y. Kang, H.-S. Lee, D. Kim, *Sci. Rep.* **2017**, *7*, 1200.

- [226] J. A. Christians, P. A. Miranda Herrera, P. V. Kamat, *J. Am. Chem. Soc.* **2015**, *137*, 1530.
- [227] B. Philippe, B. W. Park, R. Lindblad, J. Oscarsson, S. Ahmadi, E. M. J. Johansson, H. Rensmo, *Chem. Mater.* **2015**, *27*, 1720.
- [228] A. M. A. Leguy, Y. Hu, M. Campoy-Quiles, M. I. Alonso, O. J. Weber, P. Azarhoosh, M. van Schilfgaarde, M. T. Weller, T. Bein, J. Nelson, P. Docampo, P. R. F. Barnes, *Chem. Mater.* **2015**, *27*, 3397.
- [229] X. Dong, X. Fang, M. Lv, B. Lin, S. Zhang, J. Ding, N. Yuan, *J. Mater. Chem. A* **2015**, *3*, 5360.
- [230] J. Yang, B. D. Siempelkamp, D. Liu, T. L. Kelly, *ACS Nano* **2015**, *9*, 1955.
- [231] U. Krishnan, *J. Photonics Energy* **2019**, *9*, 1.
- [232] S. Guarnera, A. Abate, W. Zhang, J. M. Foster, G. Richardson, A. Petrozza, H. J. Snaith, *J. Phys. Chem. Lett.* **2015**, *6*, 432.
- [233] K. K. Bass, R. E. McAnally, S. Zhou, P. I. Djurovich, M. E. Thompson, B. C. Melot, *Chem. Commun.* **2014**, *50*, 15819.
- [234] H. Zheng, G. Liu, L. Zhu, J. Ye, X. Zhang, A. Alsaedi, T. Hayat, X. Pan, S. Dai, *ACS Appl. Mater. Interfaces* **2017**, *9*, 41006.
- [235] S. Sidhik, C. Rosiles Pérez, M. A. Serrano Estrada, T. López-Luke, A. Torres, E. De la Rosa, *Sol. Energy* **2020**, *202*, 438.
- [236] B. Roose, J.-P. C. Baena, K. C. Gödel, M. Graetzel, A. Hagfeldt, U. Steiner, A. Abate, *Nano Energy* **2016**, *30*, 517.
- [237] X. Li, M. Tschumi, H. Han, S. S. Babkair, R. A. Alzubaydi, A. A. Ansari, S. S. Habib, M. K. Nazeeruddin, S. M. Zakeeruddin, M. Grätzel, *Energy Technol.* **2015**, *3*, 551.
- [238] Y. Yu, C. Wang, C. R. Grice, N. Shrestha, J. Chen, D. Zhao, W. Liao, A. J. Cimaroli, P. J. Roland, R. J. Ellingson, Y. Yan, *ChemSusChem* **2016**, *9*, 3288.
- [239] F. Bella, G. Griffini, J.-P. Correa-Baena, G. Saracco, M. Gratzel, A. Hagfeldt, S.

Turri, C. Gerbaldi, *Science (80-. )*. **2016**, 354, 203.

- [240] N. Tripathi, M. Yanagida, Y. Shirai, T. Masuda, L. Han, K. Miyano, *J. Mater. Chem. A* **2015**, 3, 12081.
- [241] W. Tress, N. Marinova, T. Moehl, S. M. Zakeeruddin, M. K. Nazeeruddin, M. Grätzel, *Energy Environ. Sci.* **2015**, 8, 995.
- [242] Y. Shao, Y. Fang, T. Li, Q. Wang, Q. Dong, Y. Deng, Y. Yuan, H. Wei, M. Wang, A. Gruverman, J. Shield, J. Huang, *Energy Environ. Sci.* **2016**, 9, 1752.
- [243] J. Haruyama, K. Sodeyama, L. Han, Y. Tateyama, *J. Am. Chem. Soc.* **2015**, 137, 10048.
- [244] Y. Kato, L. K. Ono, M. V. Lee, S. Wang, S. R. Raga, Y. Qi, *Adv. Mater. Interfaces* **2015**, 2, 1500195.
- [245] P. Delugas, C. Caddeo, A. Filippetti, A. Mattoni, *J. Phys. Chem. Lett.* **2016**, 7, 2356.
- [246] L. Liu, S. Huang, Y. Lu, P. Liu, Y. Zhao, C. Shi, S. Zhang, J. Wu, H. Zhong, M. Sui, H. Zhou, H. Jin, Y. Li, Q. Chen, *Adv. Mater.* **2018**, 30, 1800544.
- [247] Z. Li, C. Xiao, Y. Yang, S. P. Harvey, D. H. Kim, J. A. Christians, M. Yang, P. Schulz, S. U. Nanayakkara, C.-S. Jiang, J. M. Luther, J. J. Berry, M. C. Beard, M. M. Al-Jassim, K. Zhu, *Energy Environ. Sci.* **2017**, 10, 1234.
- [248] K. Domanski, B. Roose, T. Matsui, M. Saliba, S.-H. Turren-Cruz, J.-P. Correa-Baena, C. R. Carmona, G. Richardson, J. M. Foster, F. De Angelis, J. M. Ball, A. Petrozza, N. Mine, M. K. Nazeeruddin, W. Tress, M. Grätzel, U. Steiner, A. Hagfeldt, A. Abate, *Energy Environ. Sci.* **2017**, 10, 604.
- [249] M. Bag, L. A. Renna, R. Y. Adhikari, S. Karak, F. Liu, P. M. Lahti, T. P. Russell, M. T. Tuominen, D. Venkataraman, *J. Am. Chem. Soc.* **2015**, 137, 13130.
- [250] J. Carrillo, A. Guerrero, S. Rahimnejad, O. Almora, I. Zarazua, E. Mas-Marza, J. Bisquert, G. Garcia-Belmonte, *Adv. Energy Mater.* **2016**, 6, 1502246.
- [251] M. T. Neukom, S. Züfle, E. Knapp, M. Makha, R. Hany, B. Ruhstaller, *Sol. Energy*

*Mater. Sol. Cells* **2017**, *169*, 159.

[252] Q. Wu, C. Xue, Y. Li, P. Zhou, W. Liu, J. Zhu, S. Dai, C. Zhu, S. Yang, *ACS Appl. Mater. Interfaces* **2015**, *7*, 28466.

[253] Y. Hishikawa, H. Shimura, T. Ueda, A. Sasaki, Y. Ishii, *Curr. Appl. Phys.* **2016**, *16*, 898.

[254] H.-S. Kim, I.-H. Jang, N. Ahn, M. Choi, A. Guerrero, J. Bisquert, N.-G. Park, *J. Phys. Chem. Lett.* **2015**, *6*, 4633.

# Chapter 3

---

---

## Experimental Methods

### 3.0: Introduction

The methodology used to characterise charge transporting layers and perovskite materials is described in this chapter. Additional information regarding the fabrication and processing of charge transporting layers and perovskite materials of chapter 5 will be described separately. The main aim of this research is to understand and enhance the performance of device metrics as well as achieve greater stability of perovskite solar cells through the use of numerous characterisation methodologies. An analysis of these techniques is found in this chapter.

### 3.1: Deposition Techniques

The fabrication of the perovskite solar cells used several different techniques to deposit individual layers. These techniques are explained in the following sections.

#### 3.1.1: Spin-coating

Spin coating technique is a widely used approach to fabricate thin-film semiconductor devices.<sup>[1]</sup> In order to create a uniform thin perovskite film, a substrate (for example glass slide) is placed on a spin-coater. A solution of the organic-inorganic perovskite precursor is prepared and then applied to the surface.<sup>[2]</sup> The spin coating process occurs in a number of steps as follows: (1) fluid spreading, (2) stabilising the outflow of the fluid and (3) film drying by

evaporation.<sup>[3]</sup> There are several parameters that have to be considered in this process including viscosity and concentration of the solution to be coated, spin-speed, spin-time and volume of solution dispensed.<sup>[4]</sup> The spin-coating process is shown in Figure 1.

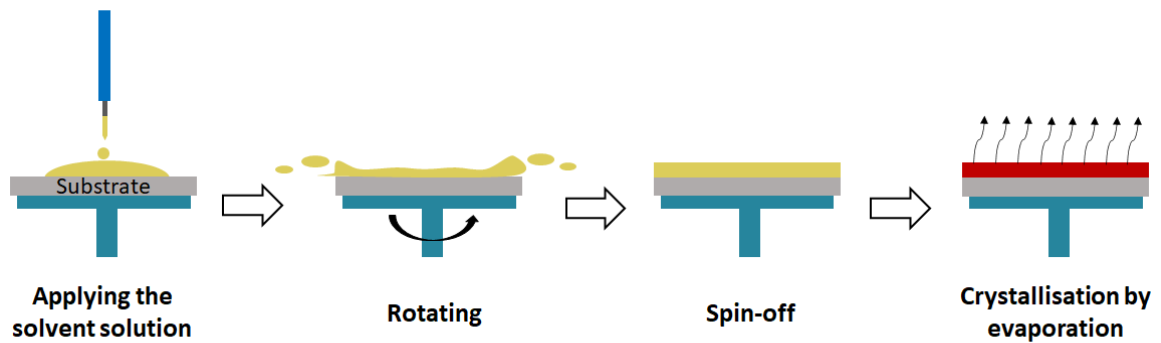


**Figure 1:** Representation of the thin film spin-coating process.

Here, film thickness can be readily controlled by control the angular velocity of the substrate  $\omega$  (rpm)<sup>[5]</sup> as defined by equation 1<sup>[6]</sup> where  $t$  is resultant film thickness.

$$t \propto \frac{1}{\sqrt{\omega}} \quad (\text{Eq.1})$$

Typically during spin coating, the substrate is kept spinning until the resultant film completely dries. There are several other factors that affect film thickness, these include the boiling point and vapour pressure of solvent that is used, in addition to environmental factors such as temperature and humidity. By using solvents possessing high boiling point and/or lower vapour pressure the drying process can be extended significantly. In order to hasten the drying process, additives or thermal annealing can be used. Drying of the film can also be promoted by heating the substrate prior to spin coating.<sup>[6]</sup>

### **3.1.2: Spray-coating**

The process of spray-coating is gaining interest as a method to fabricate photovoltaic devices.<sup>[7,8]</sup> This technique develops a fine aerosol through the passage of the solution of interest through a nozzle. This aerosol generated is directed to the surface, which requires either a carrier gas or electrostatic field.<sup>[5]</sup> The small droplets of solution that are transferred onto the substrate dry after impact with the surface.<sup>[9]</sup>

There are numerous factors that can be controlled to modify the spray coating process, and these factors have been studied widely. These factors include the rate of flow, distance present between the spray-head and the substrate, flow pressure, the concentration of the solution, spray duration, substrate temperature, frequency of application and the composition of the co-solvent mixture.<sup>[10]</sup> It has been shown that there is a significant dependence of the morphology of the particles on the distance present between the spray-head and the substrate. Additionally, the morphology and thickness of the film change due to solvent choice. To achieve a uniform pin-hole free film, a quick-drying solvent is usually used as it eliminates droplets from undergoing redissolution into the sublayers. Nevertheless, it is also essential that droplets should not dry too rapidly. To obtain a pin-hole free thin film, the amount of liquid should exceed a minimum threshold, which permits the droplets to coalesce and form a continuous wet layer.<sup>[10]</sup>

### **3.1.3: Thermal Evaporation**

Thermal evaporation is a technique used to prepare high quality thin films, typically composed of metals or low molecular mass organic molecules. This technique is usually performed in a vacuum chamber at a pressure less than  $1 \times 10^{-6}$  Pa. The

source material is heated using a crucible, with the evaporated atoms then condensing on the substrate of interest. A schematic of a thermal evaporation system is shown in Figure 2(a). Thermal evaporation chambers often contain multiple deposition sources. Here, the temperature of each source can be regulated independently. Such systems often include several shutters to protect the substrate from unnecessary deposition of molecules.<sup>[11]</sup>

The process of evaporation is shown in the image shown in Figure 2(b). A uniform and compact film can be obtained using this process if it is conducted under optimised conditions.

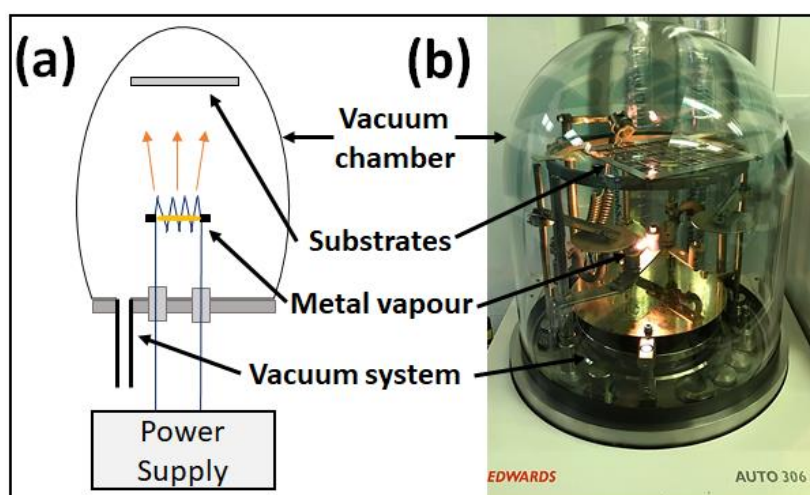


**Figure 2:** (a) Schematic diagram of the thermal evaporation coating instrument (b) Thermal evaporation system during deposition.

### 3.2: Materials

The materials and solvents used in this work are as follows: dry components: methylammonium iodide (MAI, 99.9%), formamidinium iodide (FAI, 98%), methylammonium bromide (MABr, 99.5%) and spiro-OMeTAD (sublimed 99.5%). All these materials were bought from Ossila Ltd. Lead (II) bromide  $\text{PbBr}_2$ , lead (II) iodide ( $\text{PbI}_2$ , 99.99%) were purchased from Tokyo Chemical Industry UK Ltd.

Tin(IV) oxide (SnO<sub>2</sub>) 15 wt% in H<sub>2</sub>O colloidal dispersion liquid was purchased from Alfa Aesar 44592.36. Gold wire was purchased from Cookson Gold Ltd. Hellmanex III purchased from Hellma UK Ltd. The following materials and solvents were purchased from Sigma Aldrich: titanium diisopropoxide bis(acetylacetonate) (75 wt% in isopropanol), titania paste (TiO<sub>2</sub>), cesium iodide (CsI, 99.99%), potassium iodide (KI, 99%), a poly[bis(4-phenyl)(2,4,6-trimethylphenyl)amine] (PTAA), 4-tert-butylpyridine (tBP, 98%), bis(trifluoromethane)sulfonimide lithium salt (Li TFSI, 99%), tris(2-(1*H*-pyrazol-1-yl)-4-*tert*-butylpyridine)cobalt(III)tri[hexafluoro phosphate] (FK209), Zink powder (Zn), isopropanol (IPA), n-butanol (99.8%, anhydrous), hydrochloric acid (HCl), chlorobenzene (CB, 99.8%, anhydrous), N,N-dimethylformamide (DMF, 99.8%, anhydrous), dimethyl sulfoxide (DMSO, 99.9%, anhydrous), toluene (99.8%, anhydrous) and acetonitrile (ACN, 99.8%, anhydrous). The chemical structures of materials used in perovskite solar cells are shown in Figure 3.

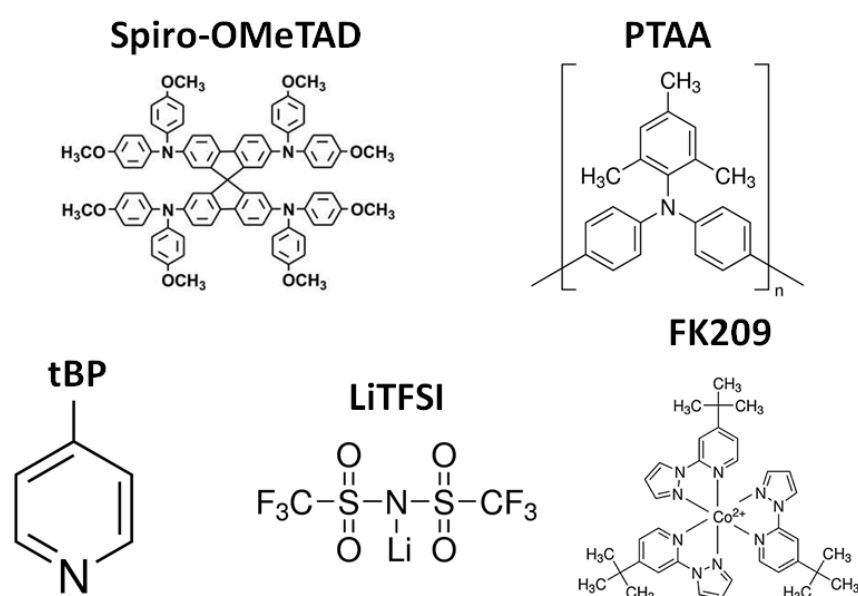


**Figure 3:** Chemical structures of organic materials used in thesis.

### 3.3: Device Fabrication

This section provides an overview of the perovskite solar cell fabrication process as shown schematically in Figure 4. The general process of device fabrication is described below. The architecture of the devices used in this research was typically a normal planar solar cell (n-i-p). Devices were fabricated on glass substrates measuring 20 mm x 15 mm having either an ITO or FTO coating.

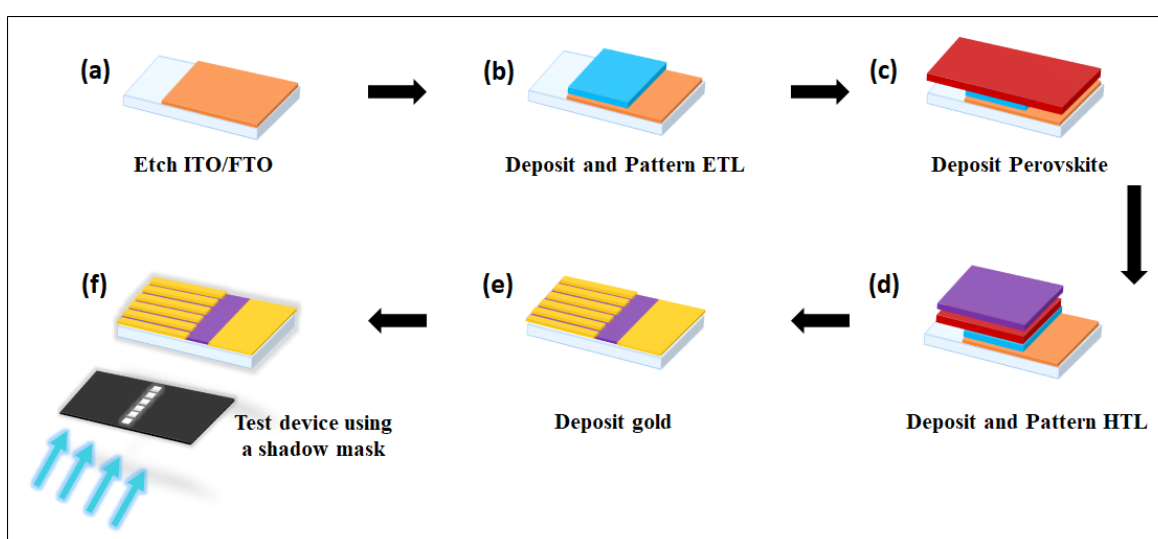


**Figure 4:** Summary of the fabrication process and testing procedure of solar cells.

#### 3.3.1: Etching and Cleaning Procedure

The initial step of device fabrication process is the etching of ITO/FTO, allowing separated anode and cathode contacts to be created. To do this, approximately two-thirds of the substrate was masked using Kapton tape, after which zinc powder was sprinkled over the exposed surface along with 4 mol of HCl. This reduced the surface of the transparent conductive oxide (TCO), permitting the extraction of  $H_3O$  ions. These generate hydrogen ions which penetrate the tin oxide and disrupt the bonds between tin and oxygen. The whole process required a couple of seconds, with the remaining residue being cleared using a cotton bud. To clean the substrates, they

were placed in a solution of 2% aqueous Hellmanex mixed with deionised (DI) water. The solution was subjected to 15 minutes of sonication. Samples were then placed in a Pyrex dish filled with IPA. They were then subject to a further 15 minutes of sonification. The substrates were finally dried using a nitrogen gun ( $N_2$ ) and then subjected to 15 minutes of cleaning by ultraviolet-ozone (UV) treatment.<sup>[12-14]</sup>

### **3.3.2: Electron Transport Layer**

$SnO_2$  and  $TiO_2$  were used as the electron transport layer (ETL). To prepare a  $SnO_2$  film, it was first diluted with DI water (6.5:1). Once formed, this solution was deposited onto ITO by spin-coated at 3000 rpm for 30 seconds, and then annealed for 30 minutes at 150 °C.

$TiO_2$  was used in compact and mesoporous forms. Compact  $TiO_2$  (c- $TiO_2$ ) layer was prepared by first dissolving titanium diisopropoxide bis(acetylacetonate) (75 wt% in isopropanol) with n-butanol (1:9). This was sprayed onto the FTO substrate held at 450 °C by a hand held spray gun with a nitrogen pressure at 30 psi. These substrates were coated every 30 seconds until the required thickness was reached. Films were then annealed for 30 minutes and then allowed to cool down overnight at room temperature. Following this, mesoporous  $TiO_2$  (mp- $TiO_2$ ) was deposited on-top of the c- $TiO_2$  by spin-coating  $TiO_2$  paste dissolved in n-butanol (1:6) at 5000 rpm for 30 seconds. Films were then annealed at 450 °C for 45 minutes. Both ETLs were spin coated under ambient conditions.

### **3.3.3: Perovskite**

$MAPbI_3$  precursor ink was prepared using  $PbI_2$  (1.25M) with a ratio of 1:1 MAI in DMSO. This solution was spin-coated using a two-step process (1000 rpm for 10

seconds, followed by 4500 rpm for 30 seconds). During this process, 100  $\mu\text{L}$  of chlorobenzene antisolvent was dropped onto the films after 10 seconds into the second step. Finally, the films were annealed at 100  $^{\circ}\text{C}$  for 60 minutes.

Triple-cation perovskite ( $\text{Cs}_{0.05}\text{FA}_{0.79}\text{MA}_{0.15}\text{PbI}_{2.45}\text{Br}_{0.55}$ ) precursor ink was prepared by using MABr (0.2M), FAI (1M),  $\text{PbBr}_2$  (0.2M) and  $\text{PbI}_2$  (1.1M). The precursor ink was dissolved in anhydrous DMF/DMSO (4:1 volume ratio) to which an additional 42  $\mu\text{L}$  (per ml of ink) of CsI (1.5M) dissolved in DMSO was added. This precursor was spin-coated using a two-step process (1000 rpm for 10 seconds, followed by 6000 rpm for 20 seconds) with 100  $\mu\text{L}$  of chlorobenzene antisolvent dropped onto the films after 15 seconds into the second step. Finally, films were annealed at 100  $^{\circ}\text{C}$  for 60 minutes. The deposition of perovskite layer was carried out in a nitrogen atmosphere.

### **3.3.4: Hole Transport Layer**

Spiro-OMeTAD and PTAA were used as the hole transport layer (HTL). The spiro-OMeTAD HTL was prepared from a solution containing 86  $\text{mg mL}^{-1}$  spiro-OMeTAD in chlorobenzene, doped with 34  $\mu\text{L}$  of tBP, 20  $\mu\text{L}$  of LiTFSI in acetonitrile solution (500  $\text{mg mL}^{-1}$ ) and 11  $\mu\text{L}$  of FK209 in acetonitrile solution (300  $\text{mg mL}^{-1}$ ). The solution was mixed and filtered using a 0.2  $\mu\text{m}$  PTFE filter. This solution was spin-coated on top of perovskite layer at 4000 rpm for 30 seconds before being left to dry in air overnight to allow it to oxidize.

PTAA was prepared from a solution containing 10  $\text{mg mL}^{-1}$  PTAA in toluene. After leaving the solution to stir at 1500 rpm overnight, the solution was placed on a hotplate at 70  $^{\circ}\text{C}$  for 3 minutes until it was fully dissolved as shown in Figure 5. The

PTAA solution was then doped with 4 $\mu$ l of tBP and 7.5  $\mu$ l of LiTFSI. This was mixed and spin-coated at 3000 rpm for 30 seconds.

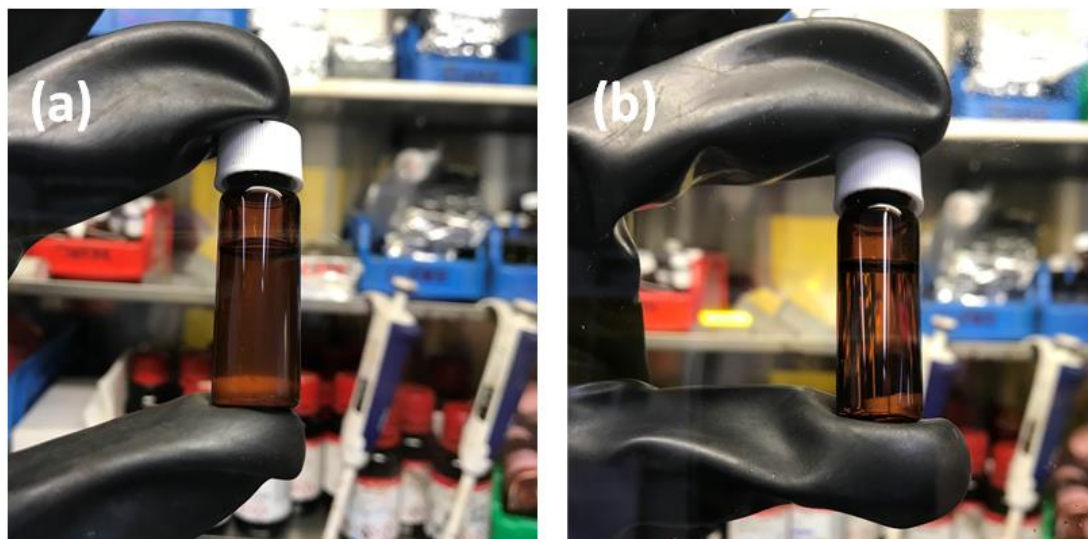


*Figure 5: PTAA solution (a) before (b) after 3 minutes placed on hotplate at 70 °C.*

### **3.3.5: Gold Cathode**

A gold layer having a thickness of 80 and 100 nm was thermally evaporated via a mask which completed the device.

## **3.4: Device Characterisation**

### **3.4.1: Current-Voltage Measurement**

To analyse device performance metrics (described in Chapter 2), they were exposed to light from a Newport 92251A-1000 solar simulator (AM1.5G). Firstly however, an NREL certified silicon reference cell was used to calibrate the integrated light-output from the simulator to  $100 \text{ mWcm}^{-2}$  at  $25 \text{ }^\circ\text{C}$ . Each solar cell was then covered by an aperture mask having an area of either  $0.026 \text{ cm}^2$  or  $0.1558 \text{ cm}^2$ . This was done to accurately define the exposed area on each device and also to prevent stray light from being absorbed. To measure  $J$ - $V$  characteristics, a Keithley 237 source measure unit was used to sweep voltage over the range of 0 to 1.2V at a rate of  $0.1 \text{ Vs}^{-1}$ . The stabilised power output was also recorded by holding the device at its  $V_{\text{MPP}}$ , with the  $V_{\text{MPP}}$  of each device being extracted from the  $J$ - $V$  scans.

### **3.4.2: Lifetime Testing**

Lifetime ageing tests of PV devices were made using an Atlas Suntest CPS+ fixed with a 1500 W Xenon bulb, quartz IR reducing filters and internal reflectors. The spectrum of the lamp was evaluated and was found to be consistent with AM1.5G as shown in Figure 6(a) [Measurement by E. Bovill, EPMM group]. The system generated an irradiance of  $100\text{mWcm}^{-2}$  using a Xenon lamp and a series of internal reflectors. The lamp had to be replaced several times over the longest lifetime testing experiments. Measurements of device performance were made using a reverse sweep  $J$ - $V$  measurement. The bias applied in these tests was swept from 1.2 V to 0 V at a scan rate of  $0.012 \text{ Vs}^{-1}$  using a Keithley 2400 source measure unit as shown in Figure 6(b). It was found that the stability of devices was reduced when they were swept into negative bias, and so this test was avoided. Devices were held

at open circuit between measurements, with every device scanned every 4 minutes. During the experiment, the local temperature was held at  $(42 \pm 3) ^\circ\text{C}$ , with humidity held at  $(38 \pm 6)\%$  RH. During lifetime testing, devices were not covered by an aperture mask, and so device metrics are normalised to their initial values.

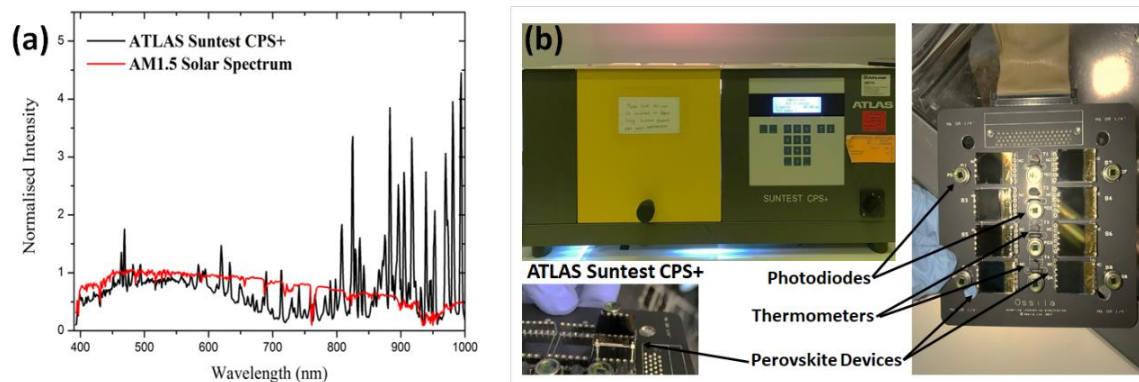


**Figure 6:** (a) Xenon lamp spectra compared to an AM 1.5 solar spectra of the Atlas Suntest CPS+, [Figure from Edward S. R. Bovill's thesis 'The Air Stability and Operational Lifetime of Organic Photovoltaic Materials and Devices'] and (b) Image of the Atlas Suntest CPS+ with photodiodes, thermometers and connected devices.

## 3.5: Microscopy and Spectroscopy

### 3.5.1: X-Ray Diffraction

X-ray diffraction (XRD) is a commonly used technique to analyse the atomic spacing and crystal structure of a material.<sup>[15-17]</sup> The process of XRD occurs through a scattering of electromagnetic waves (X-rays) by periodic structures that occur over angstrom length-scales ( $10^{-10}$  m). This size is coincident with the wavelength of the incident radiation as shown in Figure 7.

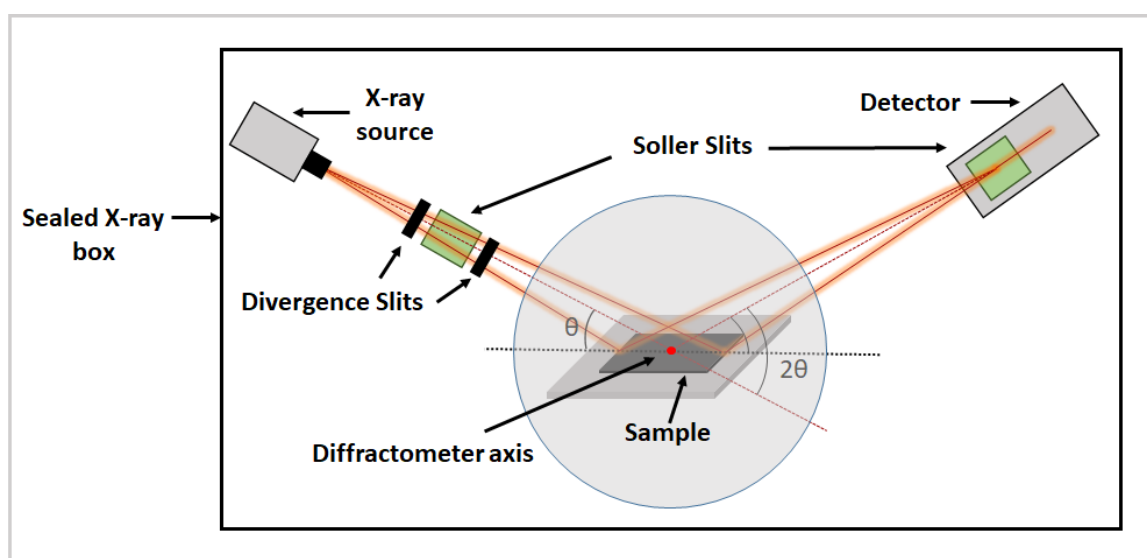


**Figure 7:** Representation of the diffraction scattering process during an XRD experiment.

The X-rays generated by a cathode ray tube are typically focused on a substrate of interest. On contact with the sample, incident rays can undergo constructive interference as defined by Bragg's law (see Equation 2).<sup>[18,19]</sup> This law equates the wavelength of electromagnetic radiation ( $\lambda$ ) (usually  $\text{Cu K}\alpha_1 = 1.5406 \text{ \AA}$ ) to the angle of diffraction ( $\theta$ ) and the lattice spacing ( $d$ ) of a crystalline sample with  $n$  being the order of interference.

$$2d \sin \theta = n\lambda \quad (\text{Eq.2})$$

Here, measurements are typically made over an angular range between  $0.5^\circ$  and  $100^\circ 2\theta$ , corresponding to lattice spacings between 0.1 nm to 20 nm. The X-rays diffracted by the surface are then detected and analysed. Diffraction can occur from the different atomic planes of a sample and will generate a range of diffraction patterns that can then be used to determine the atomic arrangement within a crystal.

Here, XRD data was collected using a PAN-alytical X'Pert Pro. This machine was run using a Philips PW3050/60 ( $\theta/\theta$ ) X-ray generator diffractometer (240 mm diameter) having a PW3064 sample spinner. For the purpose of data collection, a 1D-detector in Bragg-Brentano geometry employed a Copper Line Focus X-ray tube with  $K\alpha$  radiation ( $K\alpha_1 = 1.5406 \text{ \AA}$ ,  $K\alpha_2 = 1.5444 \text{ \AA}$ ,  $K\alpha$  ratio 0.5,  $K\alpha_{\text{avg}} = 1.5419 \text{ \AA}$ ), and a Ni  $k\beta$  absorber (0.02 mm;  $K\beta = 1.392250 \text{ \AA}$ ). To generate X-rays, a Cu anode was used with a 45 kV supply at a tube current of 40 mA. Data was recorded over the angle range  $5.00^\circ$  to  $80.00^\circ 2\theta$ , at a step size of  $0.0131^\circ$ .

### **3.5.2: Scanning Electron Microscopy**

Scanning Electron Microscopy (SEM) is a tool that can be used to image a surface of interest. A schematic of an SEM is shown in Figure 8. An SEM works by scanning a focused electron probe over a surface while recording the intensity of the backscattered signal. Here, the interaction between the incident electrons and the sample material generates a signal that is then converted to form an image.<sup>[20]</sup>

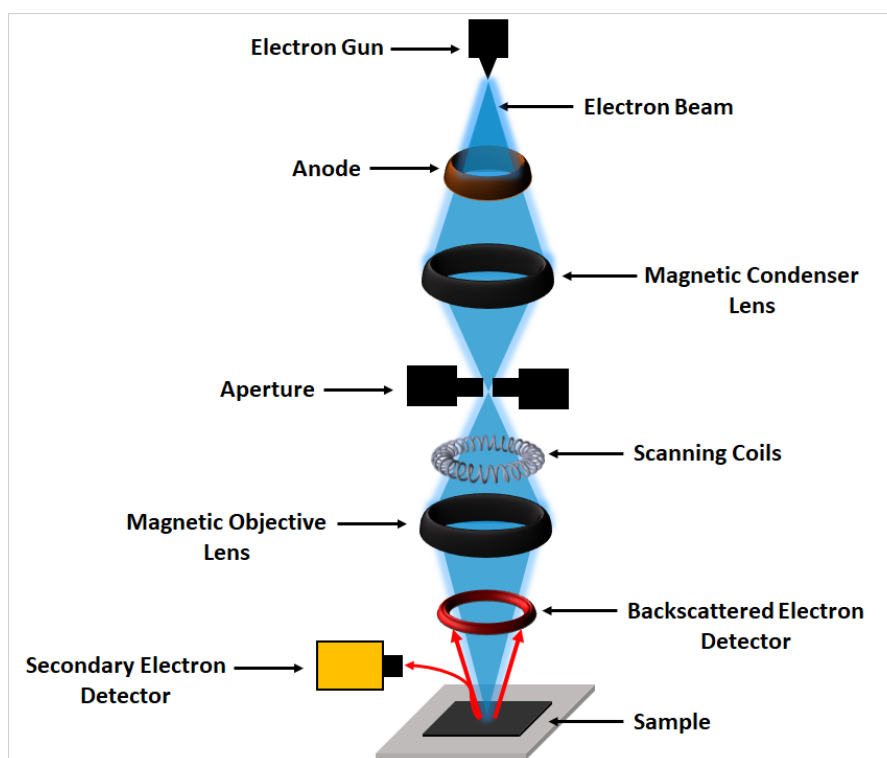


**Figure 8:** Schematic showing surface imaging achieved by the SEM.

An electron beam is generated using a field emission gun composed of a heated tungsten filament positioned on the top of the SEM instrument together with an acceleration voltage ranging from 1 to 30 kV. The electron beam generated is then directed and focussed on to the sample through the use of condenser lenses and objective lenses. The electrons scatter from the surface and are then collected by a detector. The detector generates a signal from the electrons collected that is sent to a computer to be processed into an image. High-resolution images can be achieved using high voltages in the range of 1-25 kV.

Here, surface and cross-section imaging of the perovskite layer was done on a thin film and a complete device respectively using a Carl Zeiss-modified Raith Nanofabrication SEM with an attached in-lens detector. This was set to a working distance of approximately 2.5 mm. As a protective measure to prevent damage to the sample, a low accelerating voltage of 1.5 kV was used, and the pressure of the

gun chamber was maintained at approximately  $<10^{-9}$  mBar. The pressure of the sample chamber was reduced to a minimum of  $10^{-6}$  mBar before imaging.

### 3.5.3: Atomic Force Microscopy

Atomic Force Microscopy (AFM) is a technique used to map surface topography. The technique utilises a fine tip that is placed on a cantilever and is scanned over a surface to map its surface topography. When the tip approaches a surface, the cantilever is attracted to the surface owing to the attractive forces that exist between the surface and the tip. Attractive forces (van der Waals interactions) occur when two opposite-charges attract each other. However when the cantilever comes in contact with the surface, the tip is deflected away from the surface owing to the repulsive forces that are generated. Repulsive forces are generated due to electron-electron (like-charges) that repulse each other. This process is shown in Figure 9(a). Three modes are used in AFM imaging<sup>[21]</sup>; contact mode, non-contact mode, and tapping mode as shown in Figure 9(b).<sup>[22]</sup>

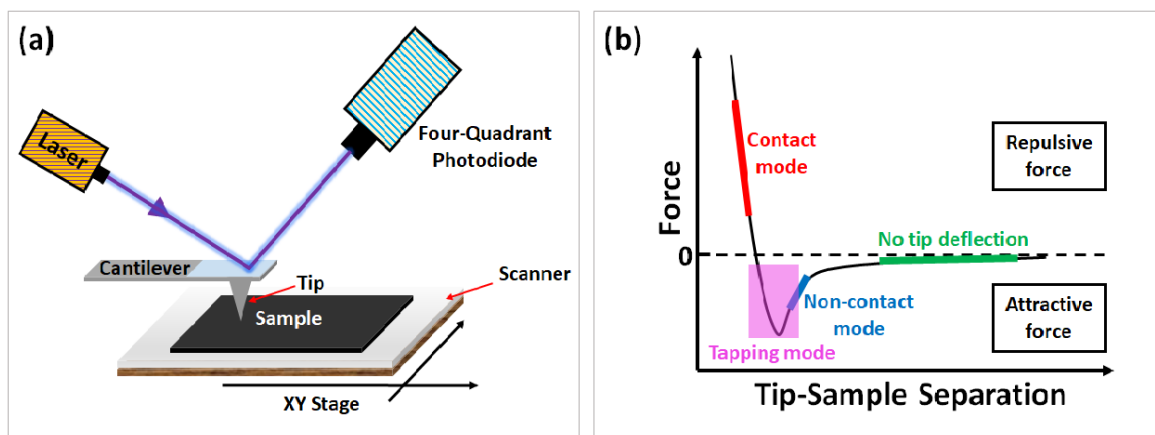


**Figure 9:** (a) Schematic diagram of the AFM used to measure surface morphology and (b) the AFM force-separation curve.

Contact mode is most suited for imaging hard surfaces; here the tip pushes against the surface however the process is controlled such that there is no damage to the

surface. In non-contact mode, there is a distance that separates the tip and the surface, resulting in reduced tip-surface interactions.

In tapping mode, damage to the surface is reduced as the cantilever oscillates, with the tip gently tapping the surface when scanning.<sup>[23]</sup> Here, the tip of the cantilever oscillates at a frequency close to that of its resonance frequency. The amplitude and phase of the tip is dependent upon the distance between the sample and tip. The movement of the tip is assessed using a feedback loop, with such oscillations changing due to the composition of the surface. Here, the height of the cantilever can be altered if required.<sup>[24]</sup>

Here, imaging was carried out on a thin film using a Veeco Dimension 3100 instrument equipped with a nanoscope 3A feedback controller in tapping mode. The feedback controller had a Z limit of 4  $\mu\text{m}$ , with the probe (spring constant of 42  $\text{Nm}^{-1}$ ) oscillated at a resonance frequency of approximately 320 kHz.

#### **3.5.4: Dektak Surface Profilometry**

The thickness of films and their surface roughness was measured using a Bruker DektakXT profilometer. To measure film thickness, it was firstly scratched with a scalpel and then cleaned with compressed nitrogen. Then film thickness was measured by scanning a stylus (12.5 $\mu\text{m}$  tip radius) across the sample placed on XY-stage using 3 mg stylus force. At least three scans/readings were made across each scratch allowing three estimates of film thickness to be made, with their mean value being taken. Figure 10 shows a schematic of the thickness measurement.

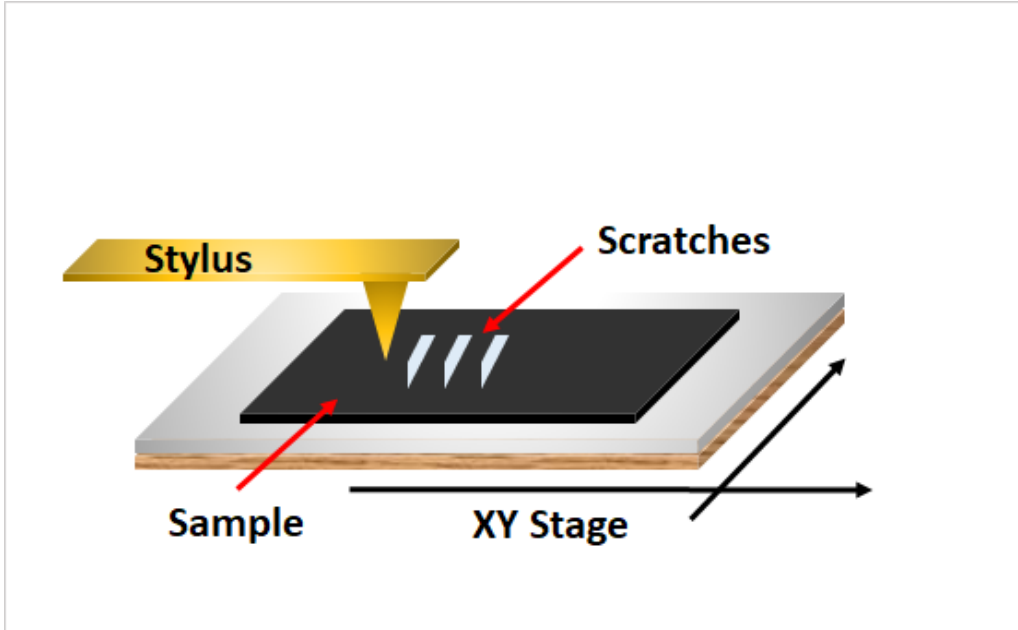


**Figure 10:** Schematic diagram of a surface profilometry.

### 3.5.5: UV-vis Absorbance

UV-vis absorbance measurements were made to characterise light absorption by the perovskite films. Here, the absorbance and transmission of the incident light passing through a sample was studied across the electromagnetic spectrum. This spectrum can be subdivided into three regions: near UV (185-400 nm), visible region (400-700 nm) and near-infrared region (700-1100 nm). When light passes through a thin film or a translucent liquid, it can be absorbed. Optical transmittance can be characterised via the (wavelength dependent) intensity of incident ( $I(\lambda)$ ) and transmitted light ( $I_0(\lambda)$ ) as defined by equation 3.<sup>[25]</sup>

$$T(\lambda) = \frac{I(\lambda)}{I_0(\lambda)} \quad (\text{Eq.3})$$

The absorbance of the film can then be defined using Equation 4.<sup>[25]</sup>

$$A(\lambda) = -\log_{10}(T(\lambda)) = -\log_{10}\left(\frac{I(\lambda)}{I_0(\lambda)}\right) \quad (\text{Eq.4})$$

It can be seen that the efficiency of light absorption depends upon photon energy. Photon energy is defined in terms of its frequency or wavelength as shown using equation 5, where  $E$  is the energy of light,  $h$  is Planck's constant,  $\nu$  is its frequency,  $c$  is the speed of light and  $\lambda$  is its wavelength. For a molecular system, the absorption of photons by electrons in the ground state (Highest Occupied Molecular Orbital - HOMO), leads to their promotion to an excited state (Lowest Unoccupied Molecular Orbital - LUMO) as shown in Figure 11. This transition occurs when the energy of the photon corresponds to the difference between the HOMO and LUMO energy levels.<sup>[26]</sup>

$$E = h\nu = \frac{hc}{\lambda} \quad (\text{Eq.5})$$

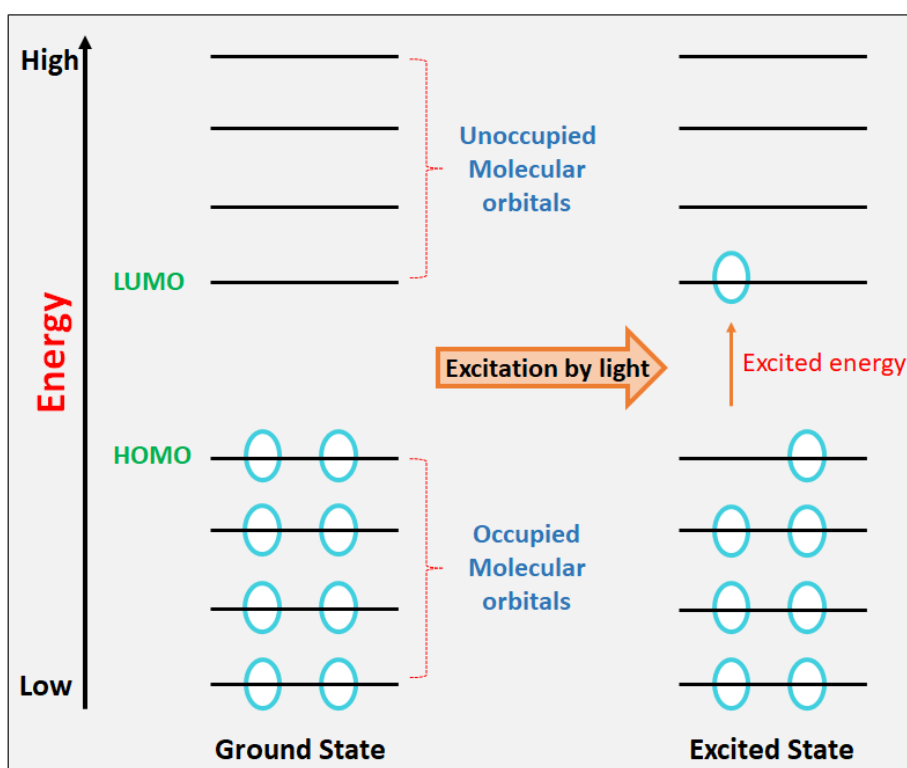


**Figure 11:** An energy level diagram of a molecule indicating HOMO and LUMO levels.

Here, absorption of thin films was measured using an Andor Shamrock SR-193i-A double-grating imaging spectrograph adjusted to a focal length of 0.193m. Spectra

were recorded using a spectrometer equipped with a 150 grooves /mm grating blazed at 500 nm. A tailor-made tungsten lamp source was used to generate white light, which was then focused onto the sample at normal incidence through a pair of lenses. The light transmitted was collimated using a 50X Mitutoyo Plan Apo SL infinity-corrected objective, and then directed into a spectrometer with the use of a final collection lens as shown in Figure 12.

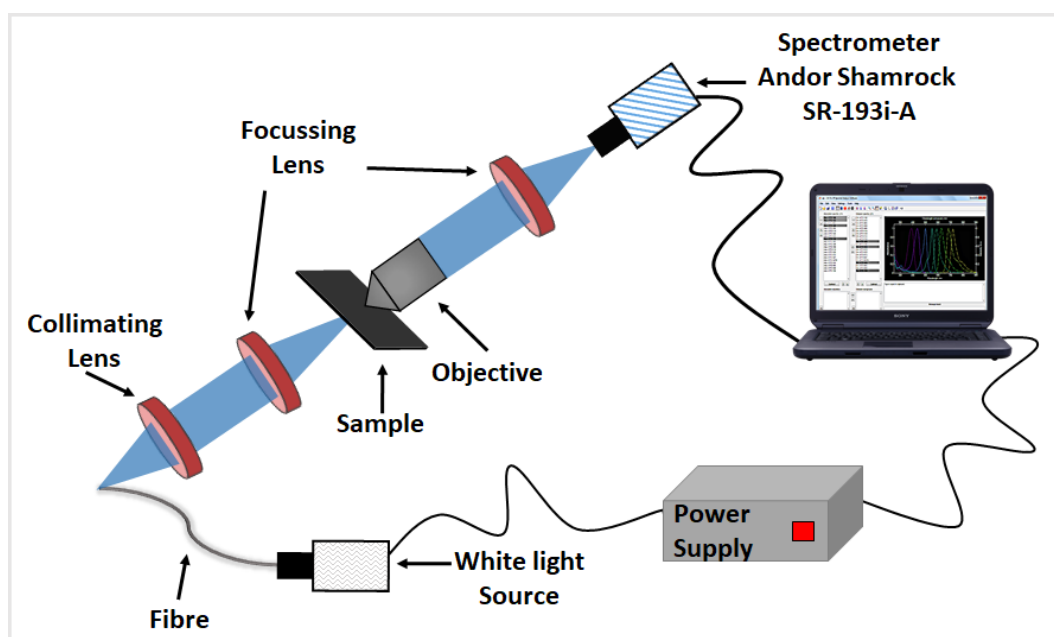


**Figure 12:** Schematic of the absorption and transmission setup. The transmission of the sample is marked in blue.

### 3.5.6: Steady-State Photoluminescence

In photoluminescence (PL) spectroscopy, the exposure of the sample to an incident laser can promote electrons in an electronic ground state ( $S_0$ ) to specific vibrational levels ( $v = 0, 1, 2$ ) in the excited state. An excited electron will then revert back to the lowest vibrational level ( $v = 0$ ) of the  $S_1$  excited state (usually within  $1 \times 10^{-12}$  s) as a result of vibrational relaxation (VR).<sup>[27]</sup> Relaxation involving the emission of a photon can then occur as the electron undergoes relaxation to a vibrational

transition of the  $S_0$  ground state. Numerous factors affect the intensity and spectral distribution of the emitted PL, these include the semiconductor bandgap, together with impurities and defects.<sup>[28]</sup>

Here, PL was measured using an Andor Shamrock SR-303i-A triple-grating imaging spectrograph having a focal length of 0.303m. This was equipped using a 150 grooves /mm grating blazed at 500 nm. A Thorlabs diode laser was used to excite the samples at an incidence angle of  $\sim 15^\circ$ . PL was accumulated at normal incidence using a lens which was directed to a spectrometer via a fibre as shown in Figure 13.

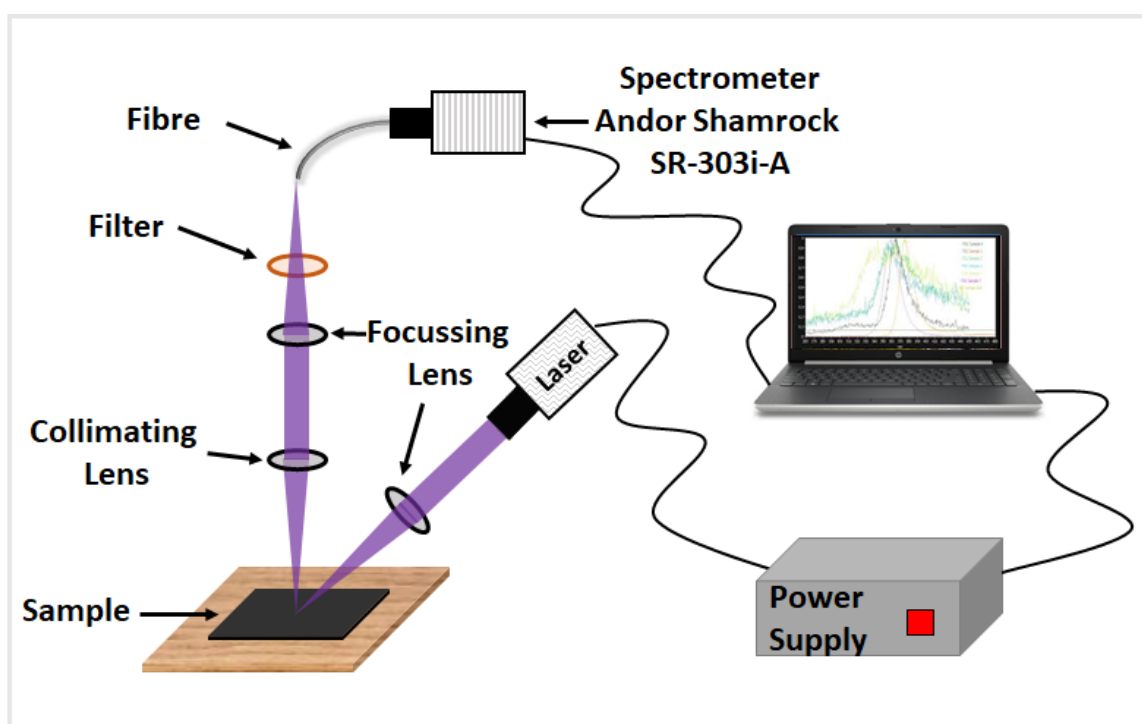


**Figure 13:** Schematic of the steady-state photoluminescence (SSPL) system.

### 3.6: References

- [1] M. D. Tyona, *Adv. Mater. Res.* **2013**, *2*, 195.
- [2] M. Sato, I. Fujii, F. Application, P. Data, P. E. H. Smith, A. E. A. Bell, **1978**.
- [3] N. Sahu, B. Parija, S. Panigrahi, *Indian J. Phys.* **2009**, *83*, 493.
- [4] W. W. Flack, D. S. Soong, A. T. Bell, D. W. Hess, *J. Appl. Phys.* **1984**, *56*, 1199.
- [5] F. C. Krebs, *Sol. Energy Mater. Sol. Cells* **2009**, *93*, 394.
- [6] Ossila, "Spin Coating: A Guide to Theory and Techniques," can be found under <https://www.ossila.com/pages/spin-coating>, **n.d.**
- [7] J. E. Bishop, J. A. Smith, C. Greenland, V. Kumar, N. Vaenas, O. S. Game, T. J. Routledge, M. Wong-Stringer, C. Rodenburg, D. G. Lidzey, *ACS Appl. Mater. Interfaces* **2018**, *10*, 39428.
- [8] J. E. Bishop, C. D. Read, J. A. Smith, T. J. Routledge, D. G. Lidzey, *Sci. Rep.* **2020**, *10*, 6610.
- [9] S. Albrecht, S. Yilmaz, I. Dumsch, S. Allard, U. Scherf, S. Beaupré, M. Leclerc, D. Neher, *Energy Procedia* **2012**, *31*, 159.
- [10] F. Aziz, A. F. Ismail, *Mater. Sci. Semicond. Process.* **2015**, *39*, 416.
- [11] D. M. Mattox, *Handbook of Physical Vapor (PVD) Processing*, **2010**.
- [12] K. H. Lee, H. W. Jang, K.-B. Kim, Y.-H. Tak, J.-L. Lee, *J. Appl. Phys.* **2004**, *95*, 586.
- [13] T. Hu, F. Zhang, Z. Xu, S. Zhao, X. Yue, G. Yuan, *Synth. Met.* **2009**, *159*, 754.
- [14] M. Saliba, J. P. Correa-Baena, C. M. Wolff, M. Stollerfoht, N. Phung, S. Albrecht, D. Neher, A. Abate, *Chem. Mater.* **2018**, *30*, 4193.
- [15] M. Z. Rahman, T. Edvinsson, in *Charact. Tech. Perovskite Sol. Cell Mater.*, Elsevier, **2020**, pp. 23–47.
- [16] Q. Jiang, Y. Zhao, X. Zhang, X. Yang, Y. Chen, Z. Chu, Q. Ye, X. Li, Z. Yin, J. You, *Nat. Photonics* **2019**, *13*, 460.

- [17] B. Li, Y. Zhang, L. Fu, T. Yu, S. Zhou, L. Zhang, L. Yin, *Nat. Commun.* **2018**, *9*, 1076.
- [18] R. A. SMITH, *Nature* **1960**, *188*, 632.
- [19] C. G. Pope, *J. Chem. Educ.* **1997**, *74*, 129.
- [20] G. H. Michler, *Electron Microscopy of Polymers*, Springer Berlin Heidelberg, Berlin, Heidelberg, **2008**.
- [21] E. Meyer, *Atomic Force Microscopy*, Elsevier, **1992**.
- [22] C. C. Lai, J. M. Bell, N. Motta, *Adv. Mater. Res.* **2008**, *32*, 49.
- [23] S. N. Magonov, V. Elings, M.-H. Whangbo, *Surf. Sci.* **1997**, *375*, L385.
- [24] E. Meyer, H. J. Hug, R. Bennewitz, *Scanning Probe Microscopy: The Lab on a Tip*, Springer Berlin Heidelberg, **2004**.
- [25] M. Razeghi, *Long Wavelength Infrared Detectors*, **2020**.
- [26] M. Rudan, *Physics of Semiconductor Devices*, Springer New York, New York, NY, **2015**.
- [27] D. R. Baer, S. Thevuthasan, *Handbook of Deposition Technologies for Films and Coatings*, Elsevier Ltd., **2010**.
- [28] NREL, "Photoluminescence Spectroscopy," can be found under <https://www.nrel.gov/pv/photoluminescence-spectroscopy.html>.

# Chapter 4

---

---

## Investigating the stability of perovskite photovoltaic devices: Role of perovskite compositions and hole transport layers

### 4.0 Introduction

Organic-inorganic halide perovskite solar cells (PSCs) have excellent optoelectronic properties, which along with their fabrication using solution processing methods under low-temperature conditions have made them a serious contender for commercialisation.<sup>[1,2]</sup> In the past few years, PSCs have undergone significant evolution in terms of their structure and composition.<sup>[3,4]</sup> Following these developments, a power conversion efficiency (PCE) of 25.5% has been demonstrated in a single junction device, while Si-perovskite monolithic tandem solar cells have reached an impressive PCE of 29.5%.<sup>[5]</sup>

There has been extensive exploration of “pure” (single cation) perovskites for PSC applications, with such materials including formamidinium lead halide (FAPbX<sub>3</sub>), methylammonium lead halide (MAPbX<sub>3</sub>), and cesium lead halide (CsPbX<sub>3</sub>), where X is bromide (Br) or iodide (I) (see discussion in Chapter 2). However, the use of these compounds has led to several issues. For instance, while several attempts have been made to improve the PCE of MAPbI<sub>3</sub>, it has so far only demonstrated a limited performance. Furthermore, MAPbI<sub>3</sub> also raises concerns in terms of its possible environmental impact and structural stability when exposed to moisture, oxygen,

and high temperatures.<sup>[6]</sup> Low intrinsic stability of MAPbI<sub>3</sub> leads to loss of methylammonium ions under external stress factors like heat and moisture that results in poor device stability of MAPbI<sub>3</sub> photovoltaic devices under operational conditions.<sup>[7-9]</sup> In contrast, formamidinium lead iodide (FAPbI<sub>3</sub>) shows good promise due to its higher resistance to the loss of cation (FA<sup>+</sup>) upon heat and possibility of crystallising in a photoactive  $\alpha$ - phase with lower band gap ( $E_g \approx 1.47$  eV)<sup>[10]</sup> than MAPbI<sub>3</sub>.<sup>[11,12]</sup> However, due to large cation size of FA<sup>+</sup>, the compound FAPbI<sub>3</sub> tends to crystallise in a non-perovskite structure  $\delta$ -phase with high band gap  $E_g \approx 2.43$  eV and poor optoelectronic properties. One way to address this issue is by incorporating fraction of smaller cations than FA<sup>+</sup> to bring down the net tolerance factor to the range ( $0.9 < t < 1.0$ ) and drive crystallisation into a perovskite phase. Alloying small amount (10 – 20%) of MA<sup>+</sup> and Br<sup>-</sup> in FAPbI<sub>3</sub> was shown to improve phase stabilisation of FAPbI<sub>3</sub>.<sup>[13]</sup> However, double cation mixed halide FA/MA Pb(I/Br) perovskites were later found to be sensitive to processing conditions and have an intrinsic structural and thermal instability which drives PSC degradation under illumination.<sup>[14,15]</sup>

The inorganic Cs<sup>+</sup> cation has attracted a significant attention in this regard due to its small ionic radius of 1.81Å as compared to 2.7Å and 2.79Å for MA and FA, respectively.<sup>[16]</sup> Lee *et al.* found that adding a small amount of Cs into FAPbI<sub>3</sub> improved PSC PCE from 14.9% to 16.5% and more importantly, this led to higher stability in device performance.<sup>[17]</sup> Qiu *et al.* also found that there was considerable improvement in the thermal and environmental phase stability following the use of Cs/FA cation-mixture, with devices achieving a PCE as high as 19.3%.<sup>[18]</sup> These

studies showed that there is a significant positive impact of Cs<sup>+</sup> incorporation in term of photovoltaic performance and long-term operational stability.

Recently incorporation both Cs<sup>+</sup> and MA<sup>+</sup> within FAPbI<sub>3</sub> to form 'triple-cation' composition demonstrated formation of large uniform grains with size greater than 400 nm, high phase purity with little to no yellow  $\delta$ -phase formation and excellent structural stability under illumination as compared to FA/MA perovskites.<sup>[19]</sup> Recently, several halides (I, Br, and chloride (Cl<sup>-</sup>)), organic cations (MA<sup>+</sup>, FA<sup>+</sup>), and alkali metals ions such as Cs<sup>+</sup>, sodium (Na<sup>+</sup>), potassium (K<sup>+</sup>) and rubidium (Rb<sup>+</sup>) have been incorporated as a part of "triple-cation" composition, with devices demonstrating high efficiencies.<sup>[14]</sup> However, the detailed investigation of the long term operational stability of triple-cation compositions are still missing. Therefore, in this study the influence of composition (triple-cation vs MAPbI<sub>3</sub>) on operational stability of PSC has been investigated.

The hole transporting material (HTM) is a key component that plays a crucial role in the stability of PSC devices. One of the most widely used HTMs in PSCs is spiro-OMeTAD which possesses a reasonably high glass transition temperature ( $T_g = 80 - 120$  °C), a hole mobility of  $\sim 10^{-4}$  cm<sup>2</sup> V<sup>-1</sup> s<sup>-1</sup>, and suitable HOMO level for efficient hole extraction from a perovskite.<sup>[20-25]</sup> When spiro-OMeTAD is used as a HTM it is often doped with (a) 4-tert-butylpyridine (tBP) which increases its solubility in chlorobenzene and (b) lithium bis(trifluoromethane)sulfonimide (LiTFSI) as well as tris(2-(1*H*-pyrazol-1-yl)-4-*tert*-butylpyridine)cobalt(III)tri[hexafluorophosphate] (FK209) to improve its electrical conductivity. However, it has been shown that Li<sup>+</sup> species in spiro-OMeTAD can migrate under operational conditions causing dedoping of spiro-OMeTAD.<sup>[26]</sup> Additionally, the hygroscopic nature of LiTFSI makes

the perovskite solar cell stack more susceptible to the effects of moisture.<sup>[27,28]</sup> The synthesis of spiro-OMeTAD is relatively complicated and it requires careful purification; features that might hinder its widespread use.<sup>[29,30]</sup> A number of researchers have explored new HTMs for PSC applications. For example, Saliba *et al.* have successfully used Poly[bis(4-phenyl)(2,4,6-trimethylphenyl)amine] (PTAA) as a HTM in an inverted (*p-i-n*) structure device and demonstrated a PCE of 21.6% together with high stability under maximum power point (MPP) tracking at 85 °C over a period of 500 hours under full illumination.<sup>[31]</sup> Matsui *et al.* have also reported similar findings when using PTAA in a planar architecture (*n-i-p*) device, with a certified PCE of 20.1% reported. Encouragingly, these studies reported that the champion device retained 92% of its initial efficiency after testing at a temperature of 85 °C and a relative humidity (RH) of 85% for the period of 1000 hours.<sup>[32]</sup>

In this chapter, a detailed series of comparative measurements are performed on a triple-cation perovskite  $\text{Cs}_{0.05}\text{FA}_{0.79}\text{MA}_{0.15}\text{PbI}_{2.45}\text{Br}_{0.55}$  with an excess of  $\text{PbI}_2$  and it is benchmarked against PSC devices based on  $\text{MAPbI}_3$ . A series of techniques are used to explore device efficiency and materials properties, including X-ray scattering (XRD), scanning electron microscopy (SEM), atomic force microscopy (AFM), UV-Vis absorption and photoluminescence (PL). The relative stability of devices and films are then explored under conditions such as humidity, temperature and illumination up to two suns. It is found that the triple-cation perovskite films perform well under such conditions. It is shown that PSCs based on a triple-cation perovskite have improved performance, reduced hysteresis and significantly improved long-term stability with T80 lifetime of 300 hours as compared to the  $\text{MAPbI}_3$  control. The relative stability of devices are also compared when either utilising spiro-OMeTAD

or PTAA as HTMs. It is found that the triple-cation PSCs using a spiro-OMeTAD as HTM show worse thermal stability than those using a PTAA HTM. These results confirm that further investigation of HTMs and interlayers is essential to achieve high performance and long-term stability before they can become commercially viable.

## 4.1 Results and Discussion

### 4.1.1 Photovoltaic performance

In this section, the impact of perovskite composition on device performance is explored, and a mixed cation and halide triple-cation (Cs/FA/MA) perovskite is compared with the well-known hybrid perovskite (MAPbI<sub>3</sub>). Device fabrication is discussed in more detail in chapter 3, section 3.3. Here, the triple-cation perovskite explored had the solution composition Cs<sub>0.05</sub>FA<sub>0.79</sub>MA<sub>0.15</sub>PbI<sub>2.45</sub>Br<sub>0.55</sub>. All fabricated devices had an *n-i-p* architecture and used a commercially accessible tin (IV) oxide (SnO<sub>2</sub>) nanoparticle as the electron transport layer (ETL) and spiro-OMeTAD as a HTL. The final structure of devices fabricated is glass/ITO/SnO<sub>2</sub>/perovskite/spiro-OMeTAD/Au as shown in Figure 1(a).

In Figure 1(b) the current density-voltage (*J-V*) performance is plotted for champion devices using MAPbI<sub>3</sub> and Cs/FA/MA perovskites. It can be seen that there is a significant improvement in most *J-V* performance metrics when using a triple-cation perovskite compared to MAPbI<sub>3</sub>. MAPbI<sub>3</sub>-based devices reach a maximum PCE of 16% with an open-circuit voltage (*V*<sub>oc</sub>) of 0.99 V, a short-circuit current density (*J*<sub>sc</sub>) of 22.37 mA cm<sup>-2</sup>, and a fill factor (FF) of 72.15%. In contrast, the triple-cation PSCs based devices attain a champion PCE of 19.5%, with a *V*<sub>oc</sub> of 1.08 V, *J*<sub>sc</sub> of 22.43 mA cm<sup>-2</sup>, and FF of 80.48%. In Figure 2, statistical box plots are plotted of the

performance metrics determined from a total of 15 devices for each material system. Champion device metrics alongside average values in parentheses are tabulated in Table 1. It is interesting to note that this improvement in device performance on using the triple-cation perovskite is accompanied by significant reduction in  $J$ - $V$  hysteresis (see Figure 1(b)). Hysteresis can be quantified using the hysteresis index (HI) as defined in equation 1. Using this, it is found that for the champion devices, there is a decrease in HI from 0.185 for MAPbI<sub>3</sub> to 0.017 for the triple-cation perovskite. Despite lower performance of MAPbI<sub>3</sub>, their performance improved significantly compared to other previously reports based on the same device architecture. For example, Bai *et al.* fabricated devices with MAPbI<sub>3</sub> as an active layer with SnO<sub>2</sub> and spiro-OMeTAD as transporting materials and achieved a PCE of 15.7%.<sup>[33]</sup> However, triple-cation perovskite devices showed comparable performance in agreement with previous work.<sup>[34,35]</sup>

$$HI = \frac{PCE(reverse) - PCE(forward)}{PCE(reverse)} \quad (Eq. 1)$$

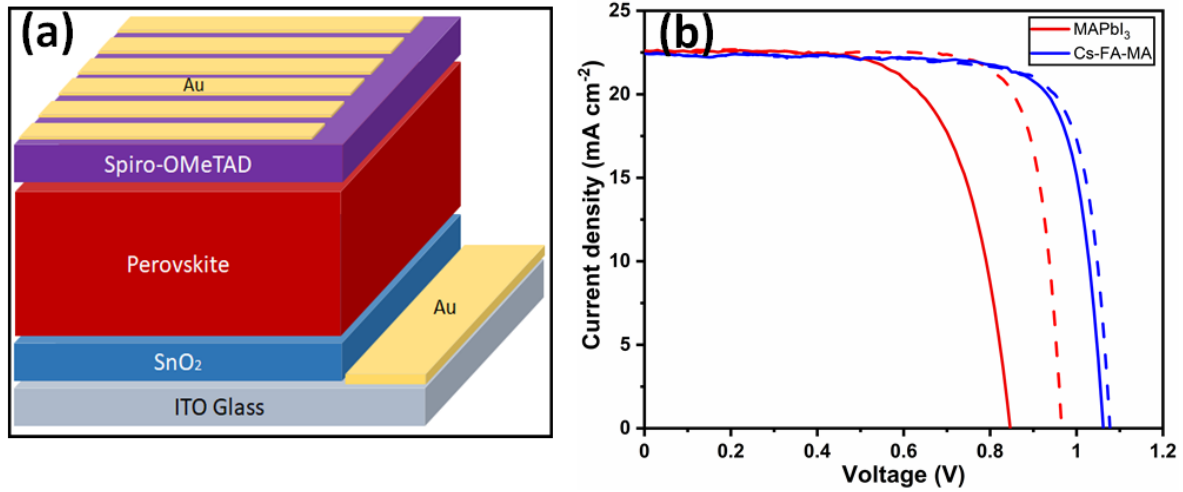


**Figure 1.** (a) Schematic representation of the structure of the perovskite solar cell studied. (b) Current density-voltage curves for the champion devices based on  $\text{MAPbI}_3$  and triple-cation perovskites. Forward ( $J_{sc}$  to  $V_{oc}$ ) sweep directions are indicated by solid lines and reverse ( $V_{oc}$  to  $J_{sc}$ ) sweep directions are indicated by dashed lines.

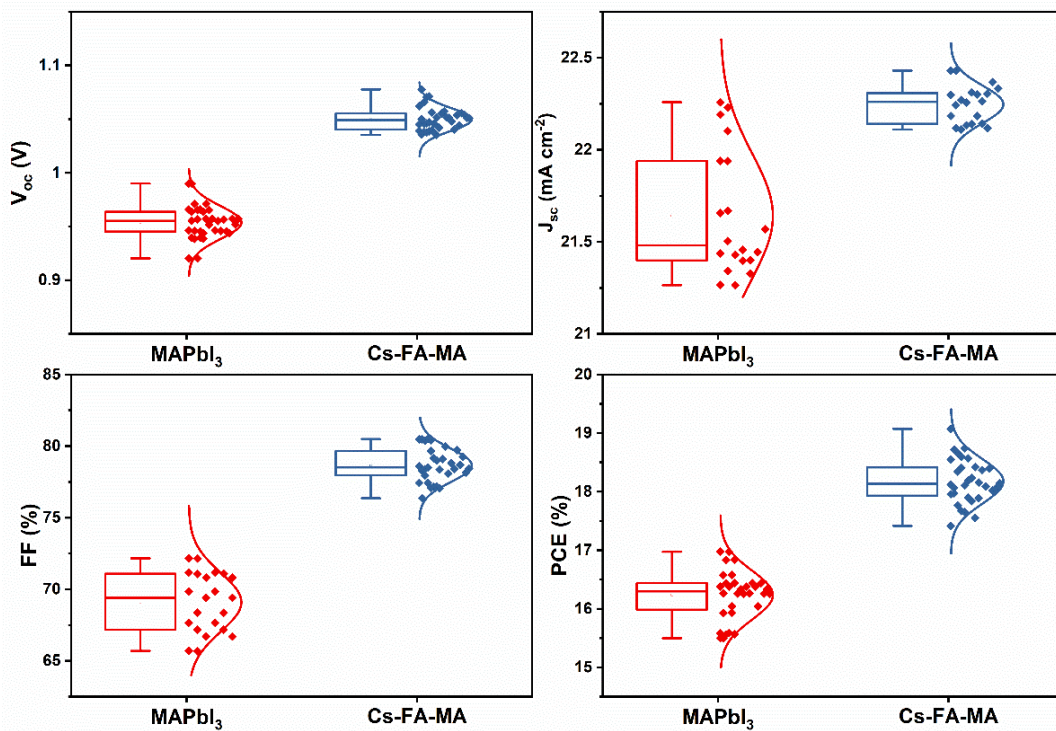


**Figure 2.** Statistical box plots for the performance (reverse scan) determined for all the perovskite solar cell devices.

<i>Perovskite</i>	<i>V<sub>oc</sub> (V)</i>	<i>J<sub>sc</sub> (mA cm<sup>-2</sup>)</i>	<i>FF (%)</i>	<i>PCE (%)</i>
<b>MAPbI<sub>3</sub></b>	<b>0.99 (0.95 ±0.02)</b>	<b>22.37 (21.64 ±0.34)</b>	<b>72.15 (69.26 ±1.97)</b>	<b>15.97 (14.24 ±0.42)</b>
<b>Cs-FA-MA</b>	<b>1.08 (1.05 ±0.01)</b>	<b>22.43 (22.25 ±0.10)</b>	<b>80.48 (78.66 ±1.16)</b>	<b>19.50 (18.38 ±0.38)</b>

**Table 1.** Summary of reverse scan ( $V_{oc}$  to  $J_{sc}$ ) performance metrics of champion PSC devices and the average values recorded from a minimum of 20 cells per testing condition (shown in parentheses).

#### 4.1.2 Thin film topography and X-ray diffraction analysis

Having determined that PSC devices based on the triple-cation perovskite show improved photovoltaic performance, the origins behind such improvements are now explored. In the following section, the structure and crystallinity of the two perovskite materials are compared. Figure 3(a) plots typical SEM images that have been recorded from a MAPbI<sub>3</sub> control and a triple-cation perovskite film. It is found that the average grain size of MAPbI<sub>3</sub> polycrystalline films prepared is in the range of 100 to 400 nm. However, the grain size of polycrystalline triple-cation film is found in the range of 200 nm to 750 nm with most of the grains being larger than 400 nm. Additionally, the triple-cation perovskite films exhibit regions that contain bright/white crystallites as shown in Figure 3(b), with these features known to be rich in PbI<sub>2</sub>.<sup>[36]</sup>

To complement these measurements, AFM topography measurements were also performed on perovskite films that were deposited on top of ITO/SnO<sub>2</sub>. Typical surface scans are shown in Figure 4. Here, it is found that the MAPbI<sub>3</sub> film had a RMS roughness of 36.79 nm compared to 19.71 nm in the case of triple-cation perovskite (see Table 2). These measurements confirm that triple-cation perovskites form

significantly more uniform, large grain and smooth films as compared to MAPbI<sub>3</sub> complementing observations from SEM.

Since the hybrid perovskite films made using solution processing are polycrystalline, the average grain size of such polycrystalline films has a significant effect on their optoelectronic performance. Polycrystalline films consist of grains with grain-boundaries that display discontinuity in crystallographic orientations along with additional compositional defects such as vacancies and un-coordinated atoms. Therefore, in addition to offering resistance to charge transport due to crystallographic disorientations, grain boundaries can act as recombination centres for photo-generated carriers. Since the charge transport within perovskite film takes place perpendicular to the plane direction, reducing the density of lateral grain-boundaries is important to reduce resistance to transport and minimise photo-carrier recombination at the grain boundaries. Therefore, achieving a grain size close to the thickness of perovskite film (~600 nm) results in grains which span the thickness of perovskite films with minimal number of in-plane grain boundaries. The triple-cation perovskite films prepared in this study possesses average grain size close to 550 nm and thus devices out-perform MAPbI<sub>3</sub> PSCs which have smaller average grain sizes (~250 nm). The variation in grain size could also explain observed difference in the hysteresis of triple-cation and MAPbI<sub>3</sub> based PSCs. It has been shown theoretically as well as experimentally that hybrid lead halide perovskites are prone to formation of cationic and anionic vacancy defects such as MA<sup>+</sup>/FA<sup>+</sup> and Br<sup>-</sup>/I<sup>-</sup> respectively. These charged vacancy defects lead to ion-migration due to electric field (or photo-voltage) generated under operational conditions such as one sun illumination. This ion-migration and interfacial

accumulation has been attributed to observed hysteretic behaviour in  $J$ - $V$  curves of perovskite solar cells. Grain boundaries have been shown to be more susceptible to vacancy defect formation than the bulk of crystallites. Additionally, grain boundaries have been predicted to facilitate vacancy mediated ion-migration.<sup>[37-39]</sup> Therefore, perovskite films with smaller average grain size have higher  $J$ - $V$  hysteresis than those having large average grain size; a factor that explains the trends observed here for  $\text{MAPbI}_3$  vs triple-cation PSCs.

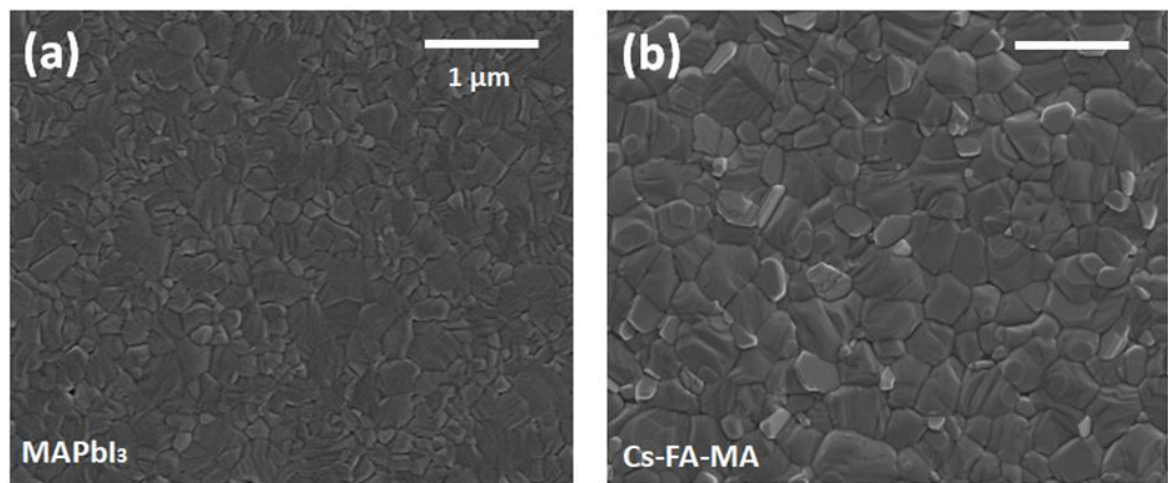


**Figure 3.** SEM of (a)  $\text{MAPbI}_3$  and (b) triple-cation perovskite films.

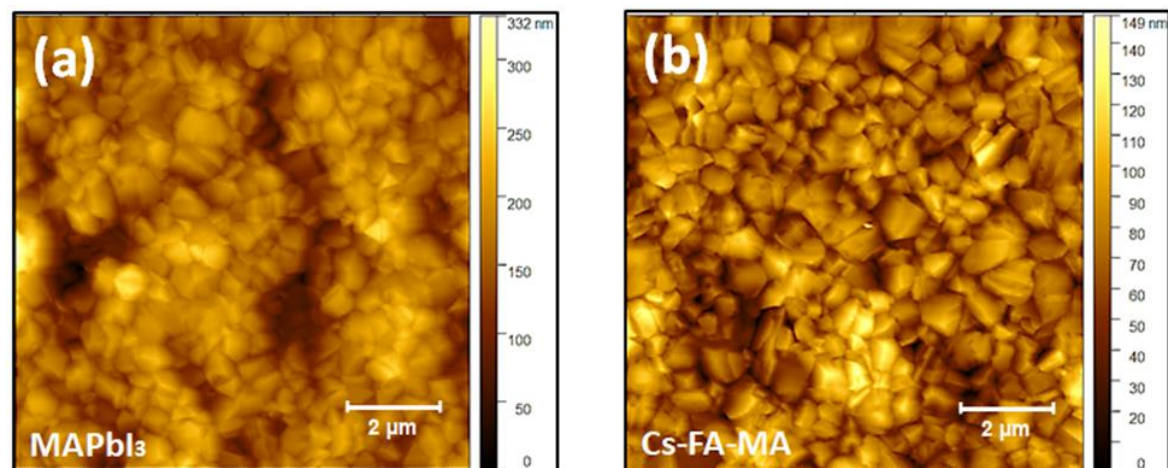


**Figure 4.** AFM images of (a)  $\text{MAPbI}_3$  and (b) triple-cation perovskite films.

<i>Perovskite</i>	<i>RMS roughness (Sq) (nm)</i>	<i>Mean roughness (Sa) (nm)</i>
<b>MAPbI<sub>3</sub></b>	<b>36.79</b>	<b>28.82</b>
<b>Triple-cation</b>	<b>19.71</b>	<b>15.73</b>

**Table 2.** Root-mean-square (RMS) of MAPbI<sub>3</sub> and triple -cation perovskite solar cells.

To further understand film structure, XRD and grazing-incidence wide-angle X-ray scattering (GIWAXS) were used to compare crystalline structure within MAPbI<sub>3</sub> and triple-cation films. XRD patterns are plotted for MAPbI<sub>3</sub> and triple-cation films in Figure 5. Here, these measurements were made on a glass/SnO<sub>2</sub>/perovskite. It can be seen that the triple-cation films have a diffraction peak at  $2\theta = 12.7^\circ$ ; a feature that suggests the existence of excess PbI<sub>2</sub>. However, this peak was not found in MAPbI<sub>3</sub> (see Figure 5). Specifically, in MAPbI<sub>3</sub> we determine characteristic peaks at  $2\theta = 14.1^\circ$ ,  $28.4^\circ$ , and  $31.9^\circ$  which correspond to the (110), (220), and (310) planes of tetragonal crystal structure of MAPbI<sub>3</sub> with space group I4/mcm,<sup>[40]</sup> with these features being in excellent agreement with the reported diffraction patterns reported in literature.<sup>[41]</sup>

In the triple-cation perovskite composition peaks are identified at  $2\theta = 14.1^\circ$ ,  $20^\circ$ ,  $24.5^\circ$ ,  $28.4^\circ$ ,  $31.9^\circ$  and  $35^\circ$  corresponding to the (001), (011), (111), (002), (012), and (112) planes which are characteristic of a cubic structure with *Pm3m* space group.<sup>[42]</sup> Here, the additional scattering features evident in the triple-cation perovskite are consistent with its enhanced compositional complexity; an observation in agreement with earlier studies.<sup>[36,43]</sup>

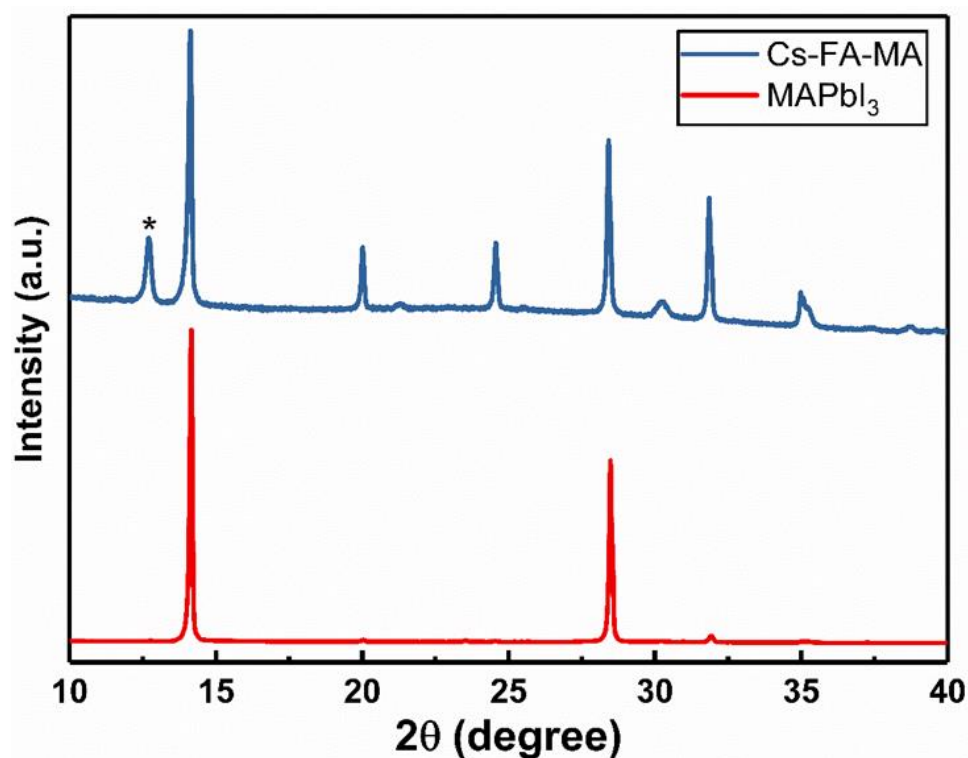


**Figure 5.** The XRD patterns of MAPbI<sub>3</sub> and triple-cation perovskite on ITO/SnO<sub>2</sub> substrates.

### 4.1.3 Photoluminescence and absorption

Having characterised film structure, attention is now turned to their optical properties. Here, the steady-state PL emission for MAPbI<sub>3</sub> and triple-cation perovskite films were measured, together with UV-Vis absorption spectra. Here, Figure 6(a) plots PL emission for the two films. It is found that emission peaks at 771.4 nm for MAPbI<sub>3</sub> and 758 nm for the triple-cation perovskite. To confirm that this differences in PL emission results from a difference in the band gap energy, the film absorption was measured as shown in Figure 6(b). Here, an approximate energy-gap was determined for MAPbI<sub>3</sub> of 1.57 eV and 1.6 eV for the triple-cation perovskite; a result in good agreement with the observed blue-shift of the PL emission in the triple-cation perovskite. Pure  $\alpha$ -FAPbI<sub>3</sub> has a band gap of 1.47 eV and has a PL emission around 840-850 nm. However, as discussed earlier triple-

cation composition is formed by alloying 14% MA<sup>+</sup> and 5% Cs<sup>+</sup> at the ‘cationic’ sites and 18% Br<sup>-</sup> at the ‘anionic’ sites of FAPbI<sub>3</sub> which increases band gap to 1.6 eV.<sup>[19,44–46]</sup> Despite the higher band gap of triple-cation composition, similar J<sub>sc</sub> values are observed in both triple-cation and MAPbI<sub>3</sub> champion devices. Here, the higher grain size characteristic of triple-cation films makes it possible to deposit films with thickness up to 600 nm without significantly increasing the density of in-plane grain boundaries. Conversely, the MAPbI<sub>3</sub> thickness has to be limited to 400 nm due to lower grain size, with thicker films leading to lower photovoltaic performance parameters. Thus the higher thickness of the triple-cation film can compensate its reduced light harvesting ability due to its larger band gap compared to MAPbI<sub>3</sub>.

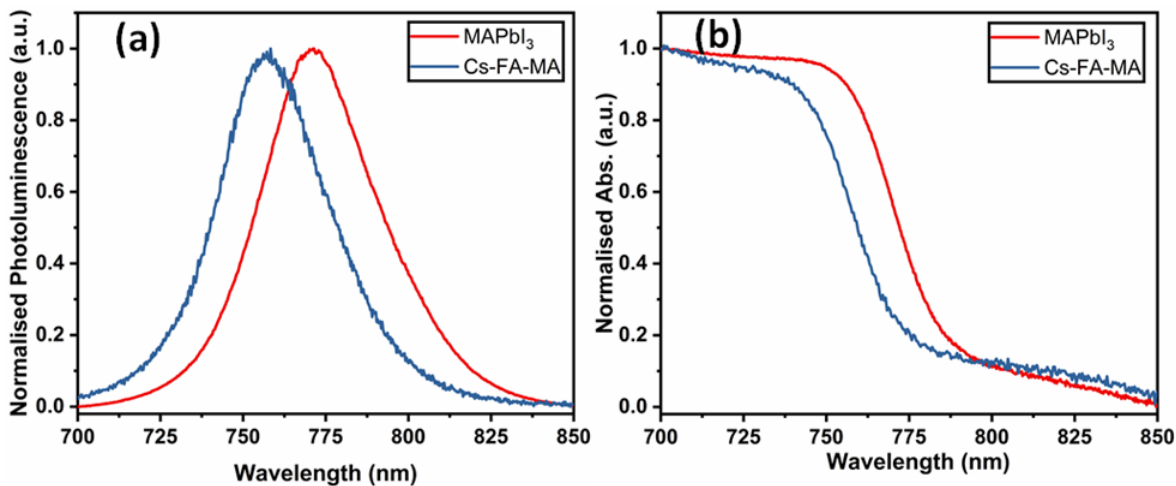


**Figure 6.** Normalised (a) photoluminescence and (b) UV-Vis absorption for MAPbI<sub>3</sub> and triple-cation perovskite films.

#### 4.1.4 Stability of triple-cation PSCs

Now we have established the basic properties of the different perovskite films and have introduced their device properties, we next consider the stability of both the constituent materials and devices.

Firstly, the relative stability of MAPbI<sub>3</sub> and triple-cation perovskite on an ITO/SnO<sub>2</sub> substrate are explored using X-ray scattering to monitor the degradation of the perovskite material under accelerated aging (stress) conditions. Here, representative perovskite thin-films were mounted in a testing chamber and held under LED illumination ( $200 \pm 10 \text{ mWcm}^{-2}$  irradiation), at a temperature ( $50 \text{ }^\circ\text{C}$ ), and RH~ 61%. The degradation of the films was then tracked by performing GIWAXS measurements using X-rays produced by the Diamond Light Source synchrotron at beam-station I22. GIWAXS measurements were recorded every 10 and 30 minutes over a period of ~ 8 hours. Typical data is shown in Figure 7 where scattering spectra are plotted that were recorded from the MAPbI<sub>3</sub> and triple-cation perovskite films.

Before accelerated degradation testing the MAPbI<sub>3</sub> and triple-cation perovskite scattering patterns are dominated by the (110) and (001) peaks respectively. The perovskite phase for both films is observed at  $Q = 1 \text{ \AA}^{-1}$  which is in agreement with previously reported work.<sup>[44,47,48]</sup> Notably, a PbI<sub>2</sub> peak is seen at  $\sim 0.9 \text{ \AA}^{-1}$  in the triple-cation perovskite, and is oriented in the out-of-plane ( $Q_z$ ) direction (see Figure 7(b)); with both features being consistent with earlier findings using SEM and PXRD.<sup>[4]</sup> Note that the peak observed at  $\sim 0.4 \text{ \AA}^{-1}$  in both perovskite films originates from the Kapton window of the chamber used to hold the samples during measurement.

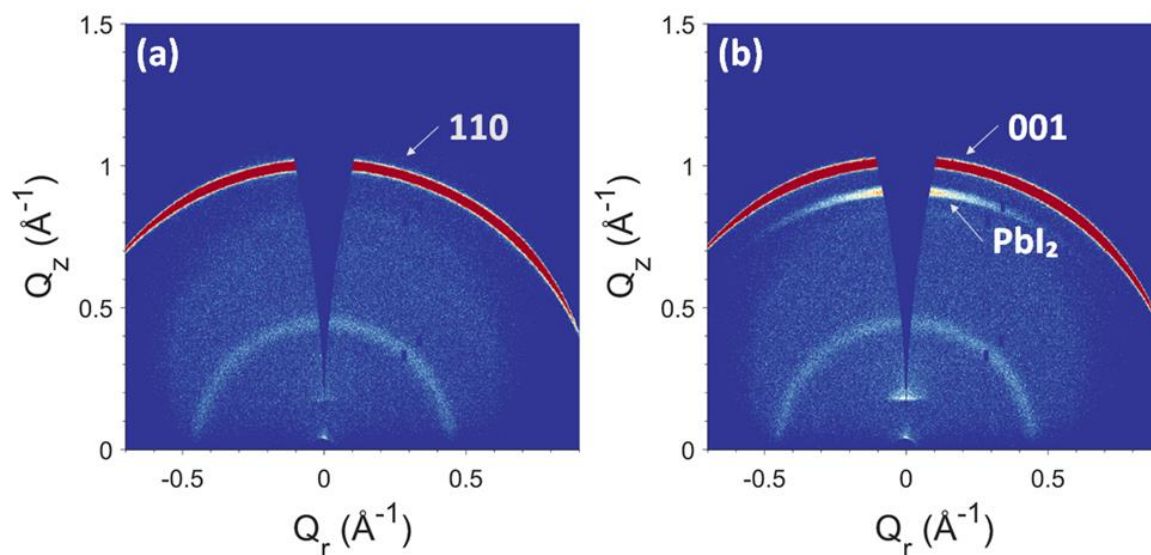


**Figure 7.** GIWAXS of fresh (a) MAPbI<sub>3</sub> film and (b) triple-cation film collected at 2° grazing-incidence angle.

In order to study the degradation of MAPbI<sub>3</sub> and triple-cation, the evolution of the 110 and 001 peaks was monitored for MAPbI<sub>3</sub> and triple-cation perovskite films on ITO/SnO<sub>2</sub> substrates under white light illumination  $200 \pm 10 \text{ mWcm}^{-2}$ , 50 °C, and RH~ 61%. Figure 8(a) and (b) plots the intensity of scattering ( $t = 0$  intensity normalized to 1) as a function of time monitored. A significant change is observed in the MAPbI<sub>3</sub> perovskite phase with a full degradation seen in 50 minutes, with a concomitant growth in the PbI<sub>2</sub> peak (Figure 8 (a)). In contrast the triple-cation film maintained its perovskite phase during testing without any further growth in PbI<sub>2</sub> as shown in Figure 8(b). Figure 8(c) shows a comparison between the relative stability derived from time-evolution of (110) and (001) peaks of MAPbI<sub>3</sub> and triple-cation films. This shows that a non-encapsulated MAPbI<sub>3</sub> film undergoes a rapid degradation under accelerated aging conditions leading to the formation of PbI<sub>2</sub>. As discussed in Chapter 2, this degradation process results from loss of MAI due to heat or via formation of hydrate phases/photo-induced reaction of MAPbI<sub>3</sub> with reactive

oxygen species when exposed to moisture, oxygen and temperature. This results in  $\text{PbI}_2$  becoming the dominant, remaining phase.<sup>[49]</sup>

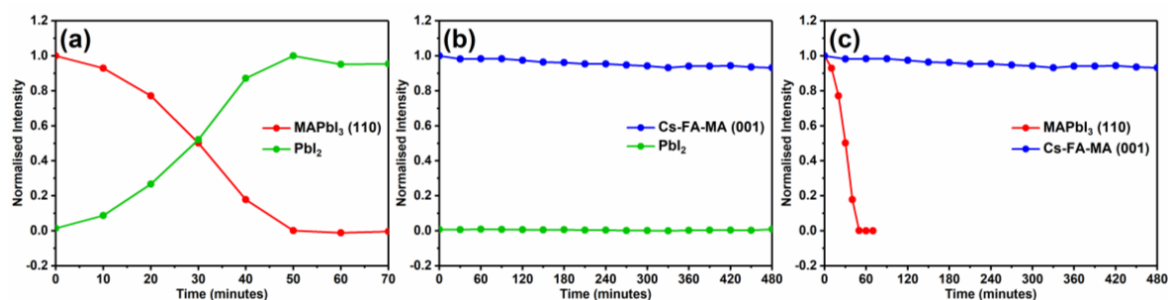


**Figure 8.** Integrated intensity of perovskite and  $\text{PbI}_2$  phases of (a)  $\text{MAPbI}_3$ , (b) triple-cation films, and (c) Stability of  $\text{MAPbI}_3$  and triple-cation perovskite integrated emission intensities when exposed to high humidity and LED light.

In the next section the thin film stability measurements are complemented with operational stability measurements made on fully encapsulated devices including  $\text{MAPbI}_3$  and triple-cation perovskites. Here, devices were tested in ambient air, with a  $J$ - $V$  scan (reverse sweep from 1.2 to 0 V) performed every 4 minutes, with devices held at approximately AM1.5 ( $100 \text{ mWcm}^{-2}$ ) at a temperature of  $(43 \pm 2) \text{ }^\circ\text{C}$  in ambient air (RH 35 - 45%). Device metrics were extracted from the  $J$ - $V$  sweeps and normalised with respect to their initial value at time  $t = 0$ . Figure 9 plots normalised PCE,  $V_{\text{OC}}$ ,  $J_{\text{SC}}$  and FF data recorded for both types of devices over a period of 300 hours. It can be seen that there is the gradual decrease in the PCE of  $\text{MAPbI}_3$  based devices, with the normalised value reducing from 1 at  $t = 0$  to 0.36 over a period of 50 hours, with complete device failure (active layer turned yellow) occurring after 120 hours. Here, the 150 nm  $\text{SiO}_2$  encapsulation used on devices offers a short term protection against degradation caused by moisture and oxygen. However, such thin encapsulation layers are not sufficient to hermetically seal the cells. Thus light and heat induced loss of MAI in form of methylamine gas and iodine vapours are one of

the dominant causes of loss in device performance in MAPbI<sub>3</sub>. In contrast, the triple-cation devices stabilised to 85% of its starting PCE after undergoing a 15% burn-in within first 12 hours. Post burn-in, triple-cation cells demonstrated remarkably stable performance over the duration of this study (288 hours). One of the main reasons for this stable performance is low volatility of FA cations compared to MA, and thus the FAPbI<sub>3</sub> based triple-cation composition has a higher intrinsic stability than MAPbI<sub>3</sub>. This result is in agreement with previous work as discussed in Chapter 2.[19]

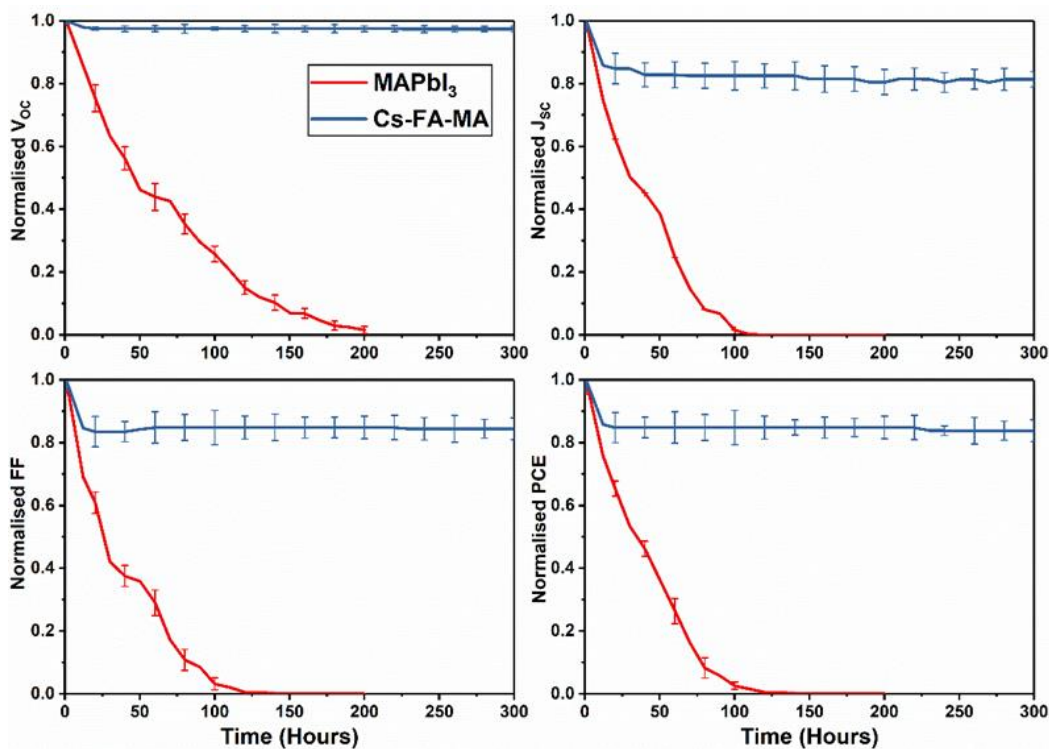


**Figure 9.** Lifetime stability measurements of MAPbI<sub>3</sub> and triple-cation perovskite devices, with data recorded from an average value of at least 8 devices.

#### 4.1.5 Influence of HTL on triple-cation Stability

Due to its multilayer, multi-component architecture, perovskite solar cell device stability depends on several factors including perovskite composition, charge-selective layers and the metal/transparent conducting oxide used for charge

collection. This is because during peak summer times under one sun conditions, the maximum temperature of a perovskite solar cell can reach up to 60 – 80 °C.<sup>[50]</sup> Therefore, it is important to develop material systems for PSC applications that are stable at such temperatures. Stability measurements on perovskite films described in the previous section showed that the triple-cation composition is a thermally stable alternative to MAPbI<sub>3</sub>. Metals oxides, such as titanium dioxide (TiO<sub>2</sub>) and SnO<sub>2</sub> are commonly used as electron transport layers in PSC. These show excellent stability at typical device processing and operating temperatures (up to 100 °C). However, the most efficient hole transport layers used in PSC are polymeric which can show intrinsically limited thermal stability due to low glass transition temperatures. Therefore, in the next section the thermal stability of commonly used hole transport layers in perovskite solar cells is compared.

Here, the relative stability of PSC devices incorporating two different, widely explored HTMs is explored; namely spiro-OMeTAD and PTAA. The device architecture explored was ITO/SnO<sub>2</sub>/triple-cation perovskite/HTL/Au, where the perovskite used was a triple-cation and the HTM was either spiro-OMeTAD or PTAA. The photovoltaic performance of freshly prepared devices is firstly compared using the *J-V* curves of champion devices presented in Figure 10. Here, the spiro-OMeTAD based PSC had a  $V_{oc} = 1.08$  V,  $J_{sc} = 22.32$  mA cm<sup>-2</sup>, FF = 79.31% and PCE = 19.1%. This performance is similar to the champion devices made using a PTAA HTM which demonstrated  $V_{oc} = 1.07$  V,  $J_{sc} = 22.14$  mA cm<sup>-2</sup>, FF = 78.55%, and PCE = 18.6%, with average performance detailed in Table 3. Notably however, PTAA devices demonstrated a higher hysteresis (0.045 compared to 0.017) than spiro-OMeTAD devices, with this effect likely due to possible differences in their hole extraction

rates. Figure 11 shows the statistical distribution of device performance parameters for PSCs utilising spiro-OMeTAD and PTAA as their HTM. PTAA based devices typically had a broader distribution in device performance parameters than spiro-OMeTAD based devices. This is due to difference in the thickness of PTAA (~50 nm) and spiro-OMeTAD (200 nm) required to obtain optimal performance. Since the PTAA thickness is equivalent to the roughness of perovskite film, the possibility to create shunt pathways between top gold electrode and the perovskite are much higher using relatively thin spin coated PTAA layers than when using much thicker spiro-OMeTAD based HTMs.

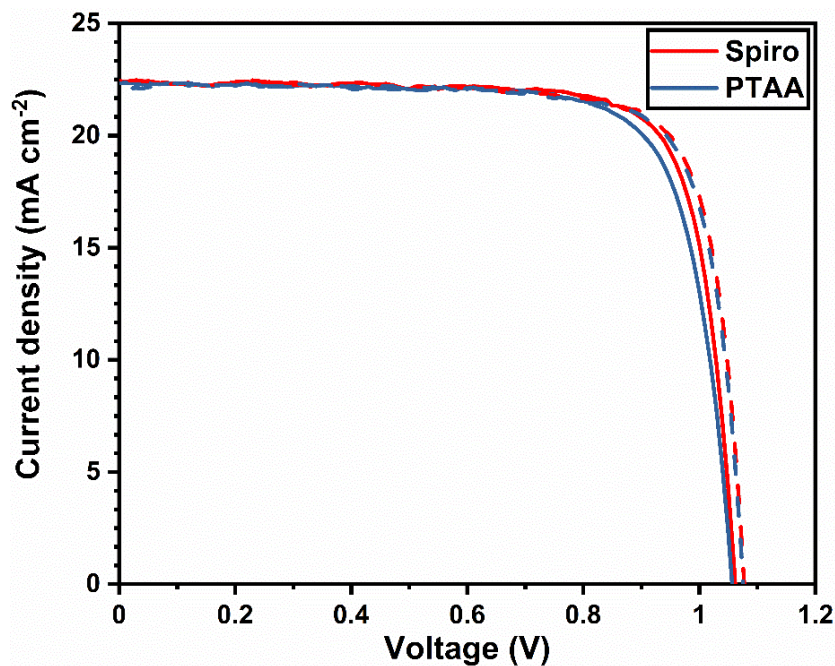


**Figure 10.** *J-V curve of the champion triple-cation perovskite solar cells with spiro-OMeTAD and PTAA as HTLs.*

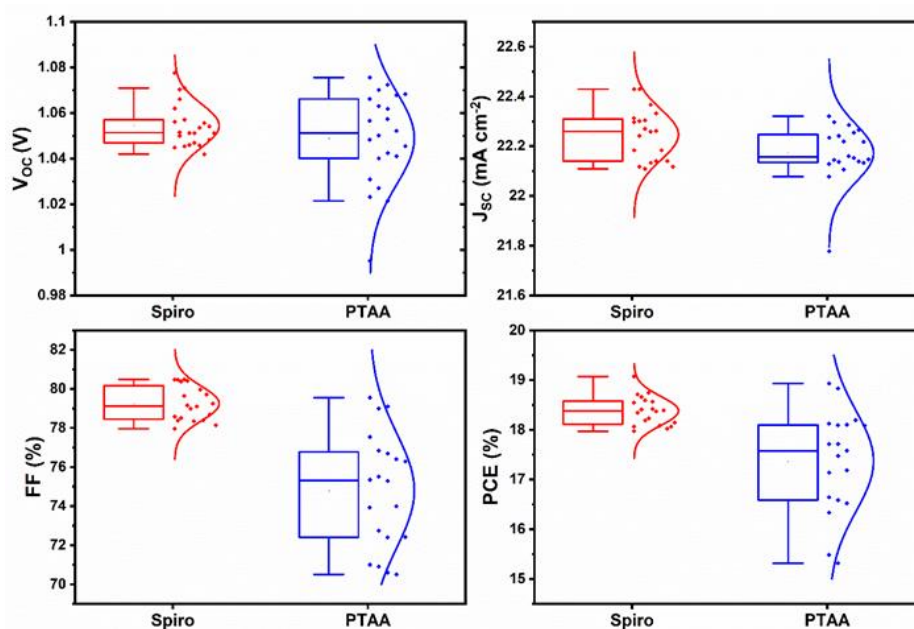


**Figure 11.** Statistical box plots for PSC performance (reverse scan) parameters of PSC using spiro-OMeTAD and PTAA as hole transport materials.

HTL	$V_{oc}$ (V)	$J_{sc}$ ( $mA\ cm^{-2}$ )	FF (%)	PCE (%)
<b>Spiro</b>	<b>1.08 (1.04 ±0.02)</b>	<b>22.32 (22.21 ±0.10)</b>	<b>79.31 (77.25 ±0.88)</b>	<b>19.11 (17.84 ±0.29)</b>
<b>PTAA</b>	<b>1.07 (1.02 ±0.04)</b>	<b>22.14 (21.17 ±0.35)</b>	<b>78.55 (74.80 ±2.92)</b>	<b>18.61 (16.15 ±1.01)</b>

**Table 3.** Summary of reverse scan ( $V_{oc}$  to  $J_{sc}$ ) performance metrics of all devices and the average values from a minimum of 20 cells per testing condition.

To explore device stability, the dark-storage (also called shelf-life) of encapsulated devices was firstly investigated over a period of 30 days. In Figure 12(a), device PCE is plotted as a function of storage time. Here, it is evident that spiro-OMeTAD devices show higher stability under this relatively mild testing condition. A relative drop of 0.7% and 6.6% is observed over 30 days for devices incorporating the spiro-OMeTAD and PTAA HTMs respectively.

It is well known that almost all chemical processes are accelerated by thermal energy, and for this reason many researchers perform testing measurements at

elevated temperature to determine acceleration factors.<sup>[51-53]</sup> Notably such measurements permit activation energies of various degradation mechanisms to be determined using an Arrhenius analysis.<sup>[54]</sup> However such analysis is only valid provided that new degradation processes are not generated by application of elevated temperature – for example phase separation between polymeric materials is one example of a process which might not occur at room temperature, but could be generated when a polymer blend were heated above its glass transition temperature.<sup>[55]</sup> It is therefore important to bear such effects in mind when performing accelerated aging tests.<sup>[56]</sup>

To determine the extent to which applied temperature facilitates device degradation, an experiment was performed in which encapsulated devices based on the two types of HTMs were placed on a hot plate in air at a temperature of 85 °C, with the PCE of such devices being measured every 30 minutes for the first 2 hours, and then every 60 minutes over the course of 8 hours. Typical data for devices incorporating a spiro-OMeTAD and PTAA HTM are shown in Figure 12(b). Here, it is evident that the spiro-OMeTAD devices undergoes an almost catastrophic and rapid failure, whilst the PTAA devices retain around 58% of their initial efficiency after 10 hours. The apparent reversal of device stability at 85 °C indicates that temperature does not accelerating a pre-existing degradation process in the spiro-OMeTAD device, but instead appears to be generating a new degradation pathway.

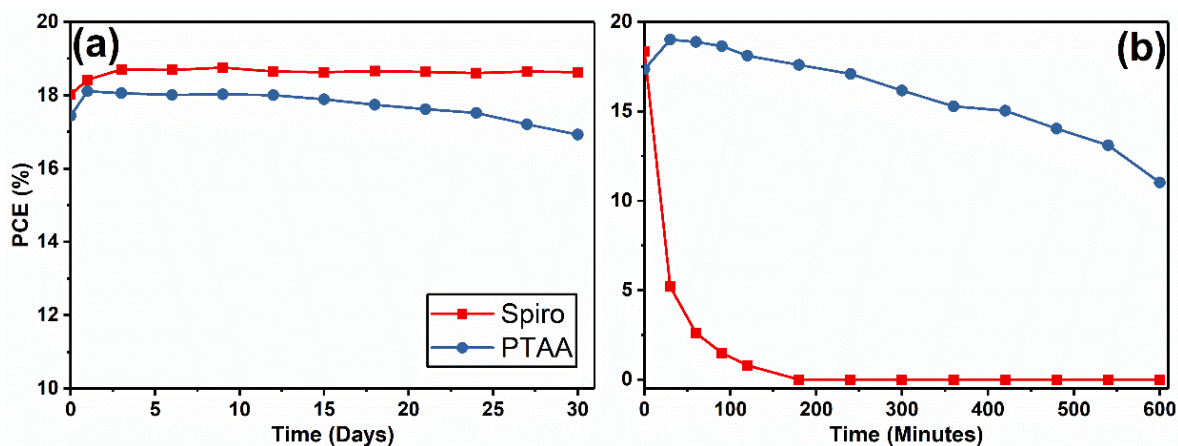


**Figure 12.** (a) Shelf-storage stability and (b) Thermal stability of the triple-cation perovskite with spiro-OMeTAD and PTAA as HTLs.

In Figure 13(a),  $J$ - $V$  curves of devices are plotted that incorporate a freshly prepared spiro-OMeTAD or PTAA layer, together with those from devices that had been annealed at 85 °C for the first 30 minutes. Relevant device metrics extracted from these measurements are shown in Figure 13(b). Here, it is found that the PCE of devices incorporating a spiro-OMeTAD HTM reduces from 18.3% to 4.24% on annealing, while PTAA-based device actually underwent an improvement in efficiency from 15.1% to 17.5%. Although the glass transition temperature of spiro-OMeTAD is around 125 °C,<sup>[57]</sup> the use of dopants such as LiTFSI and tBP further reduces this temperature.<sup>[58]</sup> Additionally, Kim *et al.* showed that the diffusion of iodide ions from the perovskite layer into the spiro-OMeTAD occurred at high temperatures leading to reduction in oxidation and conductivity of spiro-OMeTAD.<sup>[59]</sup> Jena *et al.* observed that annealing a perovskite film, free of spiro-OMeTAD, did not result in significant performance losses. Instead, they attributed PSC degradation under repeat temperature cycles to photo-oxidation and crystallisation of spiro-OMeTAD.<sup>[60]</sup> In addition, the poor thermal stability of perovskite devices may result from the loss of additives from spiro-OMeTAD.<sup>[61]</sup>

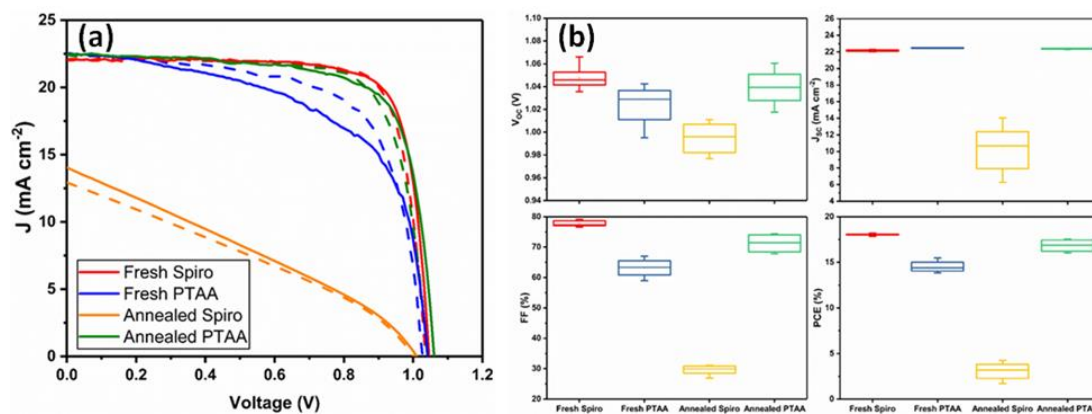


**Figure 13.** *J-V curve and box plots for spiro-OMeTAD and PTAA based devices.*

<i>Device</i>	<i><math>V_{oc}</math> (V)</i>	<i><math>J_{sc}</math> (mA cm<sup>-2</sup>)</i>	<i>FF (%)</i>	<i>PCE (%)</i>
<b>Fresh Spiro</b>	<b>1.05(1.05±0.01)</b>	<b>22.02(21.97±0.05)</b>	<b>78.98(78.35±0.62)</b>	<b>18.26(18.1±0.21)</b>
<b>Fresh PTAA</b>	<b>1.02(1.01±0.02)</b>	<b>22.05(21.99±0.06)</b>	<b>66.97(66.45±0.51)</b>	<b>15.10(14.8±0.59)</b>
<b>Annealed Spiro</b>	<b>1.01(0.99±0.02)</b>	<b>14.04(11.82±2.21)</b>	<b>29.93(24.25±5.72)</b>	<b>4.24(2.84±0.29)</b>
<b>Annealed PTAA</b>	<b>1.06(1.04±0.02)</b>	<b>22.41(22.28±0.02)</b>	<b>73.77(73.35±0.62)</b>	<b>17.52(17±0.24)</b>

**Table 4.** *Summary of reverse scan ( $V_{oc}$  to  $J_{sc}$ ) Performance metrics of all devices.*

Heat induced morphological/compositional changes in organic HTLs affects the recombination dynamics at HTL/perovskite interface. A change in intensity of steady state PL from the perovskite-HTL stack is a good indicator of altered recombination dynamics at this interface. Figure 14 shows the PL spectra of perovskite-HTL stacks incorporating spiro-OMeTAD and PTAA before and after annealing at 85 °C. The peak wavelength of PL emission is unaltered in all cases, which indicates that when thermally annealing in combination with the HTL, a compositional change is not induced in the perovskite layer such as halide segregation.<sup>[62,63]</sup> Notable, the PL intensity from the perovskite-spiro-OMeTAD film is quenched substantially after annealing at 85 °C for 30 min. This indicates that heat induced changes in spiro-OMeTAD increases non-radiative recombination at the

perovskite/spiro-OMeTAD interface, which will in turn cause a reduction in photovoltaic performance parameters - especially in Voc and FF.<sup>[64]</sup> Interestingly, the perovskite-PTAA films emitted increased PL intensity after annealing; a result that is indicative of reduced recombination losses at the PTAA/Perovskite interface. Importantly, the glass transition temperature of PTAA is comparable to spiro-OMeTAD. However, as spiro-OMeTAD is a small molecule HTL, it is able to undergo crystallisation following annealing at temperatures above 85 °C. In contrast, temperature induced long range crystallization does not occur within PTAA due to its macromolecular nature, however annealing can improve electronic-conjugation of the polymeric chains. We suspect that this points to a reduced density of trap states that exist within PTAA and at the perovskite/PTAA interface, leading to lower non-radiative recombination-rates that are observable via an increase in PL emission intensity and improved photovoltaic parameters (especially Voc and FF) in annealed PTAA devices.<sup>[31]</sup>

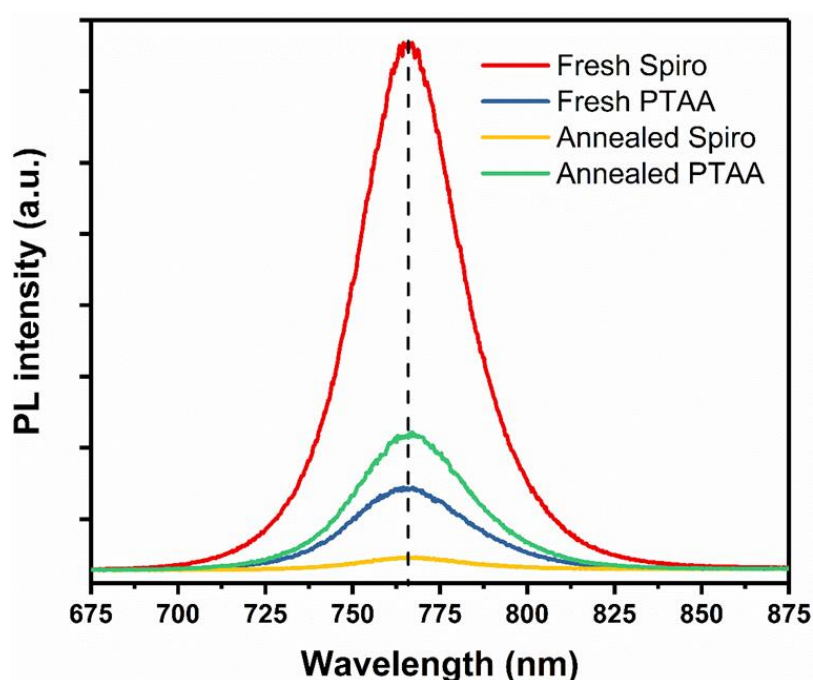


**Figure 14.** Normalised steady-state photoluminescence of fresh and 30 minutes annealed spiro-OMeTAD and PTAA films.

## 4.2 Conclusion

In summary, the effect of composition (MAPbI<sub>3</sub> vs triple-cation) on the stability of *n-i-p* architecture perovskite solar cells (PSCs) was investigated. Triple-cation composition based perovskite films showed high crystallinity, larger grain size and low surface roughness than MAPbI<sub>3</sub>. This led to a superior performance of triple-cation PSCs with a champion PCE of 19.5% as against 16% for MAPbI<sub>3</sub> based PSCs. This improvement in photovoltaic performance parameters of triple-cation PSCs also translated into improved stability of films under several stress factors (moisture, temperature and illumination) for a period of 8 hours. Triple-cation based PSCs demonstrated excellent operational stability with T80 lifetime in excess of 300 hours. In contrast - due to its low intrinsic stability - MAPbI<sub>3</sub> films and associated PSCs underwent accelerated degradation under external stress factors (humidity, heat and illumination).

The role of different HTMs in triple-cation based perovskite solar cells was investigated. It was found that devices with spiro-OMeTAD and PTAA HTM both exhibit high performance, with comparable power conversion efficiencies (19.1% for spiro-OMeTAD vs 18.6% for PTAA). It was observed that both devices have similar shelf stability over a period of 30 days, although PTAA devices had a marginally higher degradation rate. However, triple-cation PSCs with PTAA as HTM showed substantially higher stability towards thermal stress than did spiro-OMeTAD based devices. This suggests PTAA is a better candidate for field applications where cell temperatures can reach up to 60 °C under operational conditions. These results demonstrate that PSC devices incorporating triple-cation perovskite with a PTAA HTM represents a promising combination of materials to

obtain stable operation. Further investigation into the different likely degradation mechanism of HTMs under real-world operational conditions are crucial to achieving high performance and long-term stability.

### 4.3 References

- [1] A. Kojima, K. Teshima, Y. Shirai, T. Miyasaka, *J. Am. Chem. Soc.* **2009**, *131*, 6050.
- [2] M. M. Lee, J. Teuscher, T. Miyasaka, T. N. Murakami, H. J. Snaith, *Science (80-. )*. **2012**, *338*, 643.
- [3] N. J. Jeon, J. H. Noh, Y. C. Kim, W. S. Yang, S. Ryu, S. Il Seok, *Nat. Mater.* **2014**, *13*, 897.
- [4] M. Abdi-Jalebi, Z. Andaji-Garmaroudi, S. Cacovich, C. Stavrakas, B. Philippe, J. M. Richter, M. Alsari, E. P. Booker, E. M. Hutter, A. J. Pearson, S. Lilliu, T. J. Savenije, H. Rensmo, G. Divitini, C. Ducati, R. H. Friend, S. D. Stranks, *Nature* **2018**, *555*, 497.
- [5] NREL, “Best Research-Cell Efficiency Chart,” **2021**.
- [6] S. P. Dunfield, L. Bliss, F. Zhang, J. M. Luther, K. Zhu, M. F. A. M. Hest, M. O. Reese, J. J. Berry, *Adv. Energy Mater.* **2020**, *10*, 1904054.
- [7] J. H. Noh, S. H. Im, J. H. Heo, T. N. Mandal, S. Il Seok, *Nano Lett.* **2013**, *13*, 1764.
- [8] M. Shirayama, M. Kato, T. Miyadera, T. Sugita, T. Fujiseki, S. Hara, H. Kadowaki, D. Murata, M. Chikamatsu, H. Fujiwara, *J. Appl. Phys.* **2016**, *119*, 115501.
- [9] A. F. Akbulatov, S. Y. Luchkin, L. A. Frolova, N. N. Dremova, K. L. Gerasimov, I. S. Zhidkov, D. V. Anokhin, E. Z. Kurmaev, K. J. Stevenson, P. A. Troshin, *J. Phys. Chem. Lett.* **2017**, *8*, 1211.
- [10] W. S. Yang, J. H. Noh, N. J. Jeon, Y. C. Kim, S. Ryu, J. Seo, S. I. Seok, *Science (80-. )*. **2015**, *348*, 1234.
- [11] J.-W. Lee, D.-J. Seol, A.-N. Cho, N.-G. Park, *Adv. Mater.* **2014**, *26*, 4991.
- [12] Y. Yu, C. Wang, C. R. Grice, N. Shrestha, J. Chen, D. Zhao, W. Liao, A. J. Cimaroli, P. J. Roland, R. J. Ellingson, Y. Yan, *ChemSusChem* **2016**, *9*, 3288.
- [13] N. J. Jeon, J. H. Noh, W. S. Yang, Y. C. Kim, S. Ryu, J. Seo, S. Il Seok, *Nature* **2015**, *517*, 476.

- [14] T. Bu, X. Liu, J. Li, W. Li, W. Huang, Z. Ku, Y. Peng, F. Huang, Y.-B. Cheng, J. Zhong, *Electrochim. Acta* **2019**, *306*, 635.
- [15] S. Wang, J. Jin, Y. Qi, P. Liu, Y. Xia, Y. Jiang, R. He, B. Chen, Y. Liu, X. Zhao, *Adv. Funct. Mater.* **2020**, *30*, 1908343.
- [16] A. Amat, E. Mosconi, E. Ronca, C. Quarti, P. Umari, M. K. Nazeeruddin, M. Grätzel, F. De Angelis, *Nano Lett.* **2014**, *14*, 3608.
- [17] J.-W. Lee, D.-H. Kim, H.-S. Kim, S.-W. Seo, S. M. Cho, N.-G. Park, *Adv. Energy Mater.* **2015**, *5*, 1501310.
- [18] W. Qiu, A. Ray, M. Jaysankar, T. Merckx, J. P. Bastos, D. Cheyns, R. Gehlhaar, J. Poortmans, P. Heremans, *Adv. Funct. Mater.* **2017**, *27*, 1700920.
- [19] M. Saliba, T. Matsui, J.-Y. Seo, K. Domanski, J.-P. Correa-Baena, M. K. Nazeeruddin, S. M. Zakeeruddin, W. Tress, A. Abate, A. Hagfeldt, M. Grätzel, *Energy Environ. Sci.* **2016**, *9*, 1989.
- [20] U. Bach, K. De Cloedt, H. Spreitzer, M. Grätzel, *Adv. Mater.* **2000**, *12*, 1060.
- [21] D. Poplavskyy, J. Nelson, *J. Appl. Phys.* **2003**, *93*, 341.
- [22] H. J. Snaith, M. Grätzel, *Appl. Phys. Lett.* **2006**, *89*, 262114.
- [23] H. J. Snaith, A. J. Moule, C. Klein, K. Meerholz, R. H. Friend, M. Grätzel, *Nano Lett.* **2007**, *7*, 3372.
- [24] Y. Liu, Q. Chen, H.-S. Duan, H. Zhou, Y. (Michael) Yang, H. Chen, S. Luo, T.-B. Song, L. Dou, Z. Hong, Y. Yang, *J. Mater. Chem. A* **2015**, *3*, 11940.
- [25] J.-Y. Shao, N. Yang, W. Guo, B.-B. Cui, Q. Chen, Y.-W. Zhong, *Chem. Commun.* **2019**, *55*, 13406.
- [26] Z. Li, C. Xiao, Y. Yang, S. P. Harvey, D. H. Kim, J. A. Christians, M. Yang, P. Schulz, S. U. Nanayakkara, C.-S. Jiang, J. M. Luther, J. J. Berry, M. C. Beard, M. M. Al-Jassim, K. Zhu, *Energy Environ. Sci.* **2017**, *10*, 1234.
- [27] S. N. Habisreutinger, T. Leijtens, G. E. Eperon, S. D. Stranks, R. J. Nicholas, H. J. Snaith, *Nano Lett.* **2014**, *14*, 5561.

- [28] M. Hu, X. Wu, W. L. Tan, B. Tan, A. D. Scully, L. Ding, C. Zhou, Y. Xiong, F. Huang, A. N. Simonov, U. Bach, Y.-B. Cheng, S. Wang, J. Lu, *ACS Appl. Mater. Interfaces* **2020**, *12*, 8260.
- [29] B. Tan, S. R. Raga, A. S. R. Chesman, S. O. Furer, F. Zheng, D. P. McMeekin, L. Jiang, W. Mao, X. Lin, X. Wen, J. Lu, Y. Cheng, U. Bach, *Adv. Energy Mater.* **2019**, *9*, 1901519.
- [30] Z. Shariatnia, *Renew. Sustain. Energy Rev.* **2020**, *119*, 109608.
- [31] M. Saliba, T. Matsui, K. Domanski, J.-Y. Seo, A. Ummadisingu, S. M. Zakeeruddin, J.-P. Correa-Baena, W. R. Tress, A. Abate, A. Hagfeldt, M. Gratzel, *Science (80-. )*. **2016**, *354*, 206.
- [32] T. Matsui, T. Yamamoto, T. Nishihara, R. Morisawa, T. Yokoyama, T. Sekiguchi, T. Negami, *Adv. Mater.* **2019**, *31*, 1806823.
- [33] Y. Bai, Y. Fang, Y. Deng, Q. Wang, J. Zhao, X. Zheng, Y. Zhang, J. Huang, *ChemSusChem* **2016**, *9*, 2686.
- [34] F. Zheng, W. Chen, T. Bu, K. P. Ghiggino, F. Huang, Y. Cheng, P. Tapping, T. W. Kee, B. Jia, X. Wen, *Adv. Energy Mater.* **2019**, *9*, 1901016.
- [35] T. Bu, J. Li, F. Zheng, W. Chen, X. Wen, Z. Ku, Y. Peng, J. Zhong, Y.-B. Cheng, F. Huang, *Nat. Commun.* **2018**, *9*, 4609.
- [36] Y. Hu, M. F. Aygüler, M. L. Petrus, T. Bein, P. Docampo, *ACS Energy Lett.* **2017**, *2*, 2212.
- [37] J. S. Yun, J. Seidel, J. Kim, A. M. Soufiani, S. Huang, J. Lau, N. J. Jeon, S. Il Seok, M. A. Green, A. Ho-Baillie, *Adv. Energy Mater.* **2016**, *6*, 1600330.
- [38] H. Khassaf, S. K. Yadavalli, Y. Zhou, N. P. Padture, A. I. Kingon, *J. Phys. Chem. C* **2019**, *123*, 5321.
- [39] N. Phung, A. Al-Ashouri, S. Meloni, A. Mattoni, S. Albrecht, E. L. Unger, A. Merdasa, A. Abate, *Adv. Energy Mater.* **2020**, *10*, 1903735.
- [40] W. Kong, Z. Ye, Z. Qi, B. Zhang, M. Wang, A. Rahimi-Iman, H. Wu, *Phys. Chem.*

*Chem. Phys.* **2015**, *17*, 16405.

- [41] M. Zhong, Y. Liang, J. Zhang, Z. Wei, Q. Li, D. Xu, *J. Mater. Chem. A* **2019**, *7*, 6659.
- [42] L. Q. Xie, L. Chen, Z. A. Nan, H. X. Lin, T. Wang, D. P. Zhan, J. W. Yan, B. W. Mao, Z. Q. Tian, *J. Am. Chem. Soc.* **2017**, *139*, 3320.
- [43] G. Zheng, C. Zhu, J. Ma, X. Zhang, G. Tang, R. Li, Y. Chen, L. Li, J. Hu, J. Hong, Q. Chen, X. Gao, H. Zhou, *Nat. Commun.* **2018**, *9*, 2793.
- [44] T. Singh, T. Miyasaka, *Adv. Energy Mater.* **2018**, *8*, 1700677.
- [45] X. Zhang, X. Ren, B. Liu, R. Munir, X. Zhu, D. Yang, J. Li, Y. Liu, D.-M. Smilgies, R. Li, Z. Yang, T. Niu, X. Wang, A. Amassian, K. Zhao, S. (Frank) Liu, *Energy Environ. Sci.* **2017**, *10*, 2095.
- [46] M. Ouafi, B. Jaber, L. Atourki, R. Bekkari, L. Laânab, *J. Alloys Compd.* **2018**, *746*, 391.
- [47] D. Barrit, P. Cheng, M. Tang, K. Wang, H. Dang, D. Smilgies, S. (Frank) Liu, T. D. Anthopoulos, K. Zhao, A. Amassian, *Adv. Funct. Mater.* **2019**, *29*, 1807544.
- [48] H. Back, G. Kim, H. Kim, C.-Y. Nam, J. Kim, Y. R. Kim, T. Kim, B. Park, J. R. Durrant, K. Lee, *Energy Environ. Sci.* **2020**, *13*, 840.
- [49] G. Niu, W. Li, F. Meng, L. Wang, H. Dong, Y. Qiu, *J. Mater. Chem. A* **2014**, *2*, 705.
- [50] B. Chen, J. Song, X. Dai, Y. Liu, P. N. Rudd, X. Hong, **2019**, *1902413*, 1.
- [51] J. Kim, N. Park, J. S. Yun, S. Huang, M. A. Green, A. W. Y. Ho-Baillie, *Sol. Energy Mater. Sol. Cells* **2017**, *162*, 41.
- [52] B. Conings, J. Drijkoningen, N. Gauquelin, A. Babayigit, J. D'Haen, L. D'Olieslaeger, A. Ethirajan, J. Verbeeck, J. Manca, E. Mosconi, F. De Angelis, H. G. Boyen, *Adv. Energy Mater.* **2015**, *5*, 1.
- [53] Z. Fan, H. Xiao, Y. Wang, Z. Zhao, Z. Lin, H.-C. Cheng, S.-J. Lee, G. Wang, Z. Feng, W. A. Goddard, Y. Huang, X. Duan, *Joule* **2017**, *1*, 548.
- [54] O. Haillant, D. Dumbleton, A. Zielnik, *Sol. Energy Mater. Sol. Cells* **2011**, *95*,

1889.

- [55] I. Mesquita, L. Andrade, A. Mendes, *ChemSusChem* **2019**, *12*, 2186.
- [56] B. Salhi, Y. S. Wudil, M. K. Hossain, A. Al-Ahmed, F. A. Al-Sulaiman, *Renew. Sustain. Energy Rev.* **2018**, *90*, 210.
- [57] T. Leijtens, I. K. Ding, T. Giovenzana, J. T. Bloking, M. D. McGehee, A. Sellinger, *ACS Nano* **2012**, *6*, 1455.
- [58] T. Malinauskas, D. Tomkute-Luksiene, R. Sens, M. Daskeviciene, R. Send, H. Wonneberger, V. Jankauskas, I. Bruder, V. Getautis, *ACS Appl. Mater. Interfaces* **2015**, *7*, 11107.
- [59] S. Kim, S. Bae, S.-W. Lee, K. Cho, K. D. Lee, H. Kim, S. Park, G. Kwon, S.-W. Ahn, H.-M. Lee, Y. Kang, H.-S. Lee, D. Kim, *Sci. Rep.* **2017**, *7*, 1200.
- [60] A. K. Jena, Y. Numata, M. Ikegami, T. Miyasaka, *J. Mater. Chem. A* **2018**, *6*, 2219.
- [61] H. Zheng, G. Liu, C. Zhang, L. Zhu, A. Alsaedi, T. Hayat, X. Pan, S. Dai, *Sol. Energy* **2018**, *159*, 914.
- [62] Y. Fang, X. Wang, Q. Wang, J. Huang, T. Wu, *Phys. status solidi* **2014**, *211*, 2809.
- [63] Y. Deng, Z. Ni, A. F. Palmstrom, J. Zhao, S. Xu, C. H. Van Brackle, X. Xiao, K. Zhu, J. Huang, *Joule* **2020**, *4*, 1949.
- [64] M. Stolterfoht, P. Caprioglio, C. M. Wolff, J. A. Márquez, J. Nordmann, S. Zhang, D. Rothhardt, U. Hörmann, Y. Amir, A. Redinger, L. Kegelman, F. Zu, S. Albrecht, N. Koch, T. Kirchartz, M. Saliba, T. Unold, D. Neher, *Energy Environ. Sci.* **2019**, *12*, 2778.

# Chapter 5

---

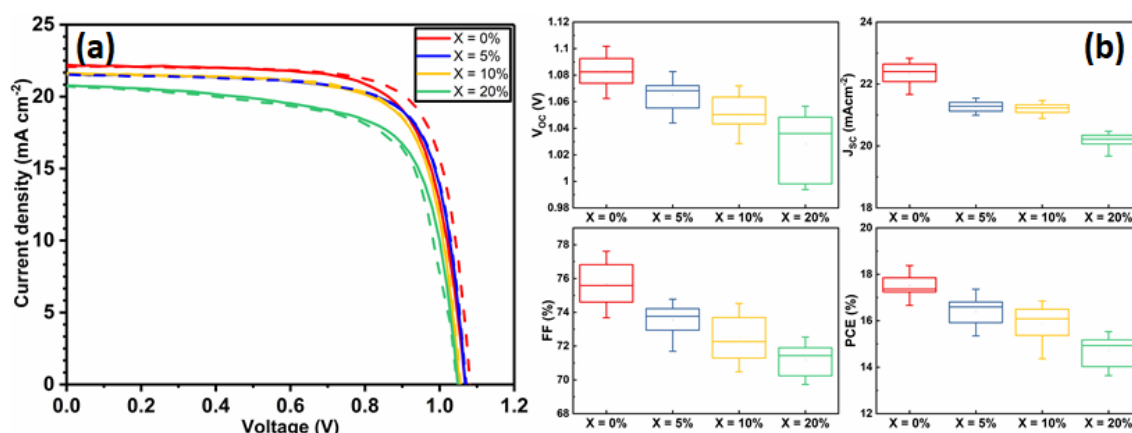
Volume 10, Issue 66

November 06, 2020

40341-40335

## RSC Advances

### Potassium Iodide Reduces the Stability of Triple-Cation Perovskite Solar Cells



For the journals PDF:

DIO: 10.1039/D0RA07107B

Cite this: RSC Adv., 2020, 10, 40341-40350

## 5.0: Motivation of Work

Previous work has been shown that the performance and stability of perovskite solar cells can be enhanced by engineering the composition of the perovskite material itself. One popular material composition is the so-called “triple-cation perovskite”; a material that has been shown to combine both high conversion efficiency and enhanced environmental stability. Interestingly however, it has also been shown that triple-cation performance and stability can be further augmented through the addition of alkali metals.<sup>[1,2]</sup> There are however open questions regarding the origin of this improvement - for example, whether they result from the passivation of defect states within the bulk of the perovskite, or instead occur from passivation of the various interfaces within the active layer. An additional question arises as to whether the addition of such materials result in an improvement in device operational stability. In this chapter, we study the effect of potassium iodide (KI) on the performance and operational stability of triple-cation photovoltaic devices. Here, devices were fabricated using two widely used electron transport layers (ETLs) SnO<sub>2</sub> and TiO<sub>2</sub> and it was found that devices containing the KI additive that utilised an SnO<sub>2</sub> ETL had reduced performance. Furthermore, it was found that devices based on both types of ETL that incorporated KI had reduced stability due to the formation of secondary phases. We suggest that this results from an interaction between KI and bromine ions that formed a non-perovskite phase (KBr) at high KI concentration.

## 5.1: Publication Main Body

### **Potassium iodide reduces the stability of triple-cation perovskite solar cells**

Tarek I. Alanazi<sup>a,b</sup>, Onkar S. Game<sup>a</sup>, Joel A. Smith<sup>a</sup>, Rachel C. Kilbride<sup>a</sup>, Claire Greenland<sup>a</sup>, Rahul Jayaprakash<sup>a</sup>, Kyriacos Georgiou<sup>a</sup>, Nicholas J. Terrill<sup>c</sup> and David G. Lidzey<sup>a\*</sup>

a. Department of Physics and Astronomy, University of Sheffield, Sheffield, S3  
7RH, United Kingdom

Email: [d.g.lidzey@sheffield.ac.uk](mailto:d.g.lidzey@sheffield.ac.uk)

b. Department of Physics, College of Science, Northern Border University,  
Arar, 73222, Kingdom of Saudi Arabia

c. Diamond Light Source Ltd, Harwell Science and Innovation Campus, Fermi  
Ave, Didcot, Oxfordshire, OX11 0DE, United Kingdom

## **Abstract**

The addition of alkali metal halides to hybrid perovskite materials can significantly impact their crystallisation and hence their performance when used in solar cell devices. Previous work on the use of potassium iodide (KI) in active layer to passivate defects in triple-cation mixed-halide perovskites has been shown to enhance their luminescence efficiency and reduce current-voltage hysteresis. However, operational stability of KI passivated perovskite solar cells under ambient conditions remains largely unexplored. By investigating perovskite solar cell performance with SnO<sub>2</sub> or TiO<sub>2</sub> electron transport layers (ETLs), we propose that defect passivation using KI is highly sensitive to the composition of the perovskite-ETL interface. We reconfirm findings from previous reports that KI preferentially interacts with bromide ions in mixed-halide perovskites, and – at concentrations > 5 mol% in the precursor solution - modifies the primary absorber composition as well as leading to the phase segregation of an undesirable secondary non-perovskite phase (KBr) at high KI concentration. Importantly, by studying both material and device stability under continuous illumination and bias under ambient/high-humidity conditions, we show that this secondary phase becomes a favourable degradation product, and that devices incorporating KI have reduced stability.

## **Introduction**

Solution-processed lead halide organic-inorganic perovskites (LHPs) are of significant interest for optoelectronic devices including photovoltaics, light-emitting diodes and radiation sensors.<sup>[3-7]</sup> The success of this class of materials has resulted from their high absorption coefficients, low exciton binding energies, long carrier diffusion lengths and extended carrier lifetimes.<sup>[8-11]</sup> Importantly, LHPs

demonstrate such properties in films deposited from solution that can be processed at temperatures (80 – 150 °C) that are an order of magnitude lower than those required to obtain similar figures of merit using inorganic semiconductors such as GaAs and Si.<sup>[12]</sup> Photovoltaics that first incorporated LHPs were composed of a single cation species. However, such materials commonly exhibit low thermal stability (e.g. methylammonium ( $\text{CH}_3\text{NH}_3^+$  or  $\text{MA}^+$ ) lead iodide ( $\text{MAPbI}_3$ )) or poor structural stability of the pseudo-cubic phase, e.g. formamidinium ( $\text{HC}(\text{NH}_2)_2^+$  or  $\text{FA}^+$ ) lead iodide ( $\text{FAPbI}_3$ ).<sup>[13]</sup> Consequently, mixed-cation ( $\text{Cs}^+$ ,  $\text{MA}^+$ ,  $\text{FA}^+$ ) and mixed-halide ( $\text{I}^-$ ,  $\text{Br}^-$ ) perovskite compositions have been developed to overcome these limitations, and can form thermally stable photo-active black phases at room temperature.<sup>[14]</sup> However, such mixed halide compositions suffer from photo-induced halide segregation and other non-radiative loss mechanisms, resulting in luminescence quantum yields that are often significantly lower than 10%.<sup>[15,16]</sup> In order to address these issues, various passivation strategies have been explored, such as the introduction of polymers or larger cations into the perovskite layer that can improve both luminescence quantum yields and moisture stability.<sup>[17-23]</sup> However, the presence of such macromolecules often impedes charge transport if not managed properly and controlling mixed phase films using larger cations can also compromise device efficiency.

To directly passivate defects in a perovskite, interest has turned to the use of inorganic additives. Saliba *et al.* explored a triple-cation mixed-halide perovskite composition (denoted throughout this paper as ‘TC’) with the addition of rubidium ( $\text{Rb}^+$ ), which showed enhanced device performance in a photovoltaic device.<sup>[24]</sup> Bu *et al.* later used a similar approach with a smaller monovalent alkali metal halide,

potassium ( $K^+$ ).<sup>[25]</sup> Despite the performance enhancement observed, solid-state NMR studies on TCs with  $Rb^+$  and  $MAPbI_3$  with the addition of  $K^+$  demonstrated that such cations are not incorporated into the perovskite lattice, and it was concluded that they underwent segregation, forming secondary phases.<sup>[26]</sup> Recently, Abd-Jalebi *et al.* reported the effectiveness of potassium iodide (KI) as a defect passivating additive in TC perovskites, resulting in materials having a high photoluminescence quantum yield (PLQY) (reportedly up to 66%) and substantially reduced photo-induced halide segregation.<sup>[2]</sup> Indeed, it was proposed that the excess iodide species from KI passivated halide vacancies in the perovskite, while a potassium halide phase resided at the grain boundary region and mitigated photo-induced halide segregation.<sup>[2]</sup>

Despite such very promising findings, there are still questions regarding the origin of the beneficial effects of alkali metal passivation in TCs (for example whether they result from interface or bulk passivation) and whether such additives confer long-term operational stability upon TC photovoltaic devices. Notably, most of the previous reports on KI passivated perovskite solar cells only investigate their shelf life or operational stability under inert environment (See Table S1 Supporting information). However, device stability under real world conditions (i.e. continuous illumination, RH > 30%, temperature > 30 °C) remains unexplored and this forms the basis of our work.

In this manuscript, we first compare the effects of the addition of KI on the optical and microstructural properties of TC and confirm previous findings in the reported literature.<sup>[2,25,27,28]</sup> We then perform focussed investigation into the effect of the addition of KI on material and device stability under ambient/high-humidity

conditions. Specifically we add KI into a TC precursor solution at different concentrations and fabricate planar perovskite solar cells, comparing the performance of devices using electron transport layers (ETLs) formed from a nanoparticle tin oxide ( $\text{SnO}_2$ ) solution with those based on titanium oxide ( $\text{TiO}_2$ ). Our study follows previous work by Abdi-Jalebi *et al.* who observed a monotonic increase in PLQY of TC perovskite on addition of KI at a concentration of up to 40% in the precursor solution, with an optimum performance of PV devices determined at a KI concentration of 10% KI.<sup>[2]</sup> Indeed, we have based our experimental methodology on such previous work and have explored a range of KI concentrations in the TC precursor solution, including 0, 5, 10, and 20 mol%. To understand the effect of the KI addition over this concentration range we use a range of characterisation techniques to understand the influence of KI on the structural, morphological and optical properties of the resultant TC films. We show that for KI additions greater than 5 mol%, phase segregation occurs forming an undesirable secondary non-perovskite phase (KBr). We then perform detailed studies on devices that incorporate either a  $\text{SnO}_2$  or  $\text{TiO}_2$  ETL that explores the effect of KI on modifying their operational stability. We show that the addition of KI has a negative effect on PV performance in devices constructed that use a  $\text{SnO}_2$  ETL, however devices based on a  $\text{TiO}_2$  ETL exhibited improved efficiency at KI concentration of 10%. To explain our findings, we propose that residual potassium hydroxide (KOH) that is used as a stabilising agent in the  $\text{SnO}_2$  colloidal solution already partially passivates this interface. This negates the beneficial effects of the KI, despite resulting in some improvement in device hysteresis. Significantly, we show that the presence of the KI additive is correlated with reduced stability of devices incorporating both  $\text{SnO}_2$  and  $\text{TiO}_2$  ETLs. Our study suggests that the passivating effects of KI in TC perovskites

occur predominantly at the ETL-perovskite interface and is determined by degree to which the interface is already passivated.

## **Results and discussion**

We have investigated the influence of potassium iodide (KI) addition (0 – 20%) on the photovoltaic performance and stability of a triple-cation mixed-halide perovskite with approximate solution composition  $\text{Cs}_{0.05}\text{FA}_{0.79}\text{MA}_{0.15}\text{PbI}_{2.45}\text{Br}_{0.55}$  with an excess of  $\text{PbI}_2$ . Henceforth, we refer to the amount of KI added as the molar fraction (in %) of all cations present in the precursor solution, defined<sup>[23]</sup> as  $X = [\text{K}] / ([\text{K}] + [\text{A}])$  where  $A = (\text{Cs}, \text{FA}, \text{MA})$ . In all cases, the composition and concentrations discussed in the paper refer to the concentration of ions in the precursor solution-phase, and we fully acknowledge that the final composition of such species in the final perovskite film is likely to be slightly different from this due to volatilization during film processing. Furthermore, we emphasize that the concentration range explored here is closely based upon previous work in which a KI concentration of 10% was shown to result in optimum device efficiency.<sup>[2,29]</sup>

### **PV device studies using an $\text{SnO}_2$ ETL**

Devices were fabricated using an n-i-p architecture using a commercially available  $\text{SnO}_2$  nanoparticle solution to fabricate ETLs and spiro-OMeTAD as a hole transport layer (HTL). The structure of the resultant glass/ITO/ $\text{SnO}_2$ /perovskite/spiro-OMeTAD/Au device is shown schematically in Fig. 1.

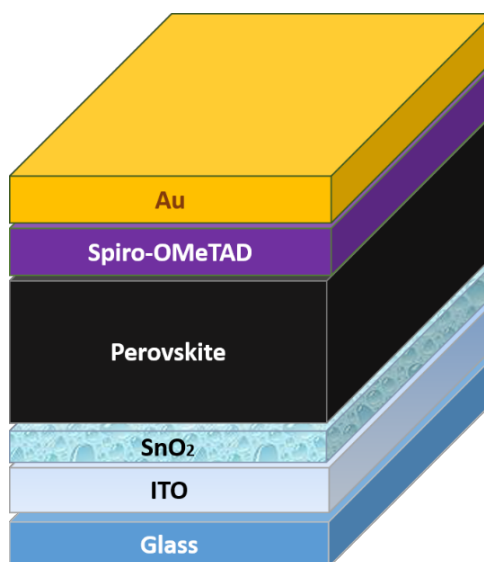


**Figure 1:** Standard architecture (*n-i-p*) triple-cation PSCs having the structure ITO/SnO<sub>2</sub>/perovskite/spiro-OMeTAD/Au.

Current density-voltage (*J-V*) performance for the best devices is shown in Fig. 2(a), with Table S2 tabulating champion device metrics (with average values shown in parenthesis) following the addition of 0, 5, 10 and 20% KI. Notably, the best performing control TC device (having 0% KI) had the highest power conversion efficiency (PCE) of 18.4%, with other device metrics being  $V_{oc}$  1.09 V,  $J_{sc}$  22.07 mA cm<sup>-2</sup> and FF of 76.2%. The forward and reverse scan *J-V* curves were characterised by a degree of hysteresis that has its origin in interfacial charge accumulation and ion migration processes within the perovskite layer.<sup>[30,31]</sup>

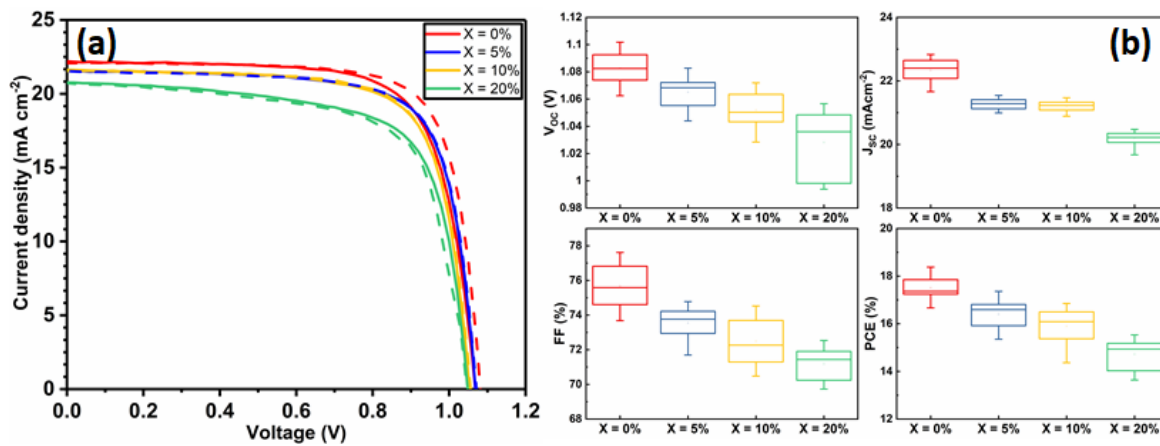


**Figure 2:** (a) Current density-voltage curves for champion devices incorporating the addition of 0, 5, 10 and 20% KI. Forward ( $J_{sc}$  to  $V_{oc}$ ) and reverse ( $V_{oc}$  to  $J_{sc}$ ) sweep directions are indicated by solid and dashed lines respectively. (b) Statistical box plots for PSCs performance (reverse scan  $V_{oc}$  to  $J_{sc}$ ) determined from all devices.

Interestingly, we observe a monotonic decrease in all  $J$ - $V$  performance parameters as the amount of KI is increased in the TC perovskite. Indeed, the open-circuit voltage decreased by  $\sim 10$  mV for each 5% increase in KI concentration. The  $J_{sc}$  and FF also underwent a similar reduction with increasing KI concentration, resulting in an almost linear loss of PCE as shown in Fig. 3.

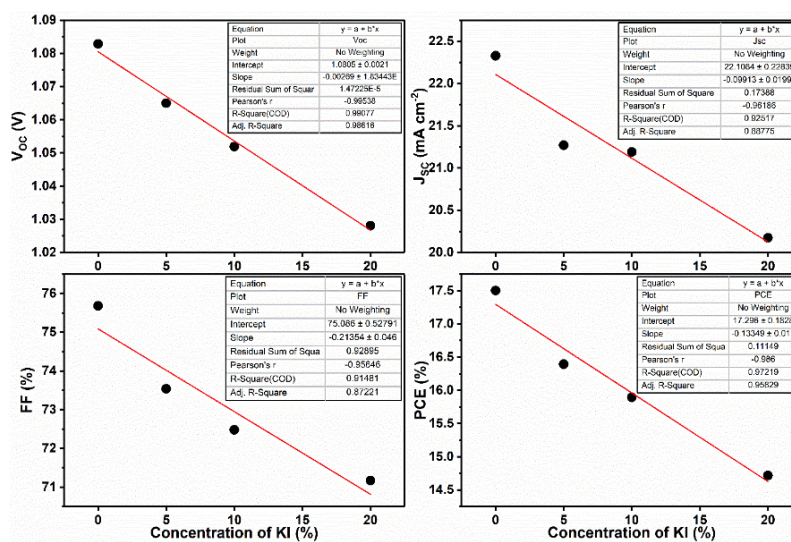


**Figure 3:** Trend in the mean performance metrics of devices as a function of KI concentration.

Statistical box plots of all devices are shown in Fig. 2(b) and confirm the trends observed in champion devices that are shown in Fig. 2(a). These results are in contrast to previous reports of improved performance in PSCs following a similar addition of potassium iodide.<sup>[2,25]</sup> However, we do observe a reduction in  $J$ - $V$  hysteresis in agreement with previous work.<sup>[32,33]</sup> Whilst of limited scientific merit,<sup>[34]</sup> the hysteresis index (HI) can be used to quantify this reduction. Here we find that in our best devices, the HI reduces from 0.06 at 0% KI to 0.004 at 20% KI (see Table S3 for further information).

### **Characterising film structure and crystallinity**

We have investigated the effect of KI addition on film microstructure using scanning electron microscopy (SEM) and atomic force microscopy (AFM). An SEM image recorded from a neat TC film is shown in Fig. 4(a). Here, the film is characterised by polycrystalline grains having a size range of 200 – 600 nm. It is also evident that the film contains regions characterised by excess  $\text{PbI}_2$  that appear as small ( $\sim 50 - 100$  nm) crystallites with brighter contrast than the larger (200 – 600 nm) surrounding perovskite. Fig. 4(a) shows SEM images of perovskite films containing 5, 10 and 20% KI. We find that the addition of 5% KI into the TC perovskite results in a decrease in average grain size from 470 nm (no KI) to 370 nm (5% KI). Interestingly, it appears that the amount of unreacted excess  $\text{PbI}_2$  decreases on addition of KI; a conclusion that is evident from the observed decrease in the fraction of bright  $\text{PbI}_2$  crystallites in Fig. 4(a). As the concentration of KI is increased to 20%, we observe an additional phase (circled yellow in Fig. 4(a)) characterised by a smaller grain structure than is typical for hybrid perovskites. Cross-sectional SEM images of complete devices indicate a similar trend; here ‘neat’ TC films ( $X = 0\%$ ) are predominantly composed

of columnar grains with vertically aligned grain boundaries as shown in Fig. 4(b). This grain structure is likely to facilitate the transport and extraction of photo generated charge carriers from the device. However, the addition of 5 - 10% KI in the precursor solution results in the formation of smaller grains than in the control (0% KI) TC device, as shown in Fig. 4(b). Here, the presence of grain boundaries that are oriented parallel to the device substrate may impede vertical charge transport, as well as increasing the bulk trap density through additional grain boundary recombination centres.<sup>[35-37]</sup> At the highest KI concentration explored (20%), a secondary phase is evident from the distorted microstructure, as can be seen in Fig. 4(b). We note that our observation of reduced perovskite grain size on addition of KI is in contrast to previous work in which it has been shown that the addition of 5% KI into a perovskite precursor slightly increased film crystallinity and grain size.<sup>[25,38,39]</sup>

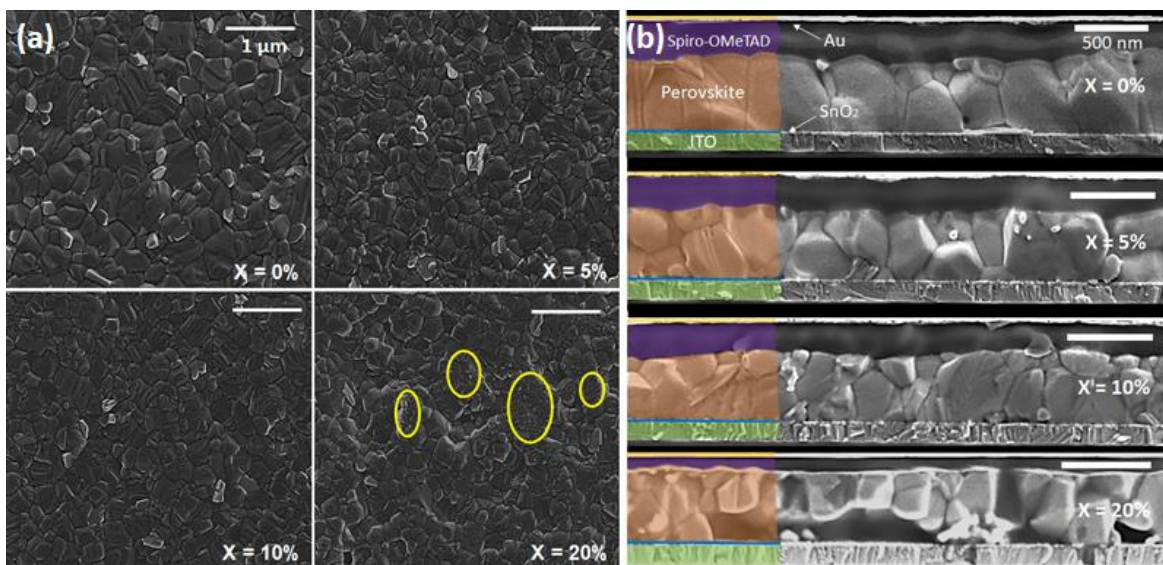


**Figure 4:** (a) SEM of triple-cation perovskite films containing various fractions of KI ( $X = 0, 5, 10$  and  $20\%$  KI). Regions marked in yellow denote the presence of a secondary phase in addition to surrounding TC perovskite grains. (b) Cross-section SEM images of TC perovskite devices;  $X = 0, 5, 10$  and  $20\%$  KI.

Here, we believe that such differences result from the specific nature of the ETL-perovskite interface. Indeed, when using ETLs that are free from alkali metals, the presence of a small amount of  $K^+$  ions in the TC solution can lead to an increase in grain size and improved crystallinity due to altered kinetics of crystallisation and growth.<sup>[40]</sup> However, as the  $K^+$  ion concentration is increased, a decrease in grain size has also been observed.<sup>[40]</sup> This suggests that there likely exists an optimum concentration of  $K^+$  ions at the ETL-perovskite interface or in the TC solution at which an improvement in grain size can be expected. Indeed, we have observed an increase in grain size in films made on mesoporous  $TiO_2$  (mp- $TiO_2$ ) ETLs using a TC precursor containing 10% KI (See Fig. 5). However, the nanoparticle  $SnO_2$  (np- $SnO_2$ ) colloidal solution used to prepare the ETL already contained a quantity of  $K^+$  ions in the form of a KOH stabiliser that was added to the solution by the manufacturer.<sup>[40,41]</sup> Although the exact concentration of the  $K^+$  in the np- $SnO_2$  ETL solution is unknown, we suspect that the addition of even a small quantity ( $\geq 5\%$ ) of KI into the TC precursor solution was sufficient to exceed the “sweet spot” concentration for optimum perovskite grain growth and instead causes a reduction in average perovskite grain size.

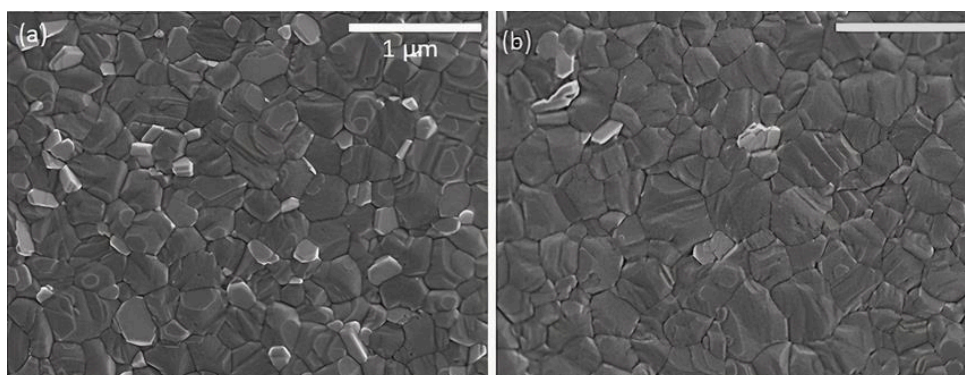


**Figure 5:** SEM images of triple-cation perovskite films on mp- $TiO_2$ ; (a) pristine film and (b)  $X = 10\%$  KI.

We believe that the increased recombination at lateral grain boundaries (in devices containing 5% and 10% KI) together with the presence of secondary non-perovskite phases (in devices containing 20% KI) are significant contributory factors to the observed decrease in the photovoltaic device efficiency.

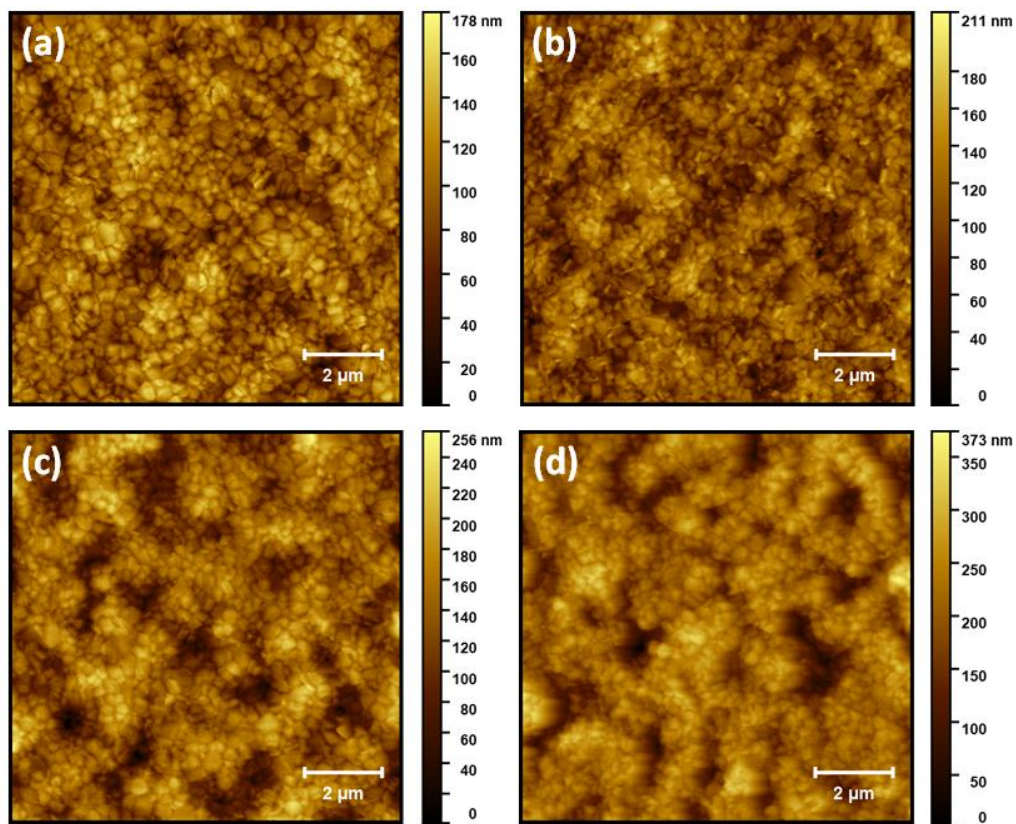


**Figure 6:** AFM images of triple-cation perovskite films; (a) pristine film, and with KI added at different concentrations (b)  $X = 5\%$ , (c)  $X = 10\%$ , and (d)  $X = 20\%$  KI.

Analysis of AFM topographs of corresponding perovskite films (Fig. 6(a - d)) show increased RMS roughness from 22 nm to 46 nm as the KI concentration is increased from 0% to 20% (See Fig. 7 and Table S4). Taken together, these observations indicate that KI modifies nucleation-growth dynamics during the formation of TC perovskite films, most likely indirectly through the presence of  $K^+$  species at the point of crystallisation.

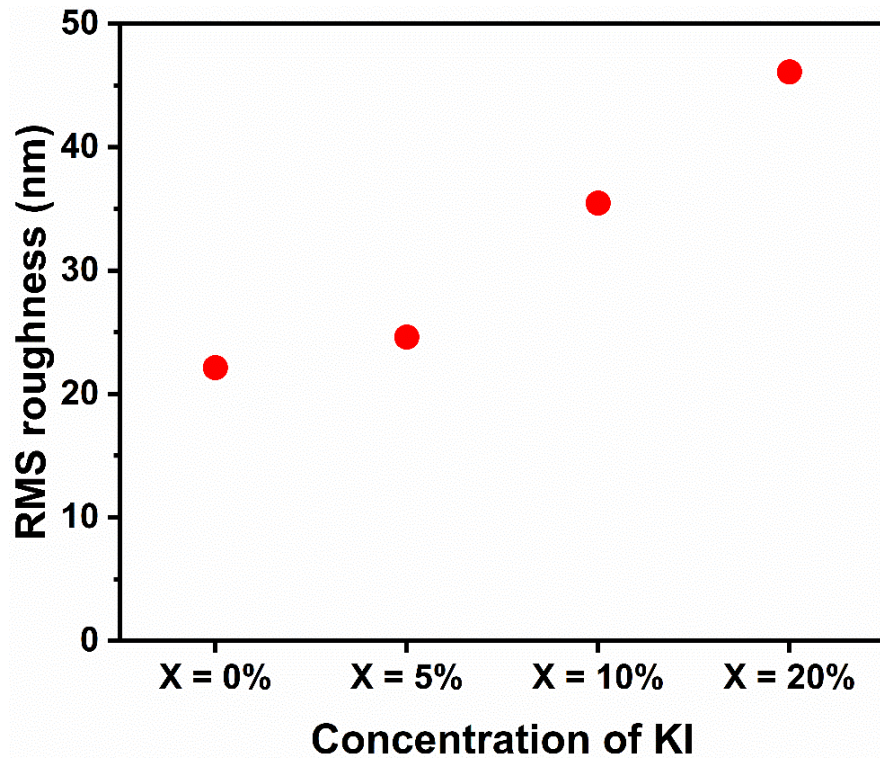


**Figure 7:** Root-mean-square roughness of films increases as KI concentration increases.

In order to understand the effect of KI on the crystallisation of the perovskite phase, we used powder X-ray ( $\text{Cu K}\alpha_{\text{avg}} = 1.5419 \text{ \AA}$ ) diffraction (XRD) and grazing-incidence wide-angle X-ray scattering (GIWAXS) to study films containing different concentrations of KI. In TC composition films without the addition of KI, we observe a diffraction peak at  $2\theta = 12.7^\circ$  which indicates the presence of excess (unreacted)  $\text{PbI}_2$ .<sup>[42]</sup> On addition of KI, a systematic decrease in the intensity of this unreacted  $\text{PbI}_2$  peak is observed in Fig. 8(a) (see also Fig. 8(b)); a finding in agreement with previous reports on potassium passivation.<sup>[29,43]</sup> Fig. 8(c) shows a magnified view of the cubic perovskite (012) scattering peak observed around  $2\theta \sim 31.8^\circ$ . Here, the gradual addition of KI is accompanied by a reduction in the scattering intensity of the (012) peak, together with a shift towards lower  $2\theta$  values. This indicates that the addition of KI results in an increase of the unit cell volume, and a reduction of the

coherent scattering domain size along the axis of measurement ([001]). Alternately it may point towards a reduction of the vertical grain size;<sup>[2]</sup> a conclusion in accord with the grain size analysis performed on the basis of SEM imaging as shown in Fig. 4(a). Note however that the trend of decreased X-ray scattering intensity following the addition of KI is observed in all peaks except for the 20% KI sample, where scattering from the {001} planes show higher intensity. This indicates an altered nucleation and growth due to the addition of KI, resulting in enhanced orientation along the [001] direction. As  $K^+$  has a smaller ionic size (1.38 Å) compared to the other cations in the TC composition ( $FA^+$ : 2.53 Å,  $MA^+$ : 2.17 Å, and  $Cs^+$ : 1.67 Å), the observed increase in lattice size is consistent with an absence of potassium incorporated at cationic sites.<sup>[44,45]</sup>

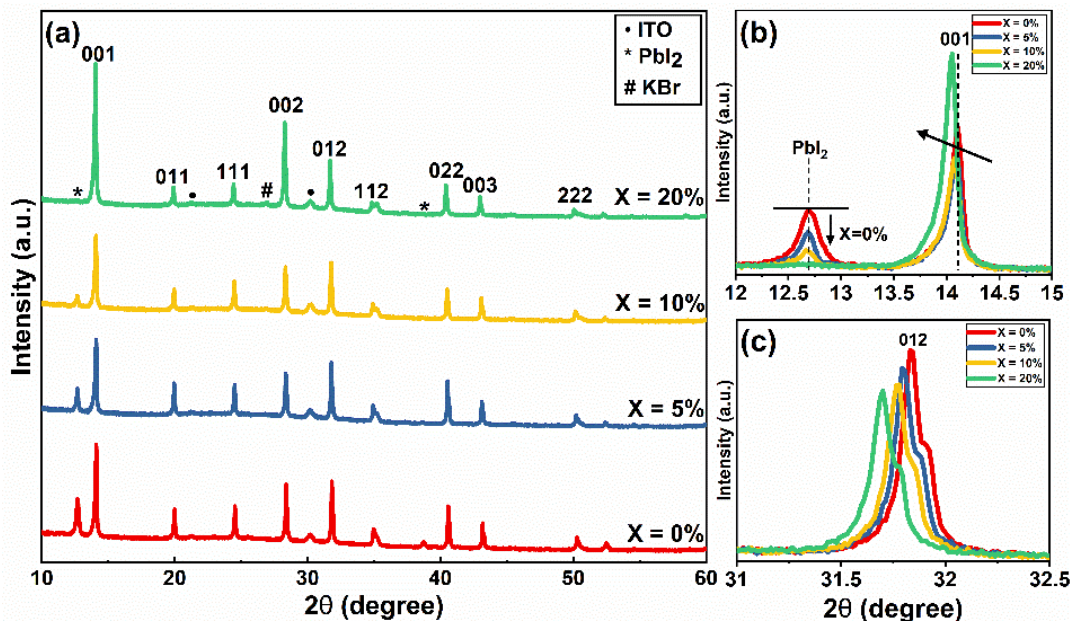


**Figure 8:** (a) XRD patterns of triple-cation perovskite films with different concentration of KI on ITO/SnO<sub>2</sub> (ETL) substrates. (b) Magnified view of XRD patterns of TC (X= 0 – 20%) films to show decrease in Pbl<sub>2</sub> peak intensity around 2θ = 12.7° and (c) variation in (012) peak around 2θ = 31.8° with KI addition.<sup>[48]</sup>

At KI concentrations greater than 5%, we observe scattering features at  $2\theta \sim 27.0^\circ$ ,  $38.6^\circ$ ,  $45.6^\circ$  and  $47.8^\circ$  (See Fig. 9) that are consistent with those expected from cubic KBr (ICDD database; card 00-036-1471).

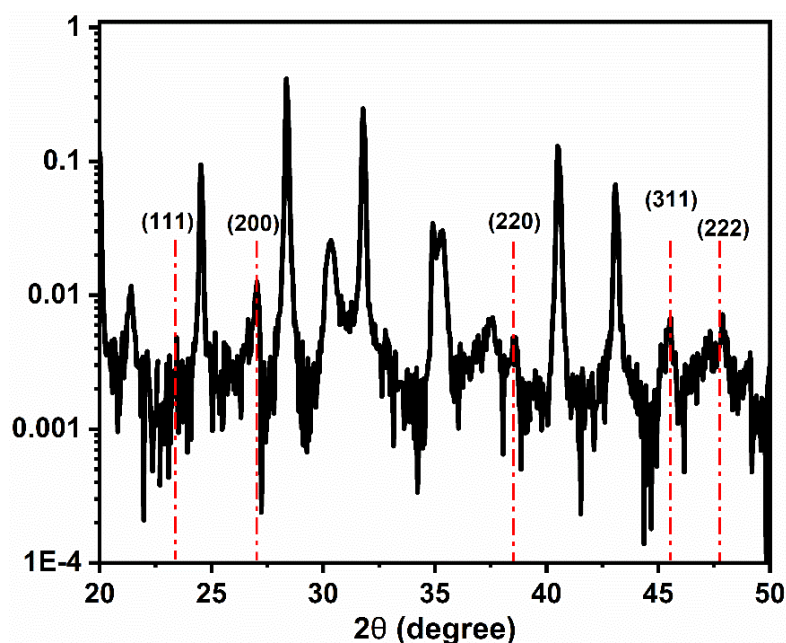


**Figure 9:** Slow XRD scan of 20% KI plotted on log-linear scale. Red vertical lines show the standard position of KBr peaks (ICDD database; card 00-036-1471).

This speculation is also confirmed using GIWAXS for 10% and 20% KI samples as shown in Fig. 10(f) which shows a feature around  $Q \sim 1.9 \text{ \AA}^{-1}$  that corresponds to the (200) reflection of KBr with a  $d$ -spacing of  $3.3 \text{ \AA}$ . This suggests at high concentrations, the  $\text{K}^+$  from KI preferentially interacts with the  $\text{Br}^-$  species in the TC and results in the formation of KBr. Although we have detected the presence of crystalline KBr, we note that previous reports have assigned this additional phase as a K/Br rich phase (e.g.  $\text{K}_2\text{PbI}_4/\text{KBr}_x\text{I}_{1-x}/\text{K}_2\text{PbBr}_4$ ).<sup>[2]</sup> We believe that the composition of secondary phases in TC perovskites generated by the addition of KI, are likely to be dependent on subtle differences in processing conditions. Using GIWAXS we also observe the formation of a secondary phase for 10 and 20% KI *via*

a peak at  $\sim 0.72 \text{ \AA}^{-1}$ , as shown in Fig. 10(a-d); a result consistent with previous observations.<sup>[2]</sup> We believe that this phase could be a potassium lead halide phase (primarily bromide), and indeed the scattering feature at  $\sim 0.72 \text{ \AA}^{-1}$  is coincident with features expected from secondary phases induced by the addition of the larger alkali metal rubidium.<sup>[42,46]</sup> However, we note that this peak is also coincident with a hydrate phase in TC compositions<sup>[47]</sup> observed for devices exposed to moisture during operation, which we discuss later in this paper.

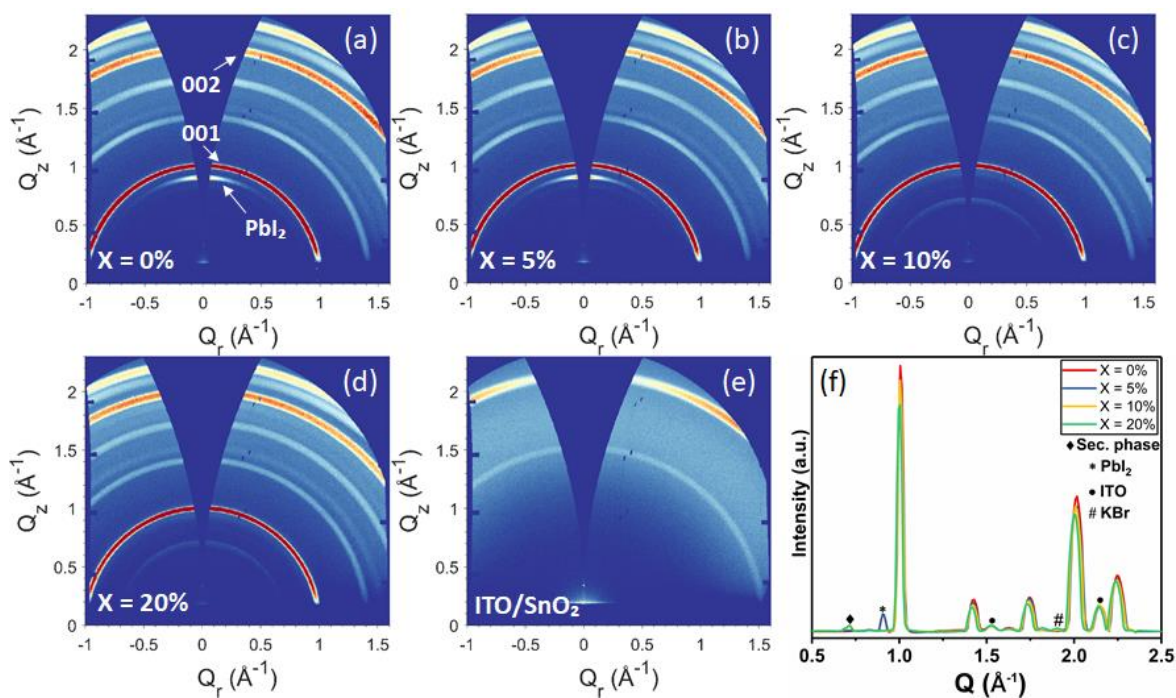


**Figure 10:** (a)-(d) GIWAXS measurements of fresh triple-cation perovskite films collected at  $2^\circ$  grazing incidence angle with different concentration of KI, (e) the diffraction pattern of (amorphous)  $\text{SnO}_2$  on top of (crystalline) ITO and (f) azimuthal integrations of GIWAXS patterns for different concentration of KI.

## Optical Spectroscopy

We have also studied the UV-vis absorption spectra and steady-state photoluminescence (PL) emission of TC films cast with different KI additive concentrations. Fig. 11(a) plots PL emission spectra as a function of KI

concentration. Here, a gradual redshift in the PL emission peak is observed, going from 755 nm in the neat TC film, to 778 nm at 20% KI. The corresponding thin-film absorption spectra are plotted in Fig. 11(b), with a similar redshift in band-edge observed with increasing KI. Although strain induced by a change in lattice parameter could lead to change in band-edge energy, we note that Abdi-Jalebi *et al.* did not observe any shift in the absorption or emission wavelength when incorporating KI into pure-iodide TC perovskites, but using scanning transmission microscopy (with energy dispersive X-ray spectroscopy), potassium and bromine rich clusters were formed near the ETL-perovskite interface.<sup>[2]</sup> Our diffraction and spectroscopic measurements are therefore consistent with the hypothesis that there is preferential co-ordination between  $K^+$  and  $Br^-$  ions in the precursor solution or during crystallisation. This leads to a loss of Br from the perovskite phase as KI is added, thereby depleting the perovskite of  $Br^-$ , with excess iodide from the KI or diminished  $PbI_2$  phase compensating for the loss of bromide. We note that  $I^-$  (2.20 Å) has a larger ionic radius than  $Br^-$  (1.96 Å), therefore a more iodide-rich TC composition is expected to have a larger lattice constant;<sup>[44]</sup> a property commensurate with a reduction in the band gap and explaining the redshift in absorption and emission seen here.

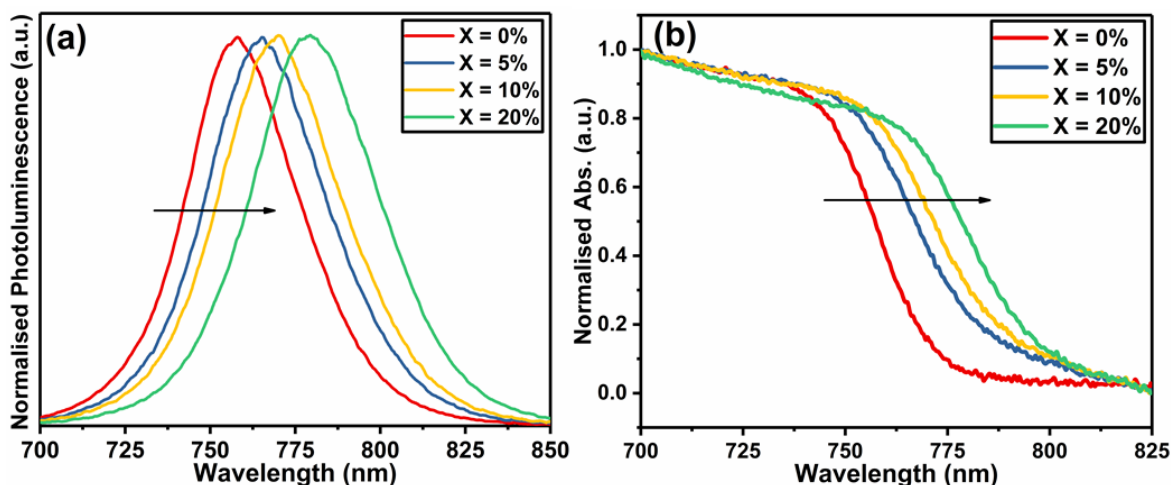


**Figure 11:** Normalised (a) photoluminescence and (b) UV-Vis absorption for triple-cation perovskite films with  $X = 0, 5, 10$  and  $20\%$  KI added.

To understand the interface photophysics of these perovskites, we have investigated their recombination dynamics when deposited on an ITO/SnO<sub>2</sub> electron accepting substrate. In Fig. 12(a), we plot the decay of luminescence following pulsed optical excitation for a series of films to which different concentrations of KI were added to the perovskite precursor. Here, we find a systematic decrease in carrier lifetime as the KI concentration increases, going from 10.8 ns in the neat film, to 8.8 ns in the film prepared from a solution containing an additional 20% KI. This indicates that the presence of potassium does not significantly improve charge carrier extraction when the perovskite is deposited on SnO<sub>2</sub> (which is efficient in all cases); a result in contrast to previous reports on the beneficial effect of potassium passivation.<sup>[25]</sup>

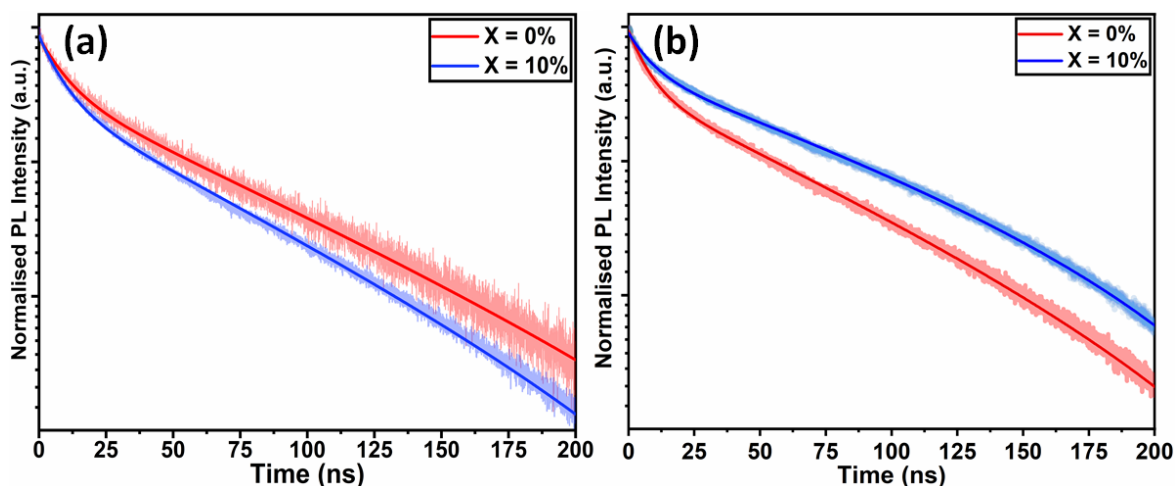


**Figure 12:** Time-resolved photoluminescence of triple-cation perovskite films with KI added at 0 and 10% cast on (a) ITO/SnO<sub>2</sub> and (b) FTO/TiO<sub>2</sub>.

### Effect of ETL on PV devices

To understand the role played by the substrate in our observations, we have fabricated devices with a TiO<sub>2</sub> ETL layer, with the perovskite composed of a TC with an addition of 10% KI. This was compared with a control in which no KI was included. Fig. 13(a) plots  $J$ - $V$  curves and performance metrics for devices based on the architecture FTO/compact (c) -TiO<sub>2</sub>/mp-TiO<sub>2</sub>/perovskite/spiro-OMeTAD/Au, with the perovskite containing either 0% or 10% KI. Interestingly, we find that in devices that use a TiO<sub>2</sub> ETL, there is an improvement in all  $J$ - $V$  metrics with the addition of 10% KI as shown in Fig. 14, with device PCE increasing from 15.2% to 17.5%. A PCE histogram is shown in Fig. 13(b).

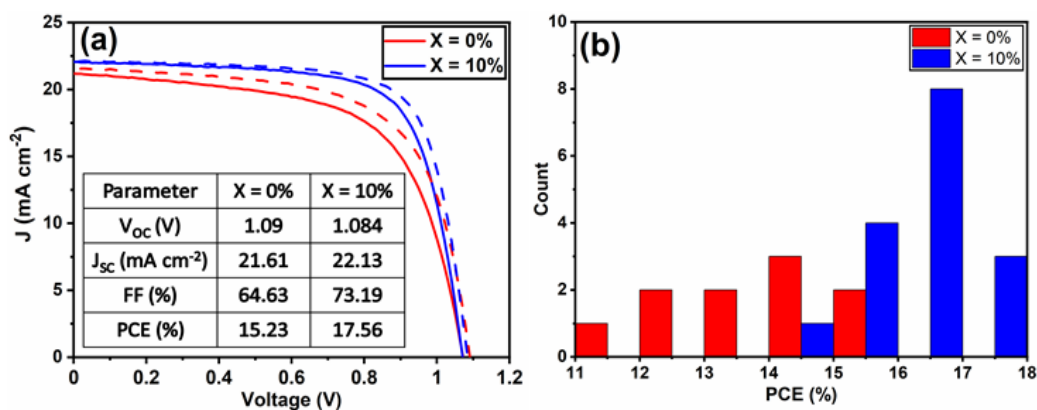


**Figure 13:** (a) J-V curves of champion triple-cation perovskite devices using  $c$ -TiO<sub>2</sub>/mp-TiO<sub>2</sub> as the ETL. (b) A histogram of PCE of all TiO<sub>2</sub> ETL devices from the reverse-scan.

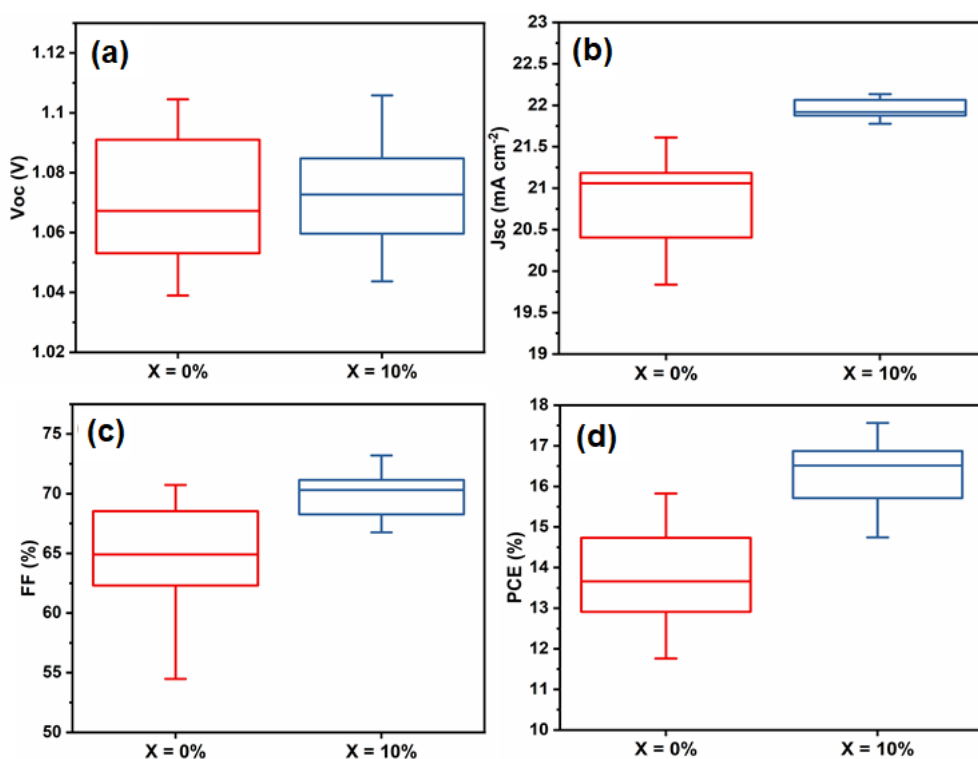


**Figure 14:** Box plots detailing the performance of all TiO<sub>2</sub> ETL devices.

X-ray diffraction measurements and UV-vis absorption (shown in Fig. 15 and 16) demonstrated a similar trend of reduced PbI<sub>2</sub> scattering intensity and a redshift in absorption following the addition of 10% KI to the perovskite. Importantly, the 10% KI perovskite deposited on TiO<sub>2</sub> was also characterised by an enhanced carrier

lifetime compared to the neat TC case (see Fig. 12(b)); a result in accord with that of Abdi-Jalebi *et al.*<sup>[2]</sup> This suggests that the precise nature of the ETL-perovskite interface before passivation plays a significant role in determining the benefit of potassium ion passivation.

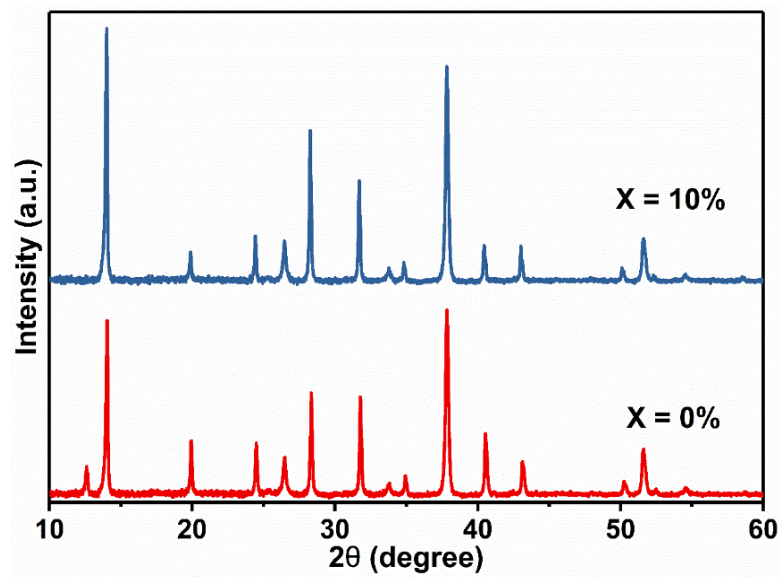


**Figure 15:** XRD patterns of triple-cation perovskite films cast on  $\text{TiO}_2$  substrates from precursor solutions having initial KI concentrations of 0 and 10%.

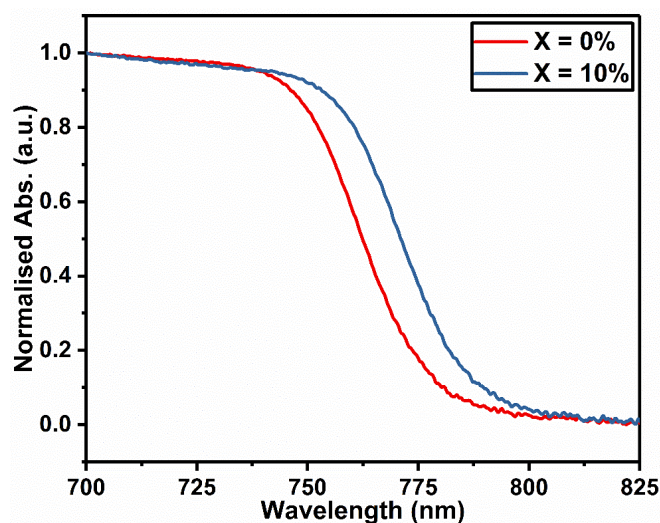


**Figure 16:** UV-Vis absorption spectra of triple-cation perovskite films cast on *c*- $\text{TiO}_2$ /*m*- $\text{TiO}_2$  substrates from a precursor solution having initial KI concentrations of 0 and 10%.

To form the SnO<sub>2</sub> ETL in our n-i-p devices, we used a colloidal SnO<sub>2</sub> solution in H<sub>2</sub>O that included potassium hydroxide (KOH) as a stabilising agent.<sup>[49]</sup> We suspect therefore that the ETL/perovskite interface formed from this material was already ‘moderately’ passivated by the potassium species. Significantly, Bu *et al.* have shown that carrier lifetime can be reduced by removing potassium ions from this SnO<sub>2</sub> surface; an effect accompanied by impaired device performance.<sup>[40]</sup> Interestingly, KOH treatment of a water-washed SnO<sub>2</sub> layer restored the device performance parameters. Bu *et al.* have also demonstrated that TC perovskite devices based on SnO<sub>2</sub> layers (processed by chemical bath deposition from a SnCl<sub>2</sub>.2H<sub>2</sub>O solution) could be passivated by ~ 3.5 mol% K<sup>+</sup> in the perovskite solution.<sup>[25]</sup> We therefore suggest that, the beneficial effects of KI addition are dependent on the unpassivated interface quality. Here the KI that is added to TC films made on intrinsically passivated SnO<sub>2</sub> ETLs likely remains in the bulk of perovskite film, forming secondary phases such as KBr. Such interfaces between the perovskite and KBr or other non-perovskite phases may increase the bulk trap density, leading to increased non-radiative recombination, or otherwise hinder charge transfer from the perovskite to the ETL as evidenced in Fig. 12(a). We believe that this scenario explains the observed negative trend in photovoltaic performance parameters on addition of KI to TC perovskite devices made with np-SnO<sub>2</sub>. As mp-TiO<sub>2</sub> has a high interfacial surface area, it is likely to be characterised by a higher density of trap states than a SnO<sub>2</sub> ETL. Here, the addition of KI to the TC is expected to passivate traps at the mp-TiO<sub>2</sub>/perovskite interface and thereby improve the performance of devices as observed on addition of 10% KI to the TC. We conclude therefore that the

net effect (positive or negative) of the addition of KI to the TC on solar cell performance depends on the extent to which it passivates the ETL-perovskite interface *and/or* generates increased recombination due to the formation of secondary phases within the bulk.

### **Stability of devices on addition of KI**

Several factors are likely to contribute to the stability of a perovskite solar cell device. These include intrinsic effects (such as the perovskite phase or composition), together with extrinsic factors (such as exposure to moisture, light and oxygen). Other factors that affect device stability include whether (or not) it is run close to its open-circuit voltage or allowed to generate a current by being held at short-circuit. The relative stability of both the ETL and HTL materials used in a device is also important, and this is often dependent on the glass transition temperature of the material. The reactivity and diffusivity of the metal electrode and other dopants or ions can also affect device operational stability. It is therefore important to identify the dominant degradation pathway(s) in a PSC to understand processes that limit its stability. We note that both intrinsic and extrinsic degradation processes can be studied in thin films prepared on representative substrates, while degradation in devices can best be studied *in operando*.

To characterise intrinsic material stability, we first performed *in situ* GIWAXS measurements on the triple cation perovskite films deposited on a quartz substrate (0% and 10% KI) to identify intrinsic/extrinsic degradation pathways under accelerated stress conditions. These measurements were performed at the I22 beamline using synchrotron-generated X-rays at the Diamond Light Source. In these experiments, an environmental chamber was integrated into the beamline, allowing

us to control temperature, humidity and light-levels. This permitted us to monitor the loss of crystallinity of the perovskite phase during film stressing, with typical 2D X-ray scattering patterns shown in Fig. 17. Full experimental details are given in the methods section.

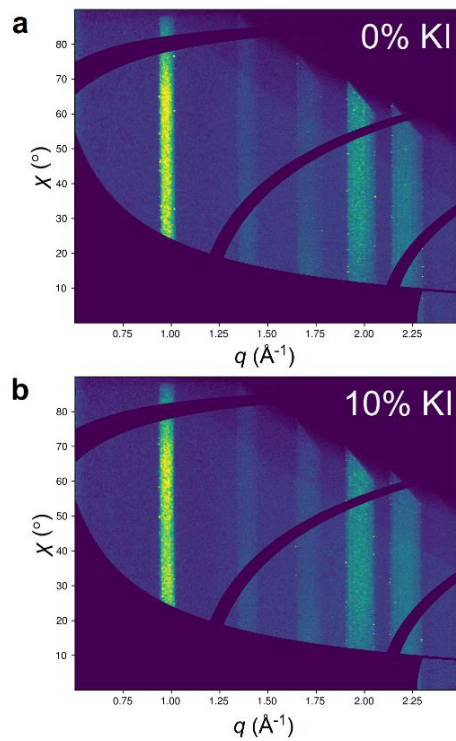


**Figure 17:** Typical remapped 2D scattering patterns for the 0% KI and 10% KI samples as recorded prior to accelerated aging conditions. Data are plotted as  $\chi$  (azimuthal scattering angle) vs.  $q$  (momentum transfer) with the perovskite (001) reflection observed at  $q \approx 1.0 \text{ \AA}^{-1}$ . For in-situ degradation studies, integrated scatter from this reflection was monitored, with background subtraction.

We first investigated intense damp heat conditions, with high humidity and samples held on a hotplate at either 120 °C or 150 °C, combined with white light illumination controlled to  $\sim 2$  suns intensity. In Fig. 18 we show that at 150 °C the integrated scattering intensity from the perovskite (001) reflection decreases rapidly to under 20% after 5-8 minutes for both samples. At 120 °C the loss of intensity is more

gradual, with the initial scatter reducing to 50% after 17 min for the 10% KI sample and around 30 min for the 0% KI sample.

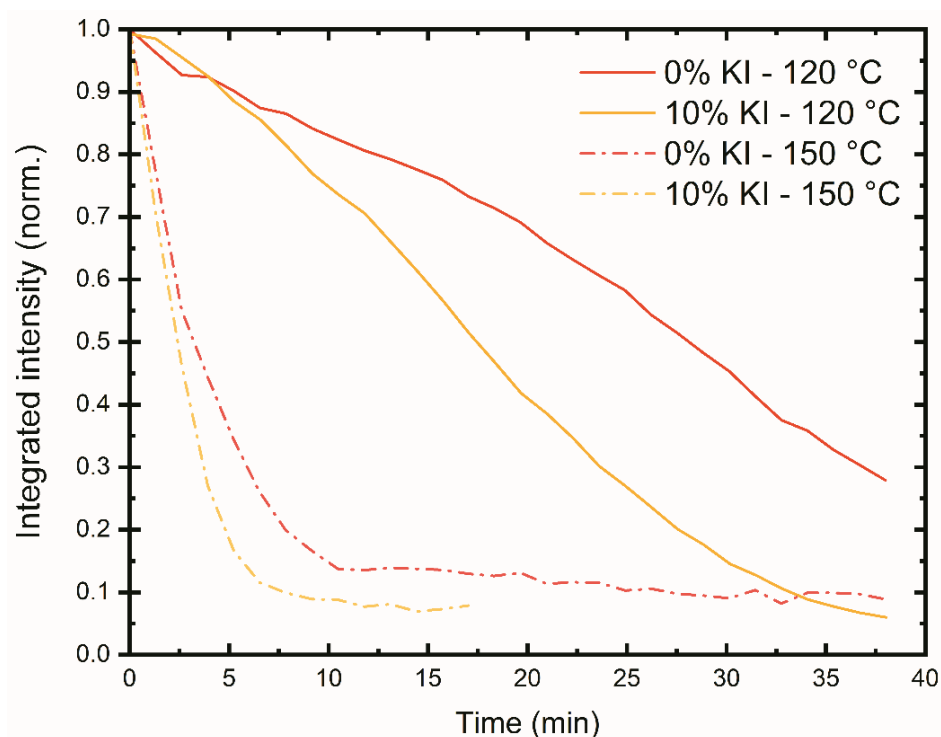


**Figure 18:** Monitoring the reduction of perovskite crystallinity under accelerated aging conditions using integrated scatter from the (001) reflection for 0% KI (red) and 10% KI (yellow) samples. Films were placed in a sample chamber with a hotplate temperature of either 120 °C (solid lines) or 150 °C (dashed). The measured air temperature ( $T_{air}$ ) and relative humidity (RH) for each experiment was  $T_{air} = 59 \pm 3$  °C,  $62 \pm 1$  °C,  $70 \pm 2$  °C,  $69 \pm 4$  °C and  $RH = 33 \pm 4\%$ ,  $26 \pm 1\%$ ,  $19 \pm 1\%$ ,  $19 \pm 3\%$  for 0% KI, 10% KI at 120 °C and 0% KI, 10% KI at 150 °C, respectively.

We next investigated reduction in scattering intensity of the perovskite phase over an extended period with films on a hotplate set to 43 °C and high humidity conditions (Fig. 19). Again, we observed the same material stability trend, with around 95% of the 0% KI perovskite scattering intensity being retained after 8 hours, whereas the scattering intensity from 10% KI sample had reduced to just under 85% over the same period (although we note small variations in chamber

conditions). Taken together, these observations indicate that the 10% KI film has reduced material stability under accelerated damp heat degradation conditions. We suspect that the origin of such instability results from chemical reactions that occur between the perovskite and water which lead to the formation of hydrates and (in case of 10% KI) secondary phases such as KBr.<sup>[29]</sup> Indeed, Wang *et al.*<sup>[50]</sup> have demonstrated that moisture induced degradation in polycrystalline perovskite films initially occurs at grain boundaries, with this degradation then propagating through the film in an in-plane direction. This suggests that morphological differences in perovskite films (such as reduced grain size) can in fact facilitate moisture induced degradation processes as observed in films produced from 10% KI TC solutions.

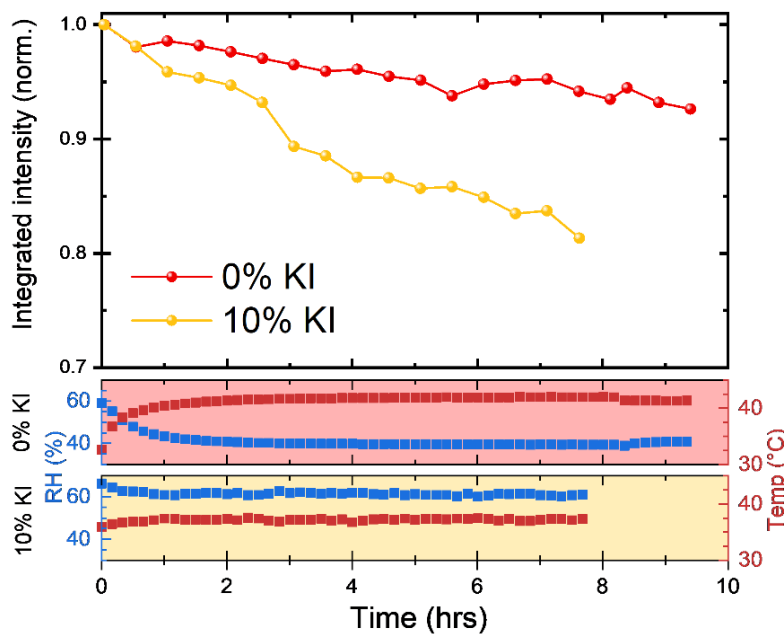


**Figure 19:** Long-term stability of 0% KI and 10% KI films under accelerated aging conditions. Scattering intensity from the (001) reflection was monitored with films kept on a 43 °C hotplate with  $T_{air}$  and RH monitored. Note, that we recorded small differences in chamber conditions between each measurement run, with average  $T_{air} \approx 41$  °C and  $RH \approx 41\%$  for 0% KI and  $T_{air} \approx 37$  °C and  $RH \approx 61\%$  for 10% KI as shown in the lower panels, corresponding to absolute humidities of  $22 \text{ gm}^{-3}$  and  $27 \text{ gm}^{-3}$ , respectively.

We have also investigated the effect of adding KI to the perovskite composition on the long-term operational stability of perovskite solar cells. Here, stability measurements were performed in ambient air at a relative humidity of 35 - 45% and at a temperature of  $(42 \pm 3)$  °C (induced by the illumination light source). In order to partially limit degradation processes to intrinsic mechanisms, devices were encapsulated using a 100 nm thick layer of SiO<sub>2</sub> layer to suppress the ingress of moisture and oxygen. During measurement, reverse sweep *J-V* curves were recorded approximately every four minutes, with devices being held at *V*<sub>oc</sub> at other times. Fig. 20(a) shows the temporal evolution of device PCE under continuous illumination for SnO<sub>2</sub>-based PSCs. Here, the control cells underwent a drop of 25% compared to the initial performance over the first 50 hours of measurement, with the devices then stabilising to 72% of their initial performance after 500 hours of continuous testing. However, devices that included excess KI had reduced stability, with their PCE undergoing a progressive decrease during testing. We have also observed similar trends of reduced operational stability in 10% KI TC perovskite solar cells fabricated using a TiO<sub>2</sub> ETL (see Fig. 20(b)). This contrasts with control devices (0% KI) on TiO<sub>2</sub> that exhibit similar stability to TC (0% KI) devices fabricated on SnO<sub>2</sub>. To understand this instability, we prepared devices without SiO<sub>2</sub> encapsulation and aged them for 50 hours under the same conditions; a result that showed the same trend of reduced stability with increasing KI concentration (see Fig. 21).

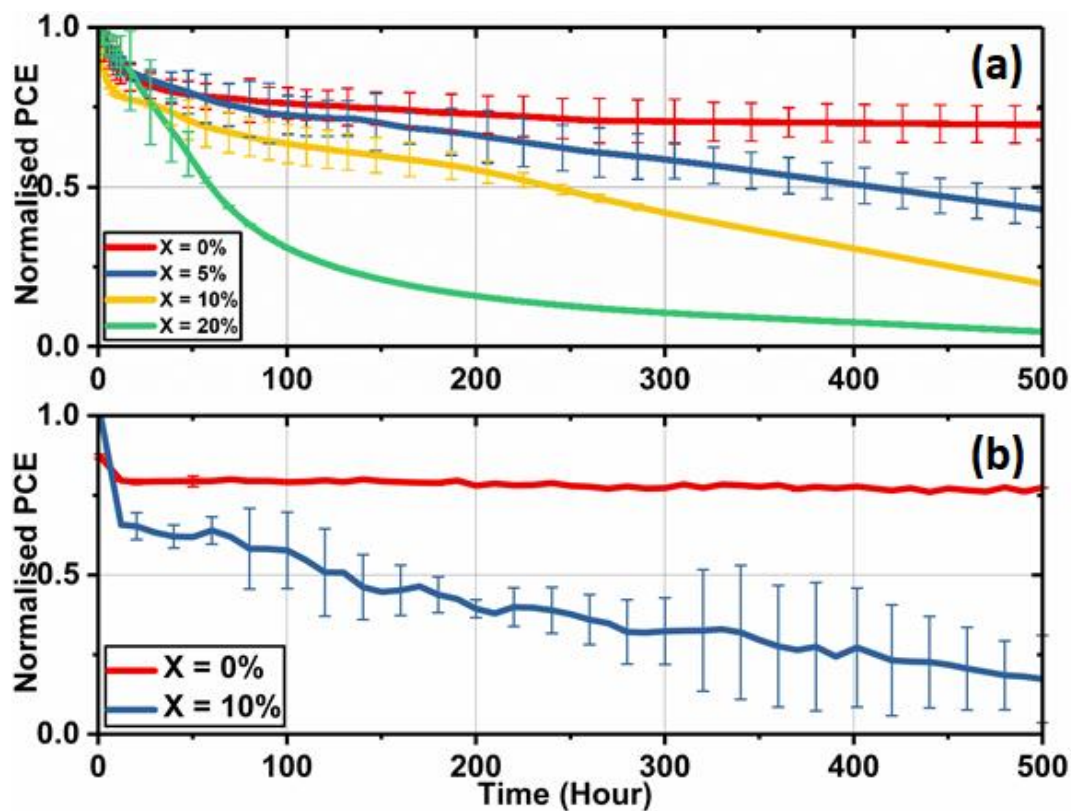


**Figure 20:** Lifetime stability measurements of triple-cation perovskite devices created from precursor solutions with various levels of KI addition cast on (a) SnO<sub>2</sub> with data presented from an average value of a minimum of 6 devices, and (b) TiO<sub>2</sub> having an initial KI concentration of 0 and 10% from an average value of 6 cells.

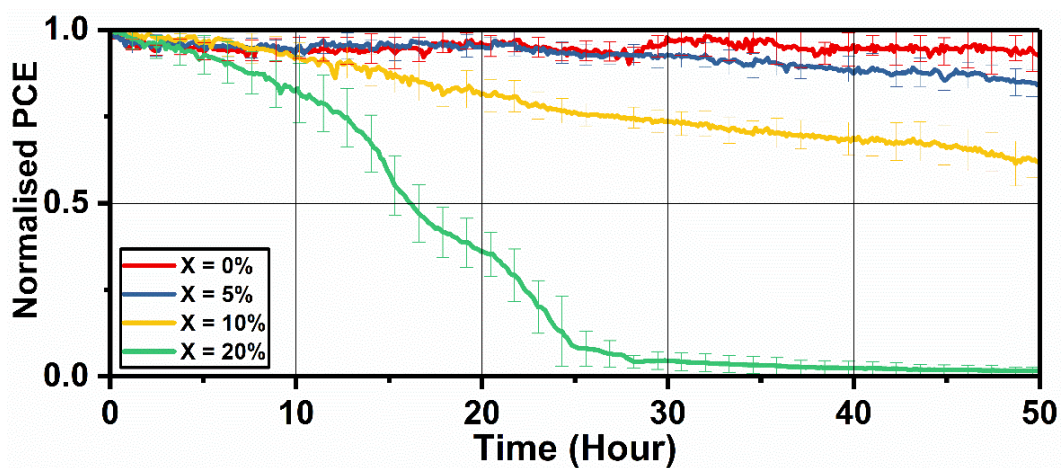


**Figure 21:** Stability of unencapsulated perovskite devices with different concentration of KI added to the precursor solution. Curves were constructed from data taken from a minimum of 2 devices.

We then recorded GIWAXS measurements on the degraded perovskite layers by removing both the Au contact and the spiro-OMeTAD layer. Fig. 22(a) and (b) show the 2D diffraction patterns from TC films having KI added at 0% and 10%, with the same patterns for 5% and 20% KI films shown in Fig. 23 (along with azimuthally integrated diffraction patterns for all four samples). We find that the degraded TC film with 0% KI is characterised by a  $\text{PbI}_2$  peak ( $\sim 0.9 \text{ \AA}^{-1}$ ), which is oriented in the out-of-plane ( $Q_z$ ) direction, and is present to a lesser extent at increasing KI concentrations; a result consistent with the undegraded samples (Fig. 10).

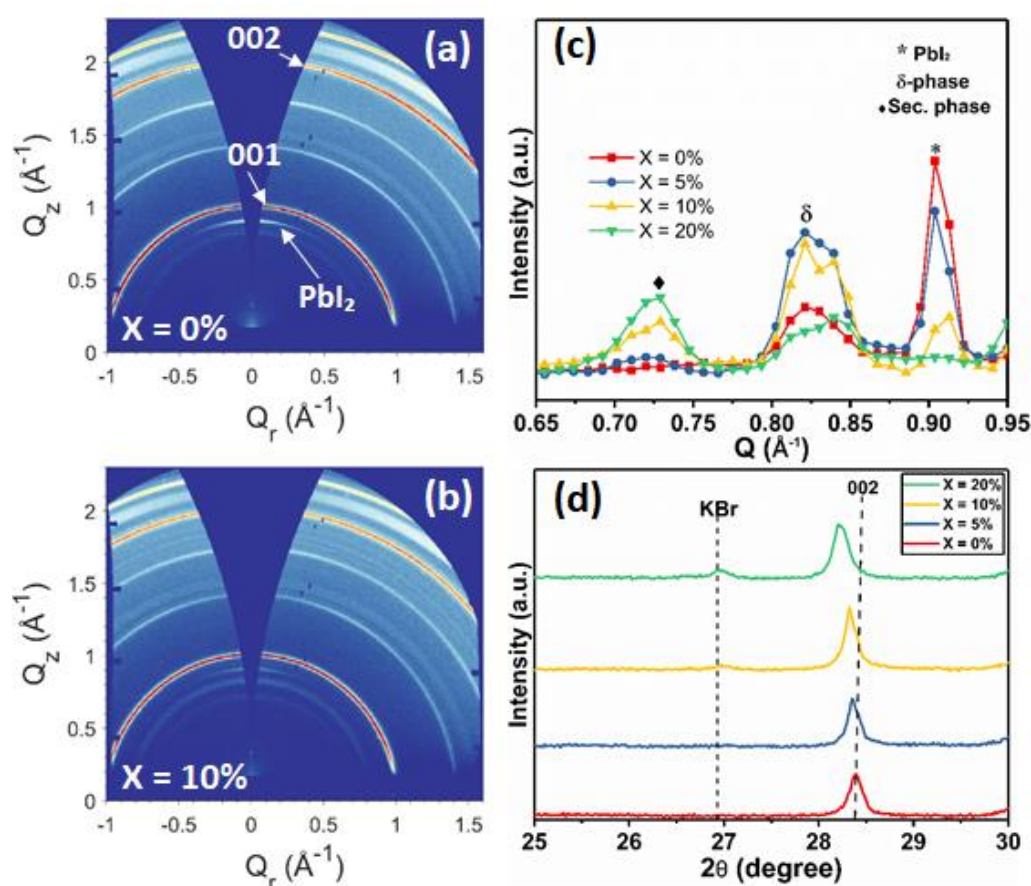


**Figure 22:** GIWAXS diffraction patterns of aged triple-cation perovskite films with (a) 0% KI and (b) 10% KI. (c) Azimuthally integrated profiles from GIWAXS patterns recorded from aged devices (see text for details), highlighting degradation products formed in the region  $0.65 \leq Q \leq 0.95 \text{ \AA}^{-1}$ . (d) XRD patterns from degraded films confirming KBr is still present for 10% and 20% KI addition.

Isotropic scattering rings are also apparent at  $\sim 0.81\text{-}0.84 \text{ \AA}^{-1}$  in both devices, and for all films incorporating KI at  $\sim 0.72 \text{ \AA}^{-1}$ , with Fig. 22(c) highlighting the phases present in the degraded films for each composition.

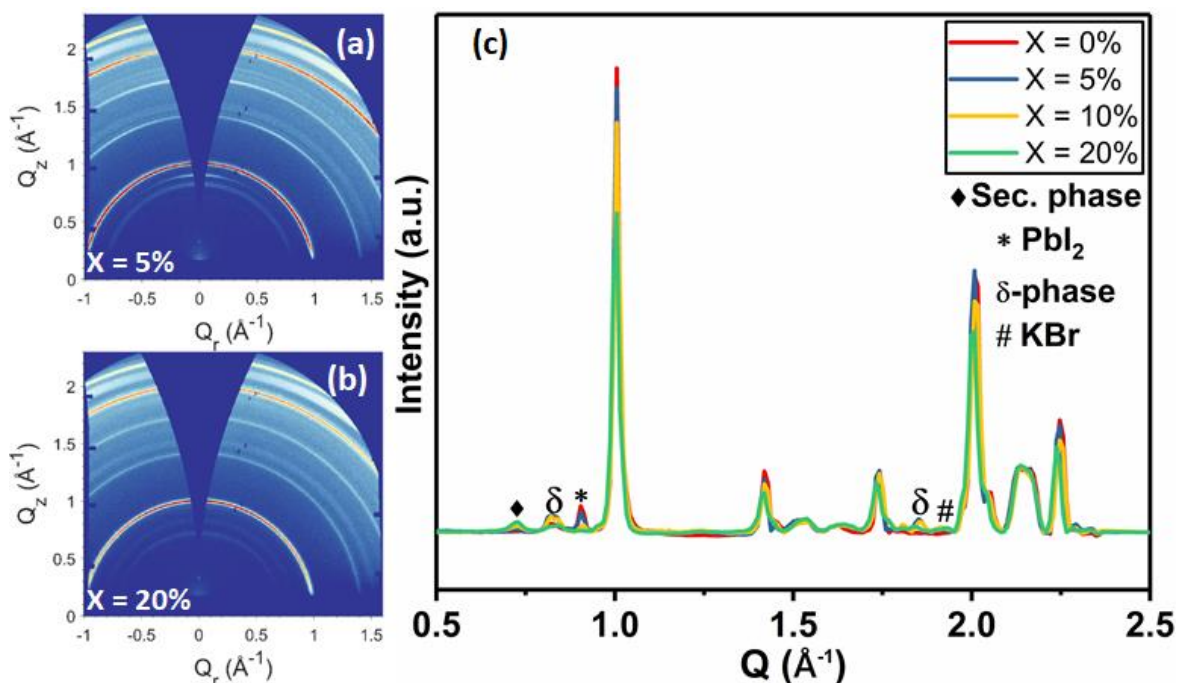


**Figure 23:** GIWAXS of films taken from aged devices, with the perovskite films prepared from precursors containing KI at a concentration of (a)  $X = 5\%$  and (b)  $X = 20\%$ . Part (c) shows an azimuthal integration of the GIWAXS pattern from an aged device recorded over profile  $0.5 \leq Q \leq 2.5 \text{ \AA}^{-1}$ .

Here, the peak at  $0.72 \text{ \AA}^{-1}$  is ascribed to a secondary or hydrate phase (as observed in the undegraded 10% and 20% KI films) with its intensity being approximately proportional to the additive concentration. The broad feature at  $\sim 0.82 \text{ \AA}^{-1}$  is attributed to a  $\delta$ -phase, or more precisely, scattering from the (100) plane of the 2H or 4H hexagonal polytype of the perovskite phase,<sup>[51]</sup> which is expected to have peaks in the range  $0.81 \leq Q \leq 0.85 \text{ \AA}^{-1}$ .<sup>[46,52]</sup> This is confirmed by two features correlated in intensity with peaks at  $\sim 0.82 \text{ \AA}^{-1}$  at  $1.81 \text{ \AA}^{-1}$  and with greater intensity at  $1.85 \text{ \AA}^{-1}$ , with the latter corresponding well with expected peak positions of either

the (202) plane of the 2H polytype or (201) plane of the 4H polytype (see Fig. 24).<sup>[51]</sup>

This phase is present to some extent in all films, but is highest in the 5% and 10% KI samples.

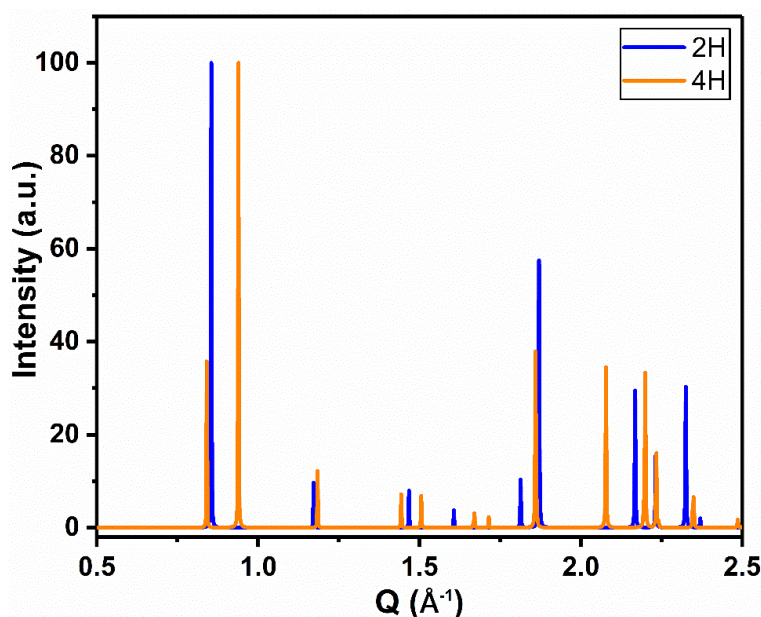


**Figure 24:** Simulated XRD of 2H and 4H polytypes of FAPbI<sub>3</sub>.

Our stability measurements indicate that 20% KI cells undergo critical failure after around 30 hours, whereas the 5% and 10% KI devices declined in efficiency linearly over the testing period (see Fig. 21). One of the possible origins of the rapid degradation of 20% KI cells could be complete conversion of the perovskite phase to other photo-inactive phases such as  $\delta$ -FAPbI<sub>3</sub> (2H polytype) or other secondary phases such as KBr or hydrates. We can in fact rule out this mechanism using the XRD measurements shown in Fig. 25 and UV-vis absorbance shown in Fig. 26.

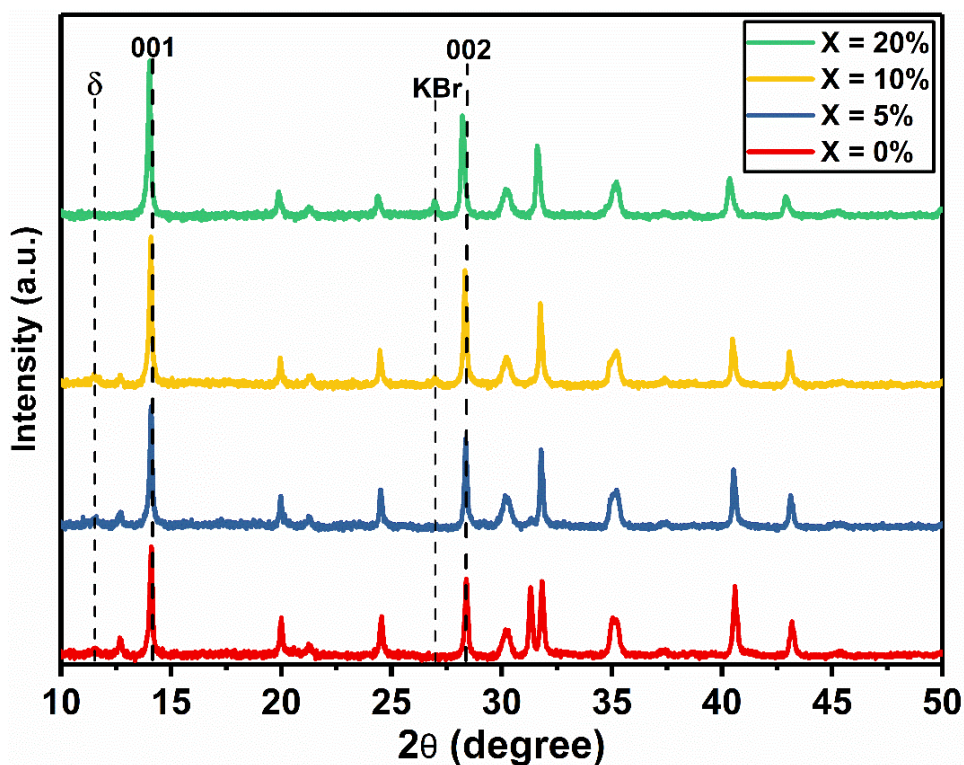


**Figure 25:** XRD patterns of aged triple-cation perovskite devices containing different concentrations of KI added to the precursor.

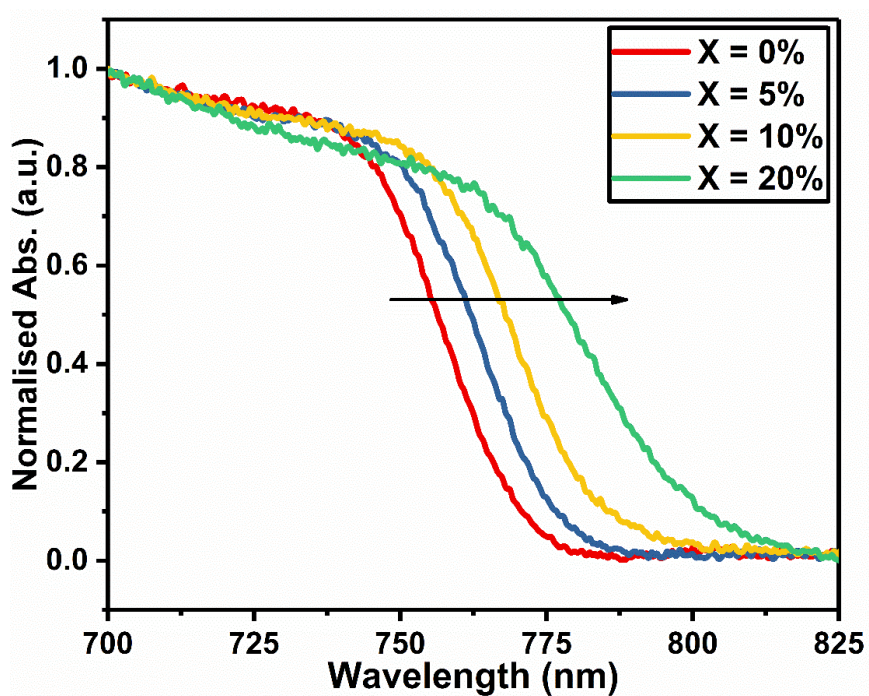


**Figure 26:** Normalised UV-Vis absorption for aged triple-cation perovskite films with X = 0, 5, 10 and 20%.

Here, our measurements indicate the retention of perovskite phase in aged TC devices for all KI compositions. Interestingly, we observe that the device containing a TC with 20% KI undergoes a red-shift in both its absorption and PL emission (780 nm for fresh device vs. 800 nm for the aged device (see Fig. 27(b) and (c)). This process is accompanied by the shift of XRD peaks to lower  $2\theta$  values, indicating a further increase in the unit cell volume. This suggests that under operational conditions (light illumination and voltage) there is a further loss of bromide ( $\text{Br}^-$ ) ions from the TC composition, resulting in an additional formation of KBr. This conclusion is further supported by XRD measurements on the aged device where a small increase in intensity of the KBr peak at  $2\theta \sim 27^\circ$  is observed (see Fig. 27(a) and 9(d)). We note that Zheng *et al.* demonstrated a similar formation of KBr-like compounds under illumination using confocal fluorescence microscopy and STEM-EDX mapping studies on perovskite films containing an addition of KI (3.5%).<sup>[53]</sup> Importantly, STEM-EDX elemental mapping results indicated the formation of KBr around the top of the TC film (at the TC/spiro-OMeTAD interface). We suggest this illumination process induces excessive formation of KBr in devices containing a high (20%) KI content. This is likely to lead to increased recombination and may impede charge transport at perovskite-ETL/HTL interfaces, leading to a rapid, critical failure of such devices. It is also apparent that the continual loss in performance of devices containing 5% and 10% KI also suggests that under operational conditions, the perovskite is less phase stable; indeed the formation of KBr and consequent removal of Br from the perovskite phase apparently results in a greater phase instability to the  $\delta$ -phase.

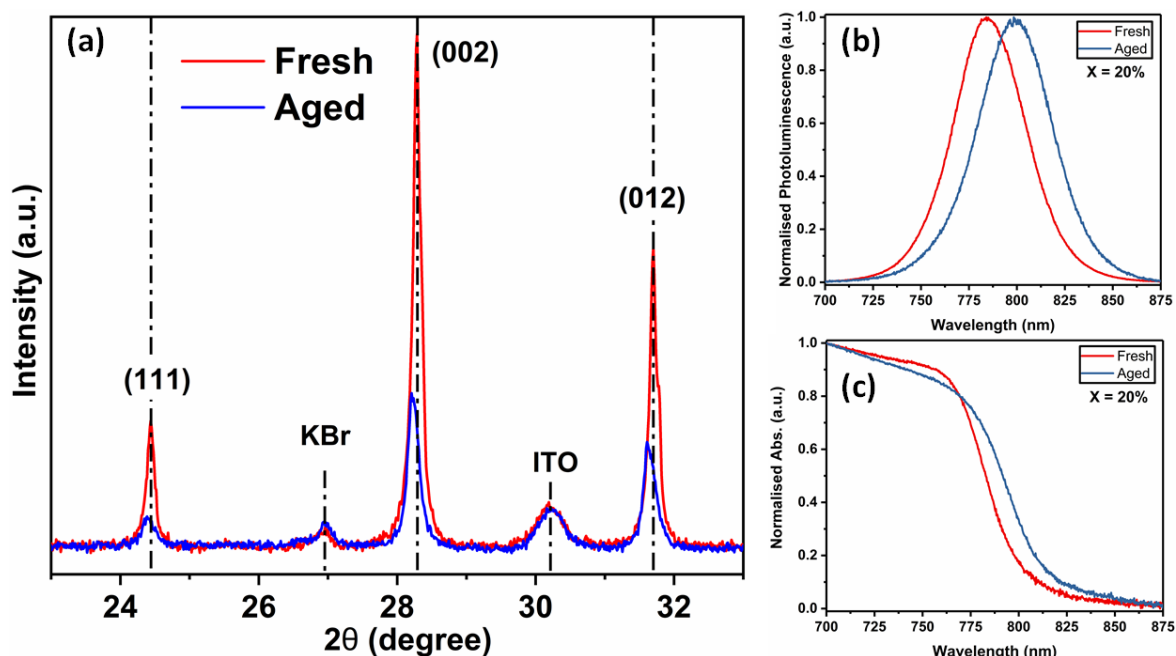


**Figure 27:** (a) XRD patterns, (b) Normalised UV-Vis absorption and (c) Normalised photoluminescence recorded on freshly prepared and aged TC perovskite films with X=20%.

Our results suggest therefore that while the addition of KI to the perovskite solution has the primary beneficial effect of passivating the ETL/perovskite interface at low concentrations, the addition of KI does not enhance the stability of devices incorporating an np-SnO<sub>2</sub> electron-extracting contact, due to the fact that the KI is apparently responsible for inadvertent compositional and phase changes to the TC perovskite. We emphasize that our control device (0% KI) that utilised a SnO<sub>2</sub> ETL was itself moderately passivated at the ETL interface by potassium ions resulting from the KOH stabiliser added to the SnO<sub>2</sub> deposition solution. This suggests therefore that the presence of small quantities of potassium at the ETL-perovskite interface does not apparently have a negative effect on the stability of a TC PSC device. However, when KI is added in high concentration to a TC precursor solution, it leads to presence of secondary phases in the film. This may cause further changes in the perovskite composition due to the application of a built-in voltage under

operational conditions leading to accelerated degradation of TC perovskite solar cells.

## Conclusions

We have systematically explored the effect of adding potassium iodide KI (0 – 20%) into a triple-cation (TC) perovskite precursor solution to determine whether it can be used to improve the efficiency of solar cell devices by passivating defect states in the perovskite and at the perovskite electron transport layer (ETL) interface. The device ETL was fabricated using a nanoparticle SnO<sub>2</sub> solution (made using a commercial colloidal product), with a range of KI different concentrations added to the perovskite precursor solution. For comparison, devices containing different concentrations of KI were also fabricated using a TiO<sub>2</sub> ETL reference. As has been previously observed,<sup>[2,53–56]</sup> the addition of KI to the TC perovskite induced a redshift in both PL emission and absorption band-edge, consistent with an increase in lattice parameter. This was accompanied by a reduction in average grain size and increase in film RMS roughness. It was found that devices fabricated on SnO<sub>2</sub> ETLs incorporating additional KI were characterised by reduced power conversion efficiency compared to un-passivated controls. In contrast, it was found that devices based on a TC perovskite incorporating 10% KI and fabricated on a TiO<sub>2</sub> ETL had a relatively improved power conversion efficiency compared to a 0% KI control. We assign the lack of improvement in the performance of SnO<sub>2</sub> based solar cells with a KI additive to the fact that the SnO<sub>2</sub>/perovskite interface was already partially passivated by the KOH stabiliser that was present in the colloidal dispersion. Indeed, we suspect that this stabiliser acts as an intrinsic source of K<sup>+</sup> ions that minimises defects at the ETL/perovskite interface. For this reason, the addition of excess KI to

the TC precursor solution resulted in a reduction in device performance due to the segregation of KBr and the formation of other non-perovskite phases.

We investigated the effect of this KI additive on both intrinsic film stability and on device performance over 500 hours of illumination and bias and found it has a detrimental effect on operational stability in devices incorporating both SnO<sub>2</sub> and TiO<sub>2</sub> ETLs. At a KI concentration of 5 and 10% KI in the initial precursor, the perovskite is found to be less phase stable, with the formation of KBr and consequent removal of Br from the perovskite phase during film formation leading to a greater phase instability to the  $\delta$ -phase under operational conditions. At very high KI concentrations (20% or higher) the perovskite devices undergo rapid, critical failure due to additional extraction of bromide species and the formation of a non-perovskite phase (KBr) under illumination and applied bias.

## 5.2: Supporting Information

### Original Electronic Support Information (ESI)

#### Methods

##### Device fabrication

**Materials and cleaning process:** The following materials were purchased from Ossila Ltd: Indium tin oxide (ITO) glass substrates (20  $\Omega$ /square), FTO (6  $\Omega$ /square), formamidinium iodide (FAI, 98%), spiro-OMeTAD (sublimed 99.5%) and methylammonium bromide (MABr, 99.5%). Additional materials were purchased as follows: SnO<sub>2</sub> 15 wt% in H<sub>2</sub>O colloidal dispersion liquid (Alfa Aesar 44592.36), lead (II) bromide PbBr<sub>2</sub>, lead (II) iodide (PbI<sub>2</sub>, 99.99%) (Tokyo Chemical Industry UK Ltd) and gold wire (Cookson Gold Ltd). All other solvents and materials were purchased from Sigma Aldrich Ltd.

ITO and FTO were etched using a 4M of hydrochloric acid solution together with zinc powder that was scattered onto the substrate surface. Following etching, substrates were immersed in a solution of 2% Hellmanex mixed with boiling deionised water and then sonicated for 15 minutes, before rinsing with DI water. This was followed by sonication in isopropanol for a further 15 minutes. Finally, substrates were dried using a nitrogen jet and cleaned for 15 minutes using an ultraviolet-ozone (UV) treatment.

**Electron transport layer:** Both SnO<sub>2</sub> and TiO<sub>2</sub> were used as electron transport layers (ETLs). SnO<sub>2</sub> was deposited onto ITO by spin-coating at 3000 rpm from a commercial (SnO<sub>2</sub> colloidal solution 15 wt% in water) which was diluted with DI water (6.5:1). Following deposition, the film was annealed for 30 minutes at 150 °C.

Compact TiO<sub>2</sub> (c-TiO<sub>2</sub>) was deposited on top of FTO substrates by spray pyrolysis.

Here, the FTO was heated to 450 °C with titanium diisopropoxide bis(acetylacetonate) (75 wt% in isopropanol) dissolved in n-butanol (1:9) sprayed onto its surface, followed by a further 30 minutes of annealing before cooling to room temperature. Following this, mesoporous TiO<sub>2</sub> (mp-TiO<sub>2</sub>) was deposited on-top of the c-TiO<sub>2</sub> by spin coating TiO<sub>2</sub> paste dissolved in n-butanol (1:6) at 5000 rpm for 30 seconds, following which it was annealed at 450 °C for 45 minutes.

**Perovskite:** Perovskite triple-cation (TC) precursor solution was prepared by dissolving FAI (1M), MABr (0.2M), PbBr<sub>2</sub> (0.2M) and PbI<sub>2</sub> (1.1M) in anhydrous DMF/DMSO (4:1 volume ratio), into which an additional 42 µl (per ml of solvents) of 1.5M CsI solution in DMSO was added. Following this, 1.5M potassium iodide (KI) solution in DMF/DMSO (4:1 volume ratio) was added at various percentages (0-20%). The TC precursor solution was then deposited on top of the ETL. Here, films were spin coated using a two-step process at 1000 rpm for a duration of 10 seconds, followed by 6000 rpm for 20 seconds, with 100 µl of chlorobenzene antisolvent dropped onto the films after a duration of 25 seconds. Finally, the films were annealed at 100 °C for 60 minutes.

**Hole transport layer and top contact:** The hole transport layer (HTL) was prepared from a solution containing 86 mg ml<sup>-1</sup> spiro-OMeTAD in chlorobenzene, doped with 34 µl of 4-tert-butylpyridine (tBP), 20 µl of bis(trifluoromethane)sulfonimide lithium (LiTFSI) in acetonitrile solution (500 mg/mL) and 11 µL of FK209 Co(II) PF<sub>6</sub> (FK209) in acetonitrile solution (300 mg/mL). After mixing and filtering, the HTL solution was spin-coated dynamically at 4000 rpm for 30 seconds before leaving in dry air overnight. The device cathode (Au) was thermally evaporated under high vacuum creating a 80 nm thick layer.

Where used, SiO<sub>2</sub> encapsulation was deposited by electron-beam evaporation under

high vacuum at a deposition rate of  $0.1\text{-}1 \text{ \AA s}^{-1}$  to a final thickness of 100 nm. The structure of a typical device is shown schematically in Figure 1.

## **Characterisation**

**Current-voltage measurement:** To characterise device performance, JV characteristics were recorded when illuminated using a Newport 92251A-1000 AM1.5g solar simulator. The system was initially calibrated using an NREL certified silicon reference cell, with the simulator optical power output adjusted to  $100 \text{ mWcm}^{-2}$  at  $25 \text{ }^\circ\text{C}$ . During measurement, an aperture mask ( $0.026 \text{ cm}^2$ ) was placed over each individual solar cell to accurately define the areas over which the perovskite solar cell was illuminated and to reduce contributions resulting from stray (scattered) light. JV curves were recorded using a Keithley 237 source measure unit that swept the voltage (in both directions) from  $-0.1$  to  $1.2 \text{ V}$  at  $0.1 \text{ Vs}^{-1}$ .

**Scanning electron microscopy (SEM):** SEM images of perovskite surfaces and device cross-sections were recorded using a Carl Zeiss-modified Raith Nanofabrication SEM with an in-lens detector. Here the microscope was operated with a typical working distance of  $\sim 2.5 \text{ mm}$  and at a low accelerating voltage of  $1.5 \text{ kV}$  to minimise sample damage. Grain sizes were calculated using ImageJ software.

**Atomic force microscopy (AFM):** Images were recorded using a Veeco Dimension 3100 instrument with a Nanoscope 3A feedback controller used in tapping mode. The AFM was equipped with TESPA-V2 probes having a resonance frequency of around  $320 \text{ KHz}$  and spring constant of  $42 \text{ Nm}^{-1}$ .

**X-ray diffractometer:** A PANalytical X'Pert Pro system powered by a Philips PW3050/60 ( $\theta/\theta$ ) X-ray generator diffractometer ( $240 \text{ mm}$  diameter) with a PW3064 sample spinner was used to determine X-ray diffraction data. The X-ray

source was a Copper Line Focus X-ray tube with  $K\alpha$  radiation ( $K\alpha_1 = 1.5406 \text{ \AA}$ ,  $K\alpha_2 = 1.5444 \text{ \AA}$ ,  $K\alpha$  ratio 0.5,  $K\alpha_{\text{avg}} = 1.5419 \text{ \AA}$ ) and a Ni  $K\beta$  absorber (0.02 mm,  $K\beta = 1.3923 \text{ \AA}$ ). This was run at 45 kV with a tube current of 40 mA. For data collection, a 1D-detector was used in Bragg-Brentano geometry, with data collected from  $5.00^\circ$  to  $80.00^\circ$   $2\theta$  with a step size of  $0.0131^\circ$ . All scans were carried out continuously in intervals of 0.31 seconds.

**Photoluminescence:** A 405 nm CW laser diode was used to excite the samples. Photoluminescence was collected at a normal incidence using an optical fibre and was directed into an Andor Shamrock CCD spectrometer.

**Time-resolved photoluminescence (TRPL):** Time-correlated single-photon counting (TCSPC) was used to measure the transient luminescence emitted from the perovskite films. Here, the samples were excited with a 507 nm pulsed laser (PicoQuant GmbH) at 2.5 MHz with a pulse width of  $\sim 600$  ps and an excitation fluence of  $\sim 1 \mu\text{J cm}^{-2}$ . Luminescence was detected using a Micro Photon Devices silicon SPAD (single photon avalanche diode). The system was controlled using a TimeHarp 260 Pico PCIe board (PicoQuant GmbH) with data points having a time resolution of 25 ps.

**Grazing incidence wide-angle X-ray scattering (GIWAXS):** Xeuss 2.0 (Xenocs) system with 9.243 keV X-rays from a liquid Ga MetalJet source (Excillum) was used to perform ex-situ grazing incidence X-ray scattering. X-rays were incident on the perovskite films at a grazing angle of  $2^\circ$ . The sample and flight tube were held under vacuum during operation to remove background scatter. A Pilatus3R 1M detector held at a distance of  $\sim 300$  mm from the sample was used to detect scattered X-rays.

The GIXSGUI MATLAB toolbox was used for data analysis, reduction and reshaping.<sup>[57]</sup>

*In-situ* GIWAXS experiments were performed at the I22 beamline at Diamond Light Source. Here, X-rays with photon energy 14 keV were incident on thin film samples having the structure glass/ITO/SnO<sub>2</sub>/perovskite which were held inside a sample chamber. This controlled environmental chamber contained a resistive heater in the base which was set to 43, 120 or 150 °C for each experiment. This was combined with illumination from a white light LED set to ~2 suns intensity (200 ± 10 mW/cm<sup>2</sup>), with humidity controlled by using a moisture bubbler on a hotplate, fed from a dry N<sub>2</sub> feed, as used in our previous work.<sup>[58]</sup> Scattering was collected with a PILATUS P3-2M-L (DECTRIS) hybrid photon counting detector mounted approximately 260 mm from the sample, with all integrated intensities averaged from two locations on each sample. Beam damage was carefully controlled (attenuation and maximum exposure) under accelerated aging conditions prior to each experiment. This allowed us to ensure that material changes observed were caused by the designed degradation factors rather than from X-ray beam damage. Data was reduced and analysed using *PyFAI*.<sup>[59]</sup>

**Lifetime testing:** An Atlas Suntest CPS+ with a 1500 W xenon bulb equipped with quartz IR reducing filters calibrated to 100 mWcm<sup>-2</sup> was used to continuously irradiate samples in ambient air (typically ~35 - 45% RH). Devices were irradiated without an aperture mask in place. *J-V* measurements were continually recorded under reverse sweep from 1.2 to 0 V at a scan rate of 0.012 V s<sup>-1</sup>. Devices were held at open circuit between measurements, with scans on each cell recorded at intervals of approximately 4 minutes. Aged perovskite devices used for GIWAXS, XRD and UV-

Vis absorption measurements (data shown in Figures 17, 22(a, b and c), 23, 25, 26 and 27) were aged using the same lamp system and under the same conditions, however devices were not protected using a SiO<sub>2</sub> encapsulation layer.

## Supplementary Tables

ETL	Perovskite composition	Potassium content (mol%)	Improved parameters (H = reduced hysteresis)						Aging protocol	Device stability condition	Stability improvement (Yes/No)	Ref
			V <sub>oc</sub>	J <sub>sc</sub>	FF	PCE	H					
c-TiO <sub>2</sub>   mp-TiO <sub>2</sub>	FA <sub>0.85</sub> MA <sub>0.15</sub> Cs <sub>0.05</sub> PbI <sub>2.7</sub> Br <sub>0.3</sub>	~ 1%	✓	✓	✓	✓	✓	N/A			1	
c-TiO <sub>2</sub>   mp-TiO <sub>2</sub>	(Cs,FA,MA)PbI <sub>2</sub> ( <sub>0.85</sub> Br <sub>0.15</sub> ) <sub>3</sub>	10%	✓	✓	✓	✓	✓	Shelf-life (ISOS D-1)	40 °C, N <sub>2</sub> atmosphere	Yes	2	
c-TiO <sub>2</sub>   mp-TiO <sub>2</sub>	(Cs,FA,MA)PbI <sub>2</sub> ( <sub>0.85</sub> Br <sub>0.15</sub> ) <sub>3</sub>	10%	✓	✓	✓	✓	✓	Operational MPP (ISOS L-1)	40 °C, 1 sun, N <sub>2</sub> atmosphere	N/A	2	
c-TiO <sub>2</sub>   mp-TiO <sub>2</sub>	(Cs <sub>0.05</sub> MA <sub>0.15</sub> FA <sub>0.79</sub> )PbI <sub>2</sub> ( <sub>0.85</sub> Br <sub>0.15</sub> ) <sub>3</sub>	10%	✓	✓	✓	✓	✓	N/A			3	
SnO <sub>2</sub> (CBD)	Cs <sub>0.05</sub> (FA <sub>0.85</sub> MA <sub>0.15</sub> ) <sub>0.95</sub> PbI <sub>2</sub> ( <sub>0.85</sub> Br <sub>0.15</sub> ) <sub>3</sub>	3.5%	✓	✓	✓	✓	✓	N/A			4	
TiO <sub>2</sub>	Cs <sub>0.925</sub> K <sub>0.075</sub> PbI <sub>2</sub> Br	0.075%	✓	✓	✓	✓	✓	Shelf-life (ISOS D-1)	RH=20%, 20 °C	Yes	5	
c-TiO <sub>2</sub> :LiMg   mp-TiO <sub>2</sub> :Li	FA <sub>0.85</sub> MA <sub>0.15</sub> PbI <sub>2</sub> ( <sub>0.85</sub> Br <sub>0.15</sub> ) <sub>3</sub>	5%	✓	✓	✓	✓	✓	Shelf-life (ISOS D-1)	Dark drying room, dew point temp. -30 °C	N/A	6	
PCBM (pin)	MAPbI <sub>3</sub> (PEDOT:PSS HTL)	0.5%	✓	✓	✓	✓	✓				7	
TiO <sub>2</sub>	MAPbI <sub>3</sub>	N/A	✓	✓	✓	✓	✓				8	
TiO <sub>2</sub>	FA <sub>0.87</sub> MA <sub>0.13</sub> PbI <sub>2</sub> ( <sub>0.87</sub> Br <sub>0.13</sub> ) <sub>3</sub>	5%	✓	✓	✓	✓	✓	Shelf-life (ISOS D-1+light)	RH=30%, room temp., 1 sun	Yes	9	
np-SnO <sub>2</sub> (Alfa Aesar)	Cs <sub>0.05</sub> FA <sub>0.79</sub> MA <sub>0.16</sub> PbI <sub>2</sub> ( <sub>0.75</sub> Br <sub>0.25</sub> ) <sub>3</sub>	15%	✓	✓	✓	✓	✓	Shelf-life (ISOS D-1)	RH=20%, ambient air	Yes	10	
0.1 M solution of SnCl <sub>2</sub> (98%) in absolute ethanol (SnO <sub>2</sub> )	MA <sub>0.17</sub> FA <sub>0.83</sub> PbI <sub>2.5</sub> Br <sub>0.5</sub>	3%	✓	✓	✓	✓	✓	Shelf-life (ISOS D-1)	RH=30-45%, ambient air	Yes	11	
SnO <sub>2</sub> (CBD)	Cs <sub>0.05</sub> (FA <sub>0.85</sub> MA <sub>0.15</sub> ) <sub>0.95</sub> PbI <sub>2</sub> ( <sub>0.85</sub> Br <sub>0.15</sub> ) <sub>3</sub>	3.5%	✓	✓	✓	✓	✓	Shelf-life (ISOS D-1)	RH=10±5%, ambient air	Yes	12	
c-TiO <sub>2</sub>   mp-TiO <sub>2</sub>	MAPbI <sub>3</sub>	0.5%	✓	✓	✓	✓	✓	Shelf-life (ISOS D-1)	RH=46%, ambient air	Yes	13	
SnO <sub>2</sub>   c-TiO <sub>2</sub>   mp-TiO <sub>2</sub>	(FA <sub>0.85</sub> MA <sub>0.17</sub> )PbI <sub>2</sub> ( <sub>0.85</sub> Br <sub>0.17</sub> ) <sub>3</sub>	3%	✓	✓	✓	✓	✓	Shelf-life (ISOS D-1)	RH=40%, 25 °C	Yes	14	
np-SnO <sub>2</sub> (Alfa Aesar)	Cs <sub>0.05</sub> FA <sub>0.79</sub> MA <sub>0.15</sub> PbI <sub>2.45</sub> Br <sub>0.55</sub>	10%					✓	Operational (ISOS L-1 and held at V <sub>oc</sub> )	RH=40% @ 42 °C, 1 sun	No	This work	
c-TiO <sub>2</sub>   mp-TiO <sub>2</sub>	Cs <sub>0.05</sub> FA <sub>0.79</sub> MA <sub>0.15</sub> PbI <sub>2.45</sub> Br <sub>0.55</sub>	10%	✓	✓	✓	✓	✓	Operational (ISOS L-1 and held at V <sub>oc</sub> )	RH=40% @ 42 °C, 1 sun	No	This work	

**Table S1:** Comparison of this work with existing literature on addition of KI in hybrid lead halide perovskite.

## References for Table 1

- 1 D.-Y. Son, S.-G. Kim, J.-Y. Seo, S.-H. Lee, H. Shin, D. Lee and N. Park, *J. Am. Chem. Soc.*, **2018**, 140, 1358–1364.
- 2 M. Abdi-Jalebi, Z. Andaji-Garmaroudi, S. Cacovich, C. Stavrakas, B. Philippe, J. M. Richter, M. Alsari, E. P. Booker, E. M. Hutter, A. J. Pearson, S. Lilliu, T. J. Savenije, H. Rensmo, G. Divitini, C. Ducati, R. H. Friend and S. D. Stranks, *Nature*, **2018**, 555, 497–501.
- 3 M. Abdi-Jalebi, Z. Andaji-Garmaroudi, A. J. Pearson, G. Divitini, S. Cacovich, B. Philippe, H. Rensmo, C. Ducati, R. H. Friend and S. D. Stranks, *ACS Energy Lett.*, **2018**, 3, 2671–2678.
- 4 F. Zheng, W. Chen, T. Bu, K. P. Ghiggino, F. Huang, Y. Cheng, P. Tapping, T. W. Kee, B. Jia and X. Wen, *Adv. Energy Mater.*, **2019**, 9, 1901016.
- 5 J. K. Nam, S. U. Chai, W. Cha, Y. J. Choi, W. Kim, M. S. Jung, J. Kwon, D. Kim and J. H. Park, *Nano Lett.*, **2017**, 17, 2028–2033.
- 6 Z. Tang, T. Bessho, F. Awai, T. Kinoshita, M. M. Maitani, R. Jono, T. N. Murakami, H. Wang, T. Kubo, S. Uchida and H. Segawa, *Sci. Rep.*, **2017**, 7, 12183.
- 7 J. Chang, Z. Lin, H. Zhu, F. H. Isikgor, Q.-H. Xu, C. Zhang, Y. Hao and J. Ouyang, *J. Mater. Chem. A*, **2016**, 4, 16546–16552.
- 8 W. Zhao, Z. Yao, F. Yu, D. Yang and S. F. Liu, *Adv. Sci.*, **2018**, 5, 1700131.
- 9 L. Kuai, Y. Wang, Z. Zhang, Y. Yang, Y. Qin, T. Wu, Y. Li, Y. Li, T. Song, X. Gao, L. Wang and B. Sun, *Sol. RRL*, **2019**, 3, 1900053.
- 10 L. Wang, G. Wang, Z. Yan, J. Qiu, C. Jia, W. Zhang, C. Zhen, C. Xu, K. Tai, X. Jiang and S. Yang, *Sol. RRL*, **2020**, 4, 2000098.
- 11 D. Yao, C. Zhang, N. D. Pham, Y. Zhang, V. T. Tiong, A. Du, Q. Shen, G. J. Wilson and H. Wang, *J. Phys. Chem. Lett.*, **2018**, 9, 2113–2120.
- 12 T. Bu, X. Liu, Y. Zhou, J. Yi, X. Huang, L. Luo, J. Xiao, Z. Ku, Y. Peng, F. Huang, Y.-B. Cheng and J. Zhong, *Energy Environ. Sci.*, **2017**, 10, 2509–2515.
- 13 S. Jia, J. Wang and L. Zhu, *J. Mater. Sci. Mater. Electron.*, **2019**, 30, 2057–2066.
- 14 Y. Yang, L. Wu, X. Hao, Z. Tang, H. Lai, J. Zhang, W. Wang and L. Feng, *RSC Adv.*, **2019**, 9, 28561–28568.

Concentration of KI	V <sub>oc</sub> (V)	J <sub>sc</sub> (mA cm <sup>-2</sup> )	FF (%)	PCE (%)
X = 0%	1.10 (1.08 ± 0.01)	22.83 (22.33 ± 0.41)	77.62 (75.68 ± 1.32)	18.38 (17.51 ± 0.48)
X = 5%	1.08 (1.07 ± 0.01)	22.55 (21.27 ± 0.18)	74.78 (73.55 ± 0.95)	17.36 (16.39 ± 0.61)
X = 10%	1.07 (1.05 ± 0.01)	21.47 (21.21 ± 0.16)	74.53 (72.49 ± 1.38)	16.85 (15.90 ± 0.74)
X = 20%	1.06 (1.03 ± 0.03)	20.48 (20.18 ± 0.24)	72.53 (71.18 ± 1.02)	15.53 (14.72 ± 0.72)

**Table S2:** Summary of reverse scan (V<sub>oc</sub> to J<sub>sc</sub>) performance metrics of all devices and average values from a minimum of 17 cells per testing condition.

KI addition	Hysteresis Index
X = 0%	0.0598
X = 5%	0.0138
X = 10%	0.0065
X = 20%	0.0039

**Table S3:** J-V hysteresis index (HI) for champion devices whose metric are presented in Table S1 (main manuscript). HI is calculated using  $HI = \frac{PCE (reverse) - PCE (forward)}{PCE (reverse)}$

[34]

<b>Composition</b>	<b>RMS roughness (<math>S_q</math>) (nm)</b>	<b>Mean roughness (<math>S_a</math>) (nm)</b>
<b>X = 0%</b>	<b>22.13</b>	<b>17.78</b>
<b>X = 5%</b>	<b>24.61</b>	<b>19.81</b>
<b>X = 10%</b>	<b>35.47</b>	<b>28.65</b>
<b>X = 20%</b>	<b>46.09</b>	<b>36.31</b>

**Table S4:** Root-mean-square roughness RMS ( $S_q$ ) and mean roughness ( $S_a$ ) as determined from AFM images.

### 5.3: References

- [1] T. Duong, Y. Wu, H. Shen, J. Peng, X. Fu, D. Jacobs, E.-C. Wang, T. C. Kho, K. C. Fong, M. Stocks, E. Franklin, A. Blakers, N. Zin, K. McIntosh, W. Li, Y.-B. Cheng, T. P. White, K. Weber, K. Catchpole, *Adv. Energy Mater.* **2017**, *7*, 1700228.
- [2] M. Abdi-Jalebi, Z. Andaji-Garmaroudi, S. Cacovich, C. Stavrakas, B. Philippe, J. M. Richter, M. Alsari, E. P. Booker, E. M. Hutter, A. J. Pearson, S. Lilliu, T. J. Savenije, H. Rensmo, G. Divitini, C. Ducati, R. H. Friend, S. D. Stranks, *Nature* **2018**, *555*, 497.
- [3] M. Grätzel, *Nat. Mater.* **2014**, *13*, 838.
- [4] Q. Zhang, M. M. Tavakoli, L. Gu, D. Zhang, L. Tang, Y. Gao, J. Guo, Y. Lin, S. Leung, S. Poddar, Y. Fu, Z. Fan, *Nat. Commun.* **2019**, *10*, 1.
- [5] Z.-K. Tan, R. S. Moghaddam, M. L. Lai, P. Docampo, R. Higler, F. Deschler, M. Price, A. Sadhanala, L. M. Pazos, D. Credgington, F. Hanusch, T. Bein, H. J. Snaith, R. H. Friend, *Nat. Nanotechnol.* **2014**, *9*, 687.
- [6] H. Wei, J. Huang, *Nat. Commun.* **2019**, *10*, 1.
- [7] S. Yakunin, D. N. Dirin, Y. Shynkarenko, V. Morad, I. Cherniukh, O. Nazarenko, D. Kreil, T. Nauser, M. V. Kovalenko, *Nat. Photonics* **2016**, *10*, 585.
- [8] S. De Wolf, J. Holovsky, S.-J. Moon, P. Löper, B. Niesen, M. Ledinsky, F.-J. Haug, J.-H. Yum, C. Ballif, *J. Phys. Chem. Lett.* **2014**, *5*, 1035.
- [9] A. Miyata, A. Mitioglu, P. Plochocka, O. Portugall, J. T. W. Wang, S. D. Stranks, H. J. Snaith, R. J. Nicholas, *Nat. Phys.* **2015**, *11*, 582.
- [10] Y. Chen, H. T. Yi, X. Wu, R. Haroldson, Y. N. Gartstein, Y. I. Rodionov, K. S. Tikhonov, A. Zakhidov, X. Y. Zhu, V. Podzorov, *Nat. Commun.* **2016**, *7*, 1.
- [11] S. D. Stranks, H. J. Snaith, *Nat. Nanotechnol.* **2015**, *10*, 391.
- [12] W. Zhang, G. E. Eperon, H. J. Snaith, *Nat. Energy* **2016**, *1*, 16048.
- [13] T. Leijtens, G. E. Eperon, N. K. Noel, S. N. Habisreutinger, A. Petrozza, H. J.

- Snaith, *Adv. Energy Mater.* **2015**, *5*, 1.
- [14] M. Saliba, T. Matsui, J.-Y. Seo, K. Domanski, J.-P. Correa-Baena, M. K. Nazeeruddin, S. M. Zakeeruddin, W. Tress, A. Abate, A. Hagfeldt, M. Grätzel, *Energy Environ. Sci.* **2016**, *9*, 1989.
- [15] E. T. Hoke, D. J. Slotcavage, E. R. Dohner, A. R. Bowring, H. I. Karunadasa, M. D. McGehee, *Chem. Sci.* **2015**, *6*, 613.
- [16] S. D. Stranks, *ACS Energy Lett.* **2017**, *2*, 1515.
- [17] D. Bi, C. Yi, J. Luo, J.-D. Décoppet, F. Zhang, S. M. Zakeeruddin, X. Li, A. Hagfeldt, M. Grätzel, *Nat. Energy* **2016**, *1*, 16142.
- [18] F. Wang, A. Shimazaki, F. Yang, K. Kanahashi, K. Matsuki, Y. Miyauchi, T. Takenobu, A. Wakamiya, Y. Murata, K. Matsuda, *J. Phys. Chem. C* **2017**, *121*, 1562.
- [19] J. Peng, J. I. Khan, W. Liu, E. Ugur, T. Duong, Y. Wu, H. Shen, K. Wang, H. Dang, E. Aydin, X. Yang, Y. Wan, K. J. Weber, K. R. Catchpole, F. Laquai, S. De Wolf, T. P. White, *Adv. Energy Mater.* **2018**, *8*, 1801208.
- [20] J. Dagar, K. Hirselandt, A. Merdasa, A. Czudek, R. Munir, F. Zu, N. Koch, T. Dittrich, E. L. Unger, *Sol. RRL* **2019**, *3*, 1900088.
- [21] P. Zhu, S. Gu, X. Luo, Y. Gao, S. Li, J. Zhu, H. Tan, *Adv. Energy Mater.* **2020**, *10*, 1903083.
- [22] W.-Q. Wu, J.-X. Zhong, J.-F. Liao, C. Zhang, Y. Zhou, W. Feng, L. Ding, L. Wang, D.-B. Kuang, *Nano Energy* **2020**, *75*, 104929.
- [23] W. Feng, C. Zhang, J.-X. Zhong, L. Ding, W.-Q. Wu, *Chem. Commun.* **2020**, *56*, 5006.
- [24] B. Philippe, M. Saliba, J.-P. Correa-Baena, U. B. Cappel, S.-H. Turren-Cruz, M. Grätzel, A. Hagfeldt, H. Rensmo, *Chem. Mater.* **2017**, *29*, 3589.
- [25] T. Bu, X. Liu, Y. Zhou, J. Yi, X. Huang, L. Luo, J. Xiao, Z. Ku, Y. Peng, F. Huang, Y.-B. Cheng, J. Zhong, *Energy Environ. Sci.* **2017**, *10*, 2509.

- [26] D. J. Kubicki, D. Prochowicz, A. Hofstetter, S. M. Zakeeruddin, M. Grätzel, L. Emsley, *J. Am. Chem. Soc.* **2017**, *139*, 14173.
- [27] P. Zhao, W. Yin, M. Kim, M. Han, Y. J. Song, T. K. Ahn, H. S. Jung, *J. Mater. Chem. A* **2017**, *5*, 7905.
- [28] L. Wang, G. Wang, Z. Yan, J. Qiu, C. Jia, W. Zhang, C. Zhen, C. Xu, K. Tai, X. Jiang, S. Yang, *Sol. RRL* **2020**, *4*, 2000098.
- [29] M. Abdi-Jalebi, Z. Andaji-Garmaroudi, A. J. Pearson, G. Divitini, S. Cacovich, B. Philippe, H. Rensmo, C. Ducati, R. H. Friend, S. D. Stranks, *ACS Energy Lett.* **2018**, *3*, 2671.
- [30] S.-H. Turren-Cruz, M. Saliba, M. T. Mayer, H. Juárez-Santiesteban, X. Mathew, L. Nienhaus, W. Tress, M. P. Erodici, M.-J. Sher, M. G. Bawendi, M. Grätzel, A. Abate, A. Hagfeldt, J.-P. Correa-Baena, *Energy Environ. Sci.* **2018**, *11*, 78.
- [31] D. Moia, I. Gelmetti, P. Calado, W. Fisher, M. Stringer, O. Game, Y. Hu, P. Docampo, D. Lidzey, E. Palomares, J. Nelson, P. R. F. Barnes, *Energy Environ. Sci.* **2019**, *12*, 1296.
- [32] D.-Y. Son, S.-G. Kim, J.-Y. Seo, S.-H. Lee, H. Shin, D. Lee, N. Park, *J. Am. Chem. Soc.* **2018**, *140*, 1358.
- [33] Z. Tang, T. Bessho, F. Awai, T. Kinoshita, M. M. Maitani, R. Jono, T. N. Murakami, H. Wang, T. Kubo, S. Uchida, H. Segawa, *Sci. Rep.* **2017**, *7*, 12183.
- [34] S. N. Habisreutinger, N. K. Noel, H. J. Snaith, *ACS Energy Lett.* **2018**, *3*, 2472.
- [35] D. Meggiolaro, S. G. Motti, E. Mosconi, A. J. Barker, J. Ball, C. Andrea Riccardo Perini, F. Deschler, A. Petrozza, F. De Angelis, *Energy Environ. Sci.* **2018**, *11*, 702.
- [36] N. Phung, A. Abate, *Small* **2018**, *14*, 1802573.
- [37] J.-X. Zhong, J.-F. Liao, Y. Jiang, L. Wang, D.-B. Kuang, W.-Q. Wu, *J. Mater. Chem. A* **2020**, *8*, 9743.
- [38] L. Kuai, Y. Wang, Z. Zhang, Y. Yang, Y. Qin, T. Wu, Y. Li, Y. Li, T. Song, X. Gao, L.

- Wang, B. Sun, *Sol. RRL* **2019**, *3*, 1900053.
- [39] Y. Yang, L. Wu, X. Hao, Z. Tang, H. Lai, J. Zhang, W. Wang, L. Feng, *RSC Adv.* **2019**, *9*, 28561.
- [40] T. Bu, J. Li, F. Zheng, W. Chen, X. Wen, Z. Ku, Y. Peng, J. Zhong, Y.-B. Cheng, F. Huang, *Nat. Commun.* **2018**, *9*, 4609.
- [41] J. A. Smith, O. S. Game, J. E. Bishop, E. L. K. Spooner, R. C. Kilbride, C. Greenland, R. Jayaprakash, T. I. Alanazi, E. J. Cassella, A. Tejada, G. Chistiakova, M. Wong-Stringer, T. J. Routledge, A. J. Parnell, D. B. Hammond, D. G. Lidzey, *ACS Appl. Energy Mater.* **2020**, acsaem.0c00525.
- [42] Y. Hu, M. F. Aygüler, M. L. Petrus, T. Bein, P. Docampo, *ACS Energy Lett.* **2017**, *2*, 2212.
- [43] T. Singh, S. Öz, A. Sasinska, R. Frohnhoven, S. Mathur, T. Miyasaka, *Adv. Funct. Mater.* **2018**, *28*, 1.
- [44] R. D. Shannon, *Acta Crystallogr.* **1976**, *32*, 751.
- [45] Y. Zhou, Y. Zhao, *Energy Environ. Sci.* **2019**, *12*, 1495.
- [46] H. X. Dang, K. Wang, M. Ghasemi, M.-C. Tang, M. De Bastiani, E. Aydin, E. Dauzon, D. Barrit, J. Peng, D.-M. Smilgies, S. De Wolf, A. Amassian, *Joule* **2019**, *3*, 1746.
- [47] L. T. Schelhas, Z. Li, J. A. Christians, A. Goyal, P. Kairys, S. P. Harvey, D. H. Kim, K. H. Stone, J. M. Luther, K. Zhu, V. Stevanovic, J. J. Berry, *Energy Environ. Sci.* **2019**, *12*, 1341.
- [48] L. Q. Xie, L. Chen, Z. A. Nan, H. X. Lin, T. Wang, D. P. Zhan, J. W. Yan, B. W. Mao, Z. Q. Tian, *J. Am. Chem. Soc.* **2017**, *139*, 3320.
- [49] Q. Jiang, L. Zhang, H. Wang, X. Yang, J. Meng, H. Liu, Z. Yin, J. Wu, X. Zhang, J. You, *Nat. Energy* **2017**, *2*, 16177.
- [50] Q. Wang, B. Chen, Y. Liu, Y. Deng, Y. Bai, Q. Dong, J. Huang, *Energy Environ. Sci.* **2017**, *10*, 516.

- [51] P. Gratia, I. Zimmermann, P. Schouwink, J.-H. Yum, J.-N. Audinot, K. Sivula, T. Wirtz, M. K. Nazeeruddin, *ACS Energy Lett.* **2017**, *2*, 2686.
- [52] M. Qin, K. Tse, T. Lau, Y. Li, C. Su, G. Yang, J. Chen, J. Zhu, U. Jeng, G. Li, H. Chen, X. Lu, *Adv. Mater.* **2019**, *31*, 1901284.
- [53] F. Zheng, W. Chen, T. Bu, K. P. Ghiggino, F. Huang, Y. Cheng, P. Tapping, T. W. Kee, B. Jia, X. Wen, *Adv. Energy Mater.* **2019**, *9*, 1901016.
- [54] J. Chang, Z. Lin, H. Zhu, F. H. Isikgor, Q.-H. Xu, C. Zhang, Y. Hao, J. Ouyang, *J. Mater. Chem. A* **2016**, *4*, 16546.
- [55] J. K. Nam, S. U. Chai, W. Cha, Y. J. Choi, W. Kim, M. S. Jung, J. Kwon, D. Kim, J. H. Park, *Nano Lett.* **2017**, *17*, 2028.
- [56] W. Zhao, Z. Yao, F. Yu, D. Yang, S. F. Liu, *Adv. Sci.* **2018**, *5*, 1700131.
- [57] Z. Jiang, *J. Appl. Crystallogr.* **2015**, *48*, 917.
- [58] O. S. Game, J. A. Smith, T. I. Alanazi, M. Wong-Stringer, V. Kumar, C. Rodenburg, N. J. Terrill, D. G. Lidzey, *J. Mater. Chem. A* **2020**, *8*, 10943.
- [59] G. Ashiotis, A. Deschildre, Z. Nawaz, J. P. Wright, D. Karkoulis, F. E. Picca, J. Kieffer, *J. Appl. Crystallogr.* **2015**, *48*, 510.

# Chapter 6

---

## Conclusions

At the time of writing, a range of new methods have been explored to fabricate perovskite solar cells (PSCs); these include spray-coating, dip-coating, blade-coating, slot die-coating, thermal evaporation, screen printing, and roll-to-roll printing. Such processes should hopefully eventually facilitate the production and manufacture of large area flexible devices. The work presented in this thesis has primarily focused on the fabrication of regular planar architecture photovoltaics (PVs). Devices were mainly fabricated by spin-coating, with studies performed to enhance device performance and long-term stability. Various charge transporting materials were explored, along with several active-layer perovskite compositions.

In **Chapter 4**, the effect of perovskite composition has been investigated on device performance and stability. Methylammonium lead iodide (MAPbI<sub>3</sub>) and triple-cation perovskite Cs<sub>0.05</sub>FA<sub>0.79</sub>MA<sub>0.15</sub>PbI<sub>2.45</sub>Br<sub>0.55</sub> perovskite compositions were fabricated based on the device structure of ITO/SnO<sub>2</sub>/perovskite/HTL/Au. This work demonstrates that triple-cation devices had better structural and optical properties and resulted in an enhanced device performance. Here, the best power conversion efficiency (PCE) for the triple-cation device investigated was found to be 19.5% as compared to 16% for MAPbI<sub>3</sub>. The stability of films and devices was then explored under enhanced stress conditions such as humidity, elevated temperature and illumination intensities of up to two suns. It was found that triple-cation PSCs have

improved performance, reduced hysteresis and considerably improved long-term stability compared to MAPbI<sub>3</sub>.

The relative stability of devices was then compared using two different hole transporting materials (HTMs); namely spiro-OMeTAD and PTAA. Here, it was found that triple-cation devices with spiro-HTM had better shelf-storage stability over 30 days, however, PTAA-HTM devices had better thermal stability compared to those using spiro-OMeTAD. These results indicate that further investigation of HTMs and interlayers is crucial to achieving further enhanced PSC performance and long-term operational stability.

In **Chapter 5**, the use of alkali metal halides as passivating agents for triple-cation hybrid perovskite has been studied, with devices incorporating SnO<sub>2</sub> and TiO<sub>2</sub> as electron transport layers (ETLs). Specifically, potassium iodide (KI) was used as a dopant into a triple-cation perovskite and it was found that KI can negatively affect device crystallinity as well as performance, with devices studied over a period of 500 hours. It was found that the perovskite-ETL interface was highly sensitive to this dopant, with such effects resulting from the fact that the SnO<sub>2</sub>/perovskite interface was already partially passivated by potassium hydroxide (KOH) present in the colloidal dispersion used. Here, the addition of excess KI in the triple-cation composition caused the segregation of KBr and the formation of other non-perovskite phases. The Chapter also confirmed the high-quality crystalline nature of pristine triple-cation perovskites that lead to excellent PSC performance and enhanced stability, further validating the conclusions reached in Chapter 4.

## 6.1: Proposed future work

For PSCs to eventually be commercialised, many open questions remain. I propose the following experiments that could be explored to further enhance device efficiency and stability:

- A range of alkali metals could be used to create new perovskite compositions, such as rubidium (Rb), sodium (Na), lithium (Li), magnesium (Mg), and guanidinium (Gu), with their effect on device performance and stability assessed.
- Such efficiency / stability studies could also comparatively examine devices based on different ETLs, such as:
  - Zinc oxide (ZnO)
  - [5,6]-Fullerene-C60 (C<sub>60</sub>)
  - [6,6]-Phenyl-C61-butyric acid methyl ester (PCBM)
- This could be complemented by experiments to explore a range of HTLs, such as:
  - Copper (II) phthalocyanine (CuPc)
  - Copper (I) oxide (Cu<sub>2</sub>O)
  - Cu<sub>2</sub>ZnSnS<sub>4</sub> (CZTS)
  - Nickel (II) oxide (NiO)

- Finally, it would be interesting to explore a series of materials to passivate the interface between the perovskite and charge transporting layer, with the aim being to further improve devices stability. There are several target materials of interest here including:
  - Poly[(thiophene)-alt-(6,7-difluoro-2-(2-hexyldecyloxy)quinoxaline)] (PTQ10)
  - Graphene oxide (GO)

In all cases, it will be interesting to determine device stability when exposed to various enhanced stress conditions, such as high light intensity, elevated temperature and high humidity, with the aim being to determine acceleration factors for device degradation. By determining acceleration factors it may be possible to further understand the mechanisms that underpin various degradation processes and to also make a better estimation for the practical lifetime of PSC devices when run under various 'real-world' operational conditions.